Terms and Conditions of Use of Digitised Theses from Trinity College Library Dublin

Copyright statement

All material supplied by Trinity College Library is protected by copyright (under the Copyright and Related Rights Act, 2000 as amended) and other relevant Intellectual Property Rights. By accessing and using a Digitised Thesis from Trinity College Library you acknowledge that all Intellectual Property Rights in any Works supplied are the sole and exclusive property of the copyright and/or other IPR holder. Specific copyright holders may not be explicitly identified. Use of materials from other sources within a thesis should not be construed as a claim over them.

A non-exclusive, non-transferable licence is hereby granted to those using or reproducing, in whole or in part, the material for valid purposes, providing the copyright owners are acknowledged using the normal conventions. Where specific permission to use material is required, this is identified and such permission must be sought from the copyright holder or agency cited.

Liability statement

By using a Digitised Thesis, I accept that Trinity College Dublin bears no legal responsibility for the accuracy, legality or comprehensiveness of materials contained within the thesis, and that Trinity College Dublin accepts no liability for indirect, consequential, or incidental, damages or losses arising from use of the thesis for whatever reason. Information located in a thesis may be subject to specific use constraints, details of which may not be explicitly described. It is the responsibility of potential and actual users to be aware of such constraints and to abide by them. By making use of material from a digitised thesis, you accept these copyright and disclaimer provisions. Where it is brought to the attention of Trinity College Library that there may be a breach of copyright or other restraint, it is the policy to withdraw or take down access to a thesis while the issue is being resolved.

Access Agreement

By using a Digitised Thesis from Trinity College Library you are bound by the following Terms & Conditions. Please read them carefully.

I have read and I understand the following statement: All material supplied via a Digitised Thesis from Trinity College Library is protected by copyright and other intellectual property rights, and duplication or sale of all or part of any of a thesis is not permitted, except that material may be duplicated by you for your research use or for educational purposes in electronic or print form providing the copyright owners are acknowledged using the normal conventions. You must obtain permission for any other use. Electronic or print copies may not be offered, whether for sale or otherwise to anyone. This copy has been supplied on the understanding that it is copyright material and that no quotation from the thesis may be published without proper acknowledgement.

Studies of Gain and Lasing in Thulium Doped Fibres

by
Severino Tessarin

A thesis submitted for the degree of Doctor of Philosophy
at the University of Dublin

School of Physics
Trinity College Dublin

Dublin, 2005

This thesis has not submitted as an exercise for a degree in this or any other university. The work described is entirely my own, with exception of assistance and collaborative work mentioned in the acknowledgements. I agree that Trinity College Library may lend or copy this thesis upon request.

Signature.

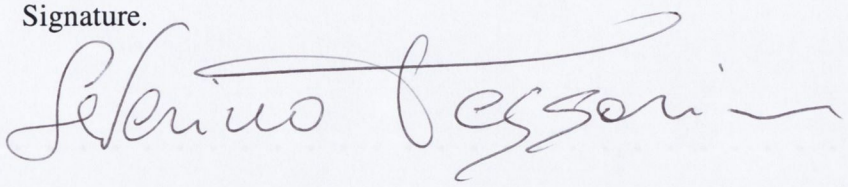

Abstract

Rare earth ions have absorption and emission lines in almost the entire transparent region of silica optical fibres, and they can be used as dopants inside the fibre core of single mode optical fibres employed for telecommunication. Erbium amplifiers has been far more successful than any other rare-earth doped amplifiers due to their unique properties such as high gain, low noise, polarization insensitivity and broad spectral bandwidth and they operate at 1550 nm- the wavelength where standard silica fibres have minimum losses.

In recent years, new types of glass host have been produced; they are mainly based on a mixture of heavy metal fluorides. The best known is named ZBLAN after the acronym of the fluoride salts component (Zr, Ba, La, N) with different stoichiometric weights. Normally the phonon energy is half of the silica fibre and the edge of the transparency region is thus shifted to longer wavelengths in the infrared region. Rare earth ion's metastable states also have longer lifetimes in fluoride hosts and, in addition, infrared fluorescence, which is normally quenched by phonon-assisted relaxation in silica, and which shows high quantum efficiency.

Praseodymium shows a transition centred at 1300 nm that is attractive for amplifying signals in the other low-losses region of standard silica fibres where they have zero dispersion point, moreover the several transitions across the visible spectrum make praseodymium fluoride fibres interesting for the construction of a visible laser. Praseodymium has a low absorption at wavelengths where pump diodes have already been produced for erbium doped amplifiers and this is an unwanted drawback either for a visible laser or for an IR amplifier, so a possible solution can be the use of a codopant capable of efficiently absorbing the pump radiation and then transferring it to the praseodymium ion. Thulium as a codopant will be shown to be effective in resonantly transferring the energy using a 790 nm pump to the highly excited levels of the praseodymium by an upcoversion process. A chapter of this thesis is dedicated to demonstrating the resonant transfer between the two ions and to characterising it's strength. The resonant transfer is shown in a praseodymium-thulium preform (first stage of fibre production) and subsequently in the fibre drawn from the preform. In the fibre other effects are present and they contribute to the population of the same level but with a different dynamic.

Recently, in new fibres produced by Lucent, the hydroxyl ions absorption at 1400 nm has almost vanished and the losses are closed to the limit values set by the Rayleigh scattering. At the same time, the zero chromatic dispersion has been shifted at 1470 nm, therefore this window is a subject of intense research in order to create an amplifier with the same performance as its erbium counterpart. The major part of this thesis is dedicated to the design and the construction of a thulium fluoride fibre amplifier able to work efficiently around 1470 nm. The natural low efficiency of the 1470 nm-thulium amplifying transition is due to the lifetime of the terminating metastable state, which is longer than the lifetime of the upper metastable state of the transition. Therefore, the problem of improving the achievable gain is related to the possibility of forcing a reduction of the ions population in the terminating level under a 790 nm optical pumping. The design of the amplifier, with its necessity of a cavity at 1.88 μm, was the subject of several investigations in order to fulfil all of the constraints existing. The creation of coated mirrors has been a successful approach in the past, but simulation shows the difficulty of coupling three different wavelengths efficiently inside a fibre. An alternative and cheaper approach with a straight industrial implementation is the creation of a ring cavity with two custom designed fibre chromatic couplers. The creation of this cavity will allow an amplifier and a laser to work simultaneously at different wavelengths, this effect is termed "co-operative lasing", and has an advantage over the existing technology in that it only needs pump lasers at a single wavelength in order to operate. A model has been created to describe the amplifier and make a simulation to the maximum cavity length compatible with our pumping power; moreover several details of the cavity design and construction are also reported.

The final part of the thesis is dedicated to the description of a thulium fibre amplifier optically pumped simultaneously by a Nd:Yag laser (1066 nm) and a Ti:Sapphire laser (800 nm). With this pumping scheme the amplifier achieves a high gain coefficient and thanks to the long lifetime of the thulium metastable levels high saturation values for the signal power are expected. A model similar to the one used for the amplifier working co-operatively with the laser has been created, and employed to optimise the powers of the two optical pumps involved, thereby obtaining the maximum efficiency in converting pump photons to signal photons.

Acknowledgements

I had the immense fortune, over the last four years, to work with Prof. John Donegan and his group. I owe to Prof. Donegan, as my supervisor, a personal debt in contributing to my formation from a human and scientific point of view. The many valuable hints and the constant encouragement that I have received have been eminently valuable. I would next like to thank Dr. Vincent Weldon for his support with the solid-state lasers. Most of all I wish to thank Mick Lynch who worked with me for the last four years, helping me in my first trials/errors phase in the lab and for being a constant source of inspiration. The help that I have received from Mick and his wife Tina when I really needed is unforgettable.

I would like to thank also all the senior staff members: Dr. Bradley, Dr. Rakovic and Prof. McCabe and the PhD students of the Semiconductor Photonics Groups: David, Matthias, Aaron, John, Torsten and Severine. They all gave and give an important contribution in creating an excellent working environment. A special thanks deserves Richard Phelan (now Dr. Phelan) who spread a contagious hurling passion, now I am a supporter of the Kilkenny hurling team.

I would also like to thank Mr. Gwenael Mazé for the preform and the doped fluoride fibres needed for this research.

A special thanks to: John Kelly, Maria Kinsella, Nigel Carroll, Ken Concannon, Dave Grouse, Mick O'Reilly and Pat Flanagan for the collaboration that I have received during the last four years.

The following have also all helped me out when it really counted: Fiacra Harte, Angus Harte, Sonia Haccius, Patrick Leonard and Cristiana Turchetti. I would like also to thank all the people in the Dublin lodge of the Theosophical Society for the spirit of universal brotherhood that they embrace.

Above all else, I'm indebted to my family back in Italy. The constant support from my parents Beppe and Leda and my brother Enrico, defies description.

List of Publications.

1) Optimisation of a two colour pumped Tm^{3+}-doped ZBLAN fibre amplifier at 1.49 μm.

Tessarin, S.; Lynch, M.; Donegan, J.F.; Maze, G.;

Submitted to Optoelectronics, IEE Proceedings, June 2005.

2) Tm^{3+}-doped ZBLAN amplifier at 1.49 μm with co-operative lasing at 1.88 μm

Tessarin, S.; Lynch, M.; Donegan, J.F.; Maze, G.;

Electronics Letters,

Volume 41, Issue 16, 4 August 2005, Page(s):899 – 900

3) Thulium doped ZBLAN fibre ring-cavity amplifier

S. Tessarin, M. Lynch, J. F. Donegan, G. Maze

Proc. SPIE Vol. 5825, p. 230-239, Opto-Ireland 2005: Optoelectronics, Photonic Devices, and Optical Networks Eds, Jun. 2005

4) Resonant energy transfer in praseodymium-thulium codoped ZBLAN fibre

Tessarin, S.; Lynch, M.; Donegan, J.F.; Maze, G.;

Optoelectronics, IEE Proceedings,

Volume 151, Issue 2, 26 April 2004 Page(s):129 – 132

.

Table of Contents

Chapter 1

Fibre Optics Telecommunications

1.1 Background

The new era in optical fibre communications can be traced to its beginning in 1970 when Kapron, Keck and Maurer of the Corning Glass Works fabricated a silica fibre having a 20-dB/km attenuation [1], overcoming the large attenuation present in the early fibres manufacturing process. During one decade, the technological improvement in the optical fibre production allowed an attenuation of 0.2 dB/km at 1.55 μm quite close to the theoretical scattering due to the lattice imperfection (Rayleigh scattering) to be achieved. At the same time, efficient narrow linewidth diode lasers were developed as optical sources and this gave the capability of achieving high data rates in optical transmissions.

Except for particular applications, modern optical communications operate with carrier frequencies located in the near infrared. Typically, wavelengths are in the range 1.3 μm to 1.55 μm. Early fibres had high levels of OH^- ions, which resulted in large absorption peaks occurring at 1.4 μm, 0.95 μm and 0.725 μm. These are the first, the second and the third overtones of the fundamental peak of water at 2.7 μm. [2] as shown in fig. 1.1.

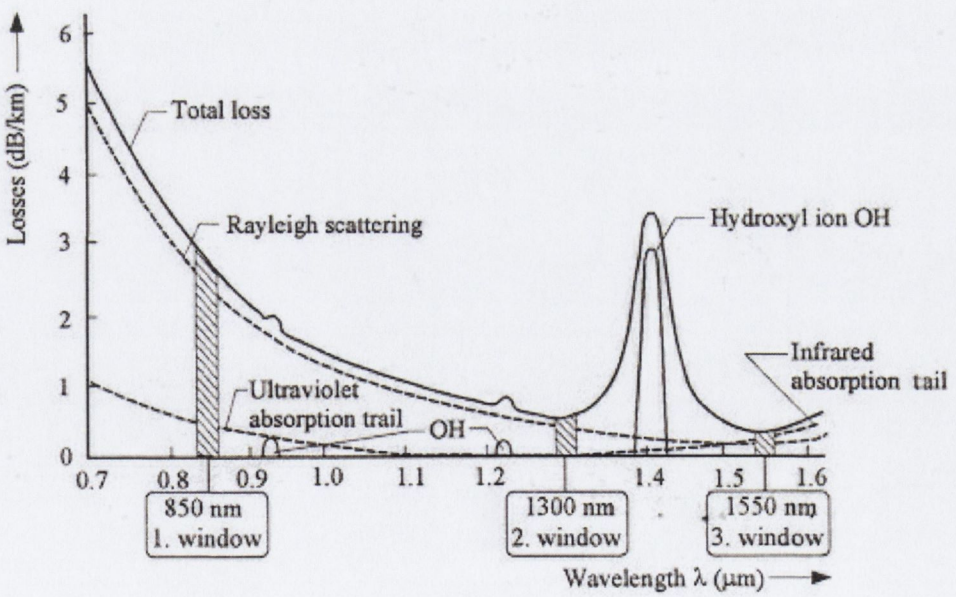

Figure 1.1: Attenuation of a standard silica fibre. Reproduced from [3].

Obtaining a large data transfer rate requires the possibility of fast modulation of the optical source, the pulses that travel along the fibre suffer from dispersion, which broaden the pulse along the communication line. This problem is known as *intersymbol interference* (ISI), where the pulse become broader as a function of the length of the fibre, due to the presence of dispersion, and ultimately overlap with neighbouring pulses creating severe problems in the detection process.

There are three mechanisms responsible for the pulse broadening:

1) Modal Dispersion, the guiding characteristic of the fibre is that it sets the number of modes that are allowed to propagate, each mode having a different propagation velocity along the fibre. A step index fibre with a large core is normally referred as a multimode fibre and gives rise to the largest modal dispersion. Shaping the refractive index in the core with a parabolic profile (graded index fibres) allows the mode to propagate in a helical path - this reduces the velocity mismatch among different supported modes. Single mode fibres are designed with a very small core cutting off all the higher modes, clearly no modal dispersion is present.

2) Material Dispersion, the refractive index depends on the wavelength and because a source is never completely monochromatic, different wavelength components travel with different speed. Standard silica fibres have zero dispersion at 1.3 μm (minimum value of group refractive index).

3) Waveguide Dispersion, the energy guided by the fundamental mode is divided between the core and the cladding. In a single mode fibre, as the wavelength increases, the field extends farther into the cladding and the propagation velocity decreases.

The sum of the material and waveguide dispersion is usually called chromatic dispersion. Old single mode fibres are usually non-dispersion shifted and the chromatic dispersion is zero at 1.3 μm (fig. 1.2), they are the most widely deployed and thus intended for use near 1.3 μm.

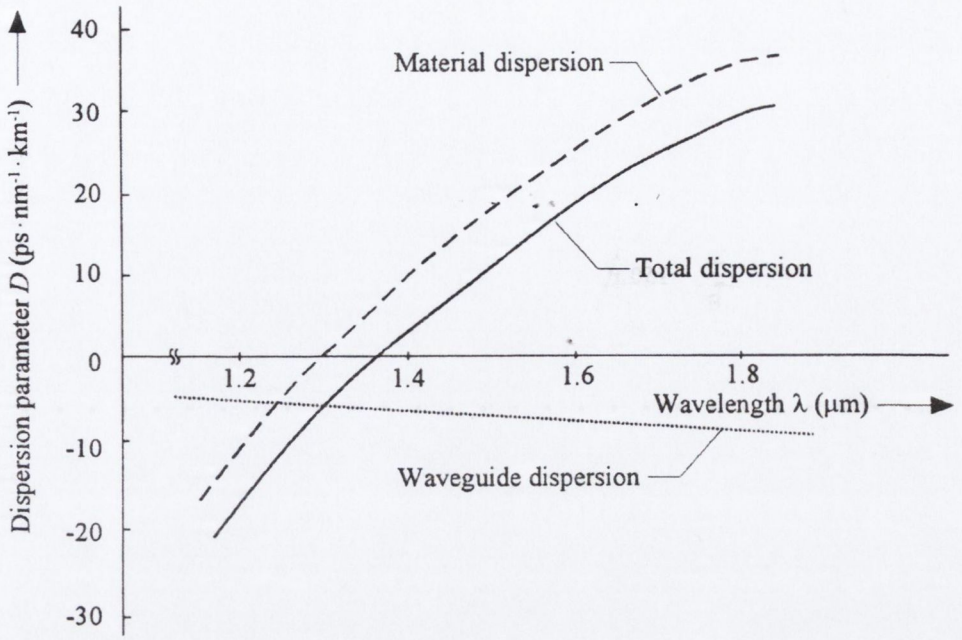

Figure 1.2: Dispersion of a standard silica single mode fibre. Reproduced from [3]

The idea of directly amplifying signals in optical fibre using doped amplifiers originated with Snitzer [4], and further refined by Payne and Reekie [5]. Erbium doped amplifiers allow efficient amplification around 1.55 μm, the discovery of the potential of erbium doped fibre as an optical amplifier opened-up the possibility of the use of the low loss silica windows at 1.55 μm. The performance/cost of erbium amplifiers still has been unmatched by any counterpart for a large numbers of reasons that makes erbium in silica possibly a unique system. Features such as: high gain with low pump power, low noise, low insertion loss, polarization insensitivity, and long transient dynamic linearity explain why such a device has become so popular.

The trend in fibre optic traffic is growing, and has massively increased in recent years, and it has become clear that a larger bandwidth will soon be needed. The erbium silica fibre amplifier has thus been shifted to operate up to 1.65 μm to the so called L band, but in order to exploit lower wavelength regions it was clear that this can only be achieved with major changes in both the transmission fibre and in the fibre amplifier. Figure 1.3 shows how the silica low loss region is divided into different telecommunication bands. As shown, standard silica fibres have an absorption peak centred at 1.4 μm due to the residual OH^- ions that have been difficult to remove.

However, recently new fibres commercially known as AllWaves[+] from Lucent have no residual OH^- absorption and are dispersion shifted to 1.45 μm.

Within one communication band, many channels spaced in a 100 GHz grid can usually be accommodated. Such a multiple wavelength system is referred to as being *wavelength division multiplexed*, and they are called *dense* when the grind spacing is 100 GHz or less, in contrast to earlier technology where the channels were further apart. Fibre amplifiers are essential since they recover the insertion losses that the signals face after being combined with the wavelength multiplexer.

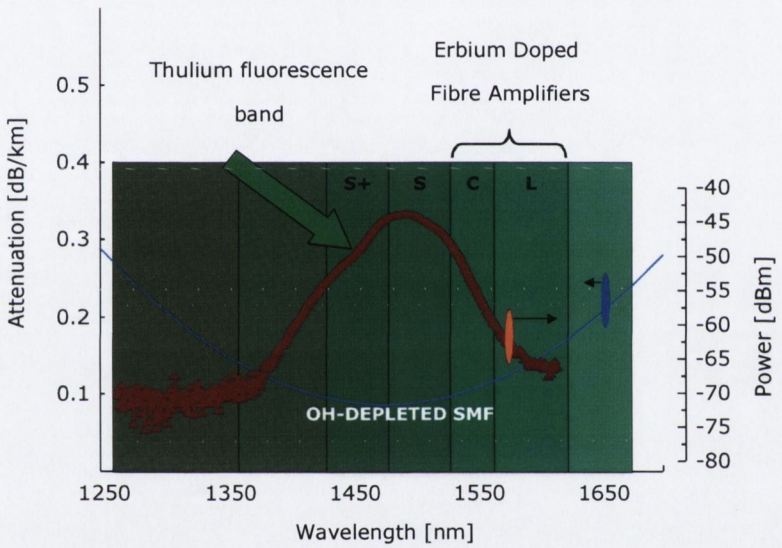

Figure 1.3: The low loss region of silica fibre is divided for convenience into several telecommunication bands: the blue curve shows the attenuation in the recently developed OH^- depleted fibre, whilst the red curve is the detected thulium fluorescence.

Thus the expansion in the use of dense wavelength division multiplexed (DWDM) in optical communications will be considerably helped by the presence of a fibre amplifier that can operate at wavelengths between 1.45 μm and 1.55 μm [7] and around 1.3 μm. Silica, however, appears to be a host with limited potential for other dopants that might work below 1.55 μm [7], mainly due to the rather high phonon energy and the degradation of pump or signal due to the excited state absorption that happens for instance in the Nd^{3+} /Pr^{3+} doped silica at 1.3 μm fibre amplifier. In 1975, a new

[+] http://www.lucent.com/press/0501/010529.nsb.html

zirconium fluoride based glass was developed [6],which shows the capability of incorporating higher ion concentrations. These glasses can be used to create highly efficient fibre lasers and amplifiers, for instance praseodymium (Pr^{3+}) and thulium (Tm^{3+}) are interesting dopants in fluoride fibres for amplifying signals respectively at around 1.3 μm and 1.47 μm.

Zirconium-based heavy metal fluoride glasses have lower phonon energy compared with silica and are promising, with longer lifetimes for the metastable energy levels and better efficiency for IR transitions. Thulium doped fluoride fibres, with strong fluorescence centred at 1.47 μm as shown in fig 1.3, appear to be a possible solution the active fibre in amplifiers which work in the S and S^+ telecommunication bands. Some of these amplifiers have already been reported and have shown high efficiency [8, 9].

Lifetime measurements of the two levels involved in the amplification process have revealed that the upper level of the amplifying transition has a shorter lifetime than the terminating level; this leads to rather poor performances [3]. In recent years, several attempts were made to reduce the impact of the self-terminating nature of the 1.47-μm transition in a thulium zirconium based fibre amplifier. A simple and elegant method of solving this is to pump one of the $^3F_4$ excited state absorption bands as depicted in fig. 1.4 A. An excited state absorption transition is located at 1.05 μm [8] and it is reasonably strong. However, at this wavelength the ground state absorption is low and a second pump is usually needed in order to raise the ions to the excited states making this amplifier difficult to design and produce. Moreover, high pump power diode lasers are not commercially available at 1.05 μm [10].

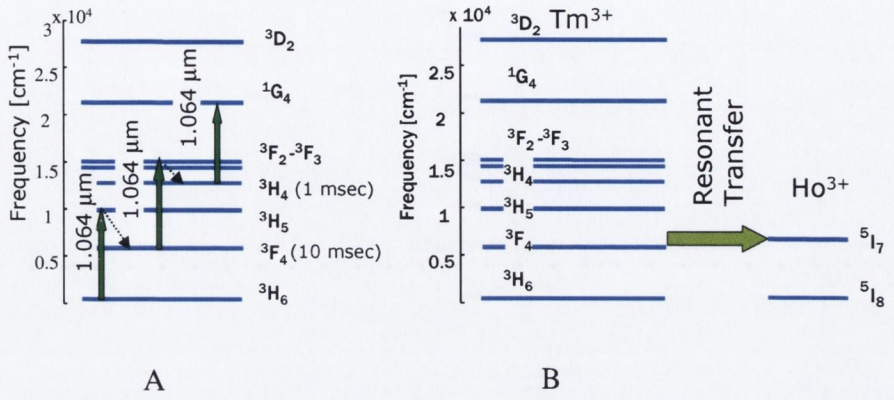

Figure 1.4: Proposed solutions in order to overcome the self-terminating nature of the 1.47-µm transition. A) A three photons upconversion process allows the depopulation of the terminating level of the 1.47-µm transition since the intermediate absorption strength is almost two orders of magnitude higher than the other two excited state absorptions. B) Codoping with a rare earth dopant where the first excited state is resonant with the Tm^{3+}:$^3F_4$

Another solution proposed was co-doping with another ion in order to depopulate the terminating level by resonant transfer. Holmium (fig 1.4.B) [11], and Terbium [12] had been revealed to be effective in reducing the lifetime of the terminating level. However, the reported performance has been shown to have a limited gain coefficient [13].
The solution that will be analysed in chapters 4 and 5 has been inspired by the work of [14] and [15], where a thulium fibre laser was operated simultaneously at around 1.8 µm and 1.4 µm by a so called cascade process. A way to artificially reduce the lifetime of the terminating level is to allow oscillations between the $^3F_4$ level and the ground state $^3H_6$ (1.88 µm). This solution makes possible single-wavelength pumping at 790 nm where thulium has a high absorption cross-section and where diode pump lasers are a mature technology that has been already developed for the erbium-doped amplifier [16].

1.2 Thesis synopsis

The present work is concentrated on the potential that praseodymium and thulium doped fluoride fibres have for the construction of optical amplifiers around 1.3 μm and 1.47 μm.

Praseodymium was studied while a thulium codopant was present in the fibre as a pump absorber, this gave an alternative to Pr^{3+} direct pumping but required a non-radiative energy transfer between Tm^{3+} and Pr^{3+}. In fact, the large cross-section of thulium ions at 790 nm effectively absorbs the optical energy. At this pump wavelength most of the thulium ions population is confined in the lower energy excited levels and no efficiently evidence has been found of a large energy exchange between the two ions.

Visible spectroscopy measurements, however, showed that appreciable energy transfers were possible between the higher excited levels. With Tm^{3+} and Pr^{3+}, concentrations (3000 ppm and 500 ppm) were selected to maximise the absorption and energy transfer while minimising self-quenching. At higher pump powers, upper states are also populated and the blue-green fluorescence emission peaking at 480 nm is clear evidence of appreciable energy transfer between the two ion species. The characterisation of the dynamics of the energy transfer was further explored by standard lifetime and frequency domain lifetime techniques, confirming the presence and allowing the measurement of the strength of the energy transfer.

Thulium in fluoride fibres showed low gain near 1.47 μm due to the lifetime of the excited levels involved in the pumping process. The terminating level of the transition has a longer lifetime than the upper level; this creates a serious difficulty in extracting a large gain. In order to directly measure the gain of the amplifier, a diode laser with a wavelength at 1.49 μm will be used; therefore we modelled the amplification at 1.49 μm for a thulium amplifier working cooperatively with a laser at 1.88 μm in order to have a direct comparison. The simulation shows a gain enhancement above the threshold for 1.88 μm lasing. The amplifier was then physically built with an all-fibre ring cavity needed in order to obtain the cooperative lasing, and thus validating the model results.

The optimisation of a power amplifier for a thulium upconversion pumping was also demonstrated; a double wavelength pumping has been shown to significantly improve the population upconversion in a thulium amplifier. We found the best ratio of the two pump powers involved in order to maximise the photon conversion efficiency.

1.3 Structure of the Thesis

The thesis is structured as follows:

Chapter 2

The chapter will provide an introduction to the structure of rare earth energy levels, a description of the properties of fluoride fibres and such relevant effects as energy transfer, concentration quenching and upconversion will be described mainly from a phenomenological point of view. An approximate model is presented for the lower energy levels of thulium ions, furthermore the determination of absorption and stimulated emissions; lifetime measurements, and excited state absorptions are reported.

Chapter 3

This chapter describes the detected resonant transfer in the Pr^{3+}-Tm^{3+} codoped fibre, and the characterization of the dynamics of the resonant transfer by standard and frequency domain lifetime techniques.

Chapter 4

This chapter is dedicated to the numerical model of the amplifier. The starting point is the guiding property of the fluoride fibres, which are essential for the determination of some of the parameters in the model. Then the description of the rate equations and the numerical integrations for the differential equations is reported.

Chapter 5

This chapter describes the ring fibre, thulium doped amplifier, its construction and the experimental results obtained, together with the comparison of the numerical model developed in chapter 4.

Chapter 6

In this chapter, the second prototype of the thulium amplifier where the optical pumping has been achieved by lasers at 800 nm and 1060 nm is presented. Its characterization and theoretical optimisation for power amplification will also be presented.

1.4 References

[1] F. P. Kapron, D. B. Keck, and R. D. Maurer, "Radiation losses in glass optical waveguides," *Appl. Phys. Lett.*, vol. 17, pp. 423-425, 1970.

[2] G. Keiser, *Optical Fibre Communications*: McGraw-Hill, 1983.

[3] G. Mahlke and P. Gossing, *Fiber Optics Cables*. Munich: Corning Cable System, 2001.

[4] E. Snitzer and R. Woodcock, 6, 1965, p.45, "Yb^{3+}-Er^{3+} glass laser," *Appl. Phys. Lett*, vol. 6, pp. 45-57.

[5] D. N. Payne and L. Reekie, "Rare-earth-doped fibre lasers and amplifiers," presented at Optical Communication, 1988. ECOC 88. Fourteenth European Conference on (Conf. Publ. No.292), 1988.

[6] M. Poulain, J. Lucas, and P. Brun, "Fluoride fibres from zirconium fluoride; optical properties of a fibre doped with Nd^{3+}," *Materials Research Bulletin*, vol. 10, pp. 243-246, 1975.

[7] R. Caspary, U. B. Unrau, and W. Kowalsky, "Recent progress on S-band fiber amplifiers," presented at Transparent Optical Networks, 2003. Proceedings of 2003 5th International Conference on, 2003.

[8] T. Komukai, T. Yamamoto, T. Sugawa, and Y. Miyajima, "1.47 μm band Tm^{3+} doped fluoride fibre amplifier using a 1.064 μm upconversion pumping scheme," *Electronics Letters*, vol. 29, pp. 110, 1993.

[9] J. Y. Allain, M. Monerie, and H. Poignant, "Tunable CW lasing around 0.82, 1.48, 1.88 and 2.35 μm in thulium-doped fluorozirconate fibre," *Electronics Letters*, vol. 25, pp. 1660-1662, 1989.

[10] B. Bourliaguet, F. Emond, S. Mohrdiek, A.-C. Jacob-Poulin, P.-Y. Cortes, and J. Lauzon, "Thulium-doped fibre amplifier using 1055 nm laser diode pumping configuration," *Electronics Letters*, vol. 38, pp. 447-448, 2002.

[11] R. M. Percival, D. Szebesta, S. T. Davey, N. A. Swain, and T. A. King, "Thulium sensitised holmium-doped CW fluoride fibre laser of high efficiency," *Electronics Letters*, vol. 28, pp. 2231-2232, 1992.

[12] T. Sakamoto, M. Shimizu, M. Yamada, T. Kanamori, Y. Ohishi, Y. Terunuma, and S. Sudo, "35-dB gain Tm-doped ZBLYAN fiber amplifier operating at 1.65 μm," *Photonics Technology Letters, IEEE*, vol. 8, pp. 349-351, 1996.

[13] T. Sakamoto, M. Shimizu, T. Kanamori, Y. Terunuma, Y. Ohishi, M. Yamada, and S. Sudo, "1.4-μm-band gain characteristics of a Tm-Ho-doped ZBLYAN fiber amplifier pumped in the 0.8-μm band," *Photonics Technology Letters, IEEE*, vol. 7, pp. 983-985, 1995.

[14] R. Allen, L. Esterowitz, and I. Aggarwal, "An efficient 1.46 μm thulium fiber laser via a cascade process," *Quantum Electronics, IEEE Journal of*, vol. 29, pp. 303-306, 1993.

[15] R. M. Percival, D. Szebesta, S. T. Davey, N. A. Swain, and T. A. King, "High effcient cw cascade operation of 1.47 μm and 1.82 μm transition in Tm^{3+} doped fluoride fibre," *Electronics Letters*, vol. 28, pp. 2063-2065, 1992.

[16] B. Pedersen, W. J. Miniscalco, and S. A. Zemon, "Evaluation of the 800 nm pump band for erbium-doped fiber amplifiers," *Lightwave Technology, Journal of*, vol. 10, pp. 1041-1049, 1992.

Chapter 2

Optical Properties of Rare Earth Ions

2.1 Introduction

The rare earth atoms can be divided in two series; the first called the Lanthanides goes from the atomic number 58 (Cerium) to number 71 (Lutetium). The other series is called the Actinides, usually they are unstable and radioactive and therefore rarely studied in optical spectroscopy. The Lanthanides possesses the same electronic outer structure configuration: filled shells $5p^2 5p^6 6s^2$ as shown in fig. 2.1.

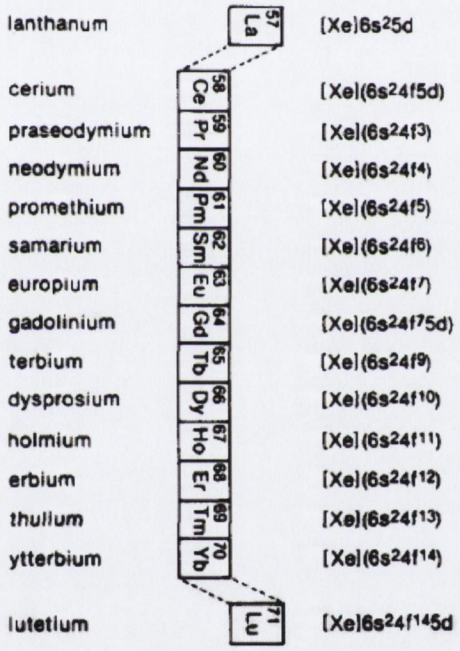

Figure 2.1: The 15 rare-earth elements showing the atomic number and electronic configuration. [Xe] stand for the electronic configuration of the noble gas Xenon. Reproduced from [1].

The optical properties are dictated by electrons in the 4f shell, which are progressively filled with the increase in the atomic number along the series, and the optical transitions are associated with excitation and relaxation of the 4f-electrons. When incorporated into solids, the rare-earths are usually found in the more commonly the 3+ charge state with the exception of Europium, with the loss of the two 6s and one 4f electrons, this

however leaves the outer 5s and 5p shells intact. The shielding effect provided by the outer filled shells is associated with the unique properties that rare-earth ions, have in respect to transitions metals for instance.

The optical electrons are exposed to a reduced electric field created by the host's ions and the rather weak interaction with the host material, making them behave like an isolated ion. Therefore 4f-transitions absorb and emit as sharp lines in many visible and IR wavelengths compatible with the transparency of the host material itself. In the past, rare-earth spectroscopy measurements have been performed primarily in crystals [2], mostly on host-based alkaline fluorides like CaF_2. These measurements showed the possibility of establishing laser oscillations in large numbers of 4f-transitions spanned across the visible and IR wavelengths. During the early 1960's a series of experiments showed the possibility of achieving pulse laser oscillation in rare-earth doped crystals fluorides and $CaWO_4$ in the mid infrared regions at liquid nitrogen temperature [3]. Lately vitreous hosts have been also doped with rare-earth ions. This research has led to low loss multimode silica fibres and recently, single-mode doped silica fibres.

The low symmetry of host sites in glass usually causes Stark splitting in the absorption and emission fluorescence. The degeneracy that exists in the energy levels is removed and the hyperfine structure is often visible. The broadening mechanism of the optical transition in rare-earth doped glass is complicated by multiple broadening effects, and moreover is glass dependant so most of the conclusions are essentially empirical. The broadening is due to two distinct causes: *homogenous broadening*, is related to the distribution of the energy of the phonons which take part in the absorption or emission processes; for this reason it is also known as phonon broadening. The second cause is referred to as *inhomogeneous broadening* and it is due to the unique crystal field that each ion experiences in a random distributed lattice.

The distribution of available host sites in glass results in much broader fluorescence spectra in the glass compared with crystalline materials. Moreover the light confinement allows long interaction length in silica fibres and easily controllable thermal effects. This makes possible the construction of simple Fabry-Perot cavity diode laser pumped fibre lasers which usually show diffraction limited beam quality, possible tune-ability and low threshold.

The usefulness of silica fibres was limited by the high phonon energy of the glass, which reduces the lifetime of the metastable levels and thus their fluorescence efficiency by non-radiative relaxation. New glasses based on zirconium fluoride showed reduced phonon energy and a wider transmission band allowing more efficient laser oscillation across the visible and IR regions.

The aim of this chapter is to introduce the electronic proprieties of the general rare-earth ion, and the theory that describes the interaction with an external electromagnetic field. The rest of the chapter is allocated to the presentation of a thulium analytical model and some spectroscopic measurements.

2.2 Electronic Properties

The familiar Schrödinger equation can be solved for hydrogen-like atoms. The atomic potential in such Hamiltonians is symmetric for rotations, and the angular momentum commutes with the Hamiltonian. This provides a natural basis in order to obtain the eigenvalues of the Hamiltonian.

The general case for an atom with many electrons is rather more complicated: the Schrödinger equation[1] includes a repulsive Coulomb potential and the spin-orbit interaction (L-S) for an atom of atomic number Z and N electrons as:

$$\left[-\frac{\hbar^2}{2m_e}\sum_{i=1}^{N}\nabla_i^2-\sum_{i=1}^{N}\frac{Ze^2}{r_i}+\sum_{i>j=1}^{N}\frac{e^2}{r_{ij}}+\sum_i\xi(r_i)L_iS_i\right]\psi(\vec{r})=E\psi(\vec{r}), \tag{2.1}$$

where $r_{ij}=\left|\vec{r_i}-\vec{r_j}\right|$ and $r_i=\left|\vec{r_i}\right|$ are respectively the distance between two electrons and the distance of the *i*-electron to the nucleus.

The repulsive Coulomb term cannot be treated as a perturbation, so in the Schrödinger equations a dominant symmetric $V_i(r_i)$ potential is introduced, which represent the mean field due to the spherical charge distribution of the other inner shells electrons termed the *central field approximation*. The problem is solved with an self-consistent method called Hartree-Fock, the wave function is correctly anti-symmetric and a particular labour intensive set of integral-differential equations can be solved [4]. The previous solutions are constructed from hydrogenic states, where L the total orbital angular momentum and S the total spin are both "good quantum numbers". The vector model of the atom is therefore appropriate and L and S can be added to form the total

[1] cgs units

angular momentum J. The labelling of the levels is expressed with the Russell-Sanders scheme like $^{2S+1}L_J$ using for L the equivalent spectroscopic letter (s,p,d,f,....).

The problem is now reduced to taking into account the residual Coulomb effect due to the mutual interaction between 4f-electrons and the spin-orbit interaction. The former partially lifts the degeneracy presented in the central field approximation and the energy states show a dependency on both L and S.

Next in the hierarchy is the spin-orbit coupling that lifts the degeneracy in the total angular momentum and splits the LS terms into J levels which can be solved using an intermediate coupling calculation by simultaneously diagonalising the spin-orbit and the electrostatic interaction.

In this way it is possible to calculate the energy of the excited state levels of rare-earth ions, moreover if U^t are the reduced matrix found by simultaneously diagonalising the electrostatic and the spin-orbit interaction between two state characterized by the set of the quantum numbers *a* and *b,* then:

(2.2) $$\langle b \| U^t \| a \rangle .$$

These values are almost independent of the host and they are tabulated in [5]. Section 2.4 will report how to take into account the host effect by introducing three phenomenological parameters with the aid of the Judd-Ofelt analysis.

2.3 Optical Properties of Rare-Earth Ions

The 4f-electrons can interact with an incoming electromagnetic field. If the frequency of the electromagnetic field is comparable with the frequency spacing between the ground state and an excited state, then a photon can be absorbed. It is useful to define the oscillator strength $S_{a\to b}$ of a general transition between the two multiplets *a* and *b* given by the expectation value of the dipole operator $\vec{D}$:

(2.3) $$S_{a\to b} = \sum_{i,j} \left| \langle b_j | \vec{D} | a_i \rangle \right|,$$

where the summation is over all the multiplet components. Electric dipole operator transitions are usually more intense than magnetic, nevertheless magnetic components are in some cases presented. The dipole operator has an odd parity while the energy states have all the same parity, so this seems in contradiction with the selection rules, however, the mixed L-S levels are not completely pure, as previously specified. This

fact can be attributed to the low degree of symmetry associated with the rare-earth site in the glass medium and therefore the total oscillator strength is usually approximated with the electric dipole oscillator strength.

The spontaneous emission rates from a level *a* to a level *b* can be calculated from the Poynting vector which in the classical limit is proportional to the oscillator strength [6]:

$$A_{a\to b} = \frac{64\pi^4 \upsilon^3}{3hc^3(2J+1)} \chi_{ed} S_{a\to b}, \tag{2.4}$$

where J is the quantum number of the total angular momentum of the initial state *a*, $S_{a\to b}$ is the electric oscillator strength and the electric local field correction factor is $\chi_{ed} = n(n^2+1)^2/9$ where n is the refractive index.

For an energy level *a* the spontaneous emission lifetime τ_a is define as the inverse of the sum of all the radiative spontaneous emission rates originated from the considerate energy level, i.e.:

$$\frac{1}{\tau_a} \equiv \sum_j A_{a\to j}.$$

The branching ratio is therefore define as:

$$\beta_{a\to b} = \frac{A_{a\to b}}{\sum_j A_{a\to j}} = \tau_a A_{a\to b},$$

and gives the relative probability of spontaneous decay for a particular transition $a \to b$.

The transition cross-section σ specifies the character of the interaction of the atom with the radiation, its integral (in m^2-Hz) is proportional to oscillator strength defined in the eq. 2.3:

$$S_{a\to b} \propto \int \sigma(\upsilon) d\upsilon. \tag{2.5}$$

Usually it is more convenient to work with a dimensionless quantity:

$$f_{a\to b} = \frac{8\pi m \upsilon}{3hc^3(2J_a+1)} \chi_{ed} S_{a\to b}, \tag{2.6}$$

so the measured cross section can be connected to the dimensionless oscillation strength as:

(2.7) $$f_{a\to b} = \frac{mc}{\pi}\int \sigma(\upsilon)d\upsilon .$$

It is possible to connect in an empirical way the absorption oscillation strength to the reduced matrix elements of the equation 2.1 as:

(2.8) $$S_{a\to b} = e^2 \sum_{t=2,4,6} \Omega_t \left|\langle b\|U^t\|a\rangle\right|^2 ,$$

this method is called Judd [7] -Ofelt analysis [8]. In practice, the three empirical parameters Ω_2, Ω_4, Ω_6, are obtain by performing a least-squares fit to the integrated absorption bands from the measured absorption spectrum. Once the parameters are obtained it is possible to determine the strength of any radiative transition for the specific dopant-host combination.

Mc Cumber theory stated that the relationship between the emission and the absorption spectra [9] when the time required to obtain thermal distribution is short compared to the lifetime of the level is:

(2.9) $$\sigma_e = \sigma_a e^{\left(\frac{\varepsilon - h\upsilon}{kT}\right)},$$

which means that the stimulated emission cross-sections σ_e and the absorption cross-sections σ_a ,are scaled with respect to each other by a temperature-dependent parameter ε, which is the net free energy required to excite one ion in the transition involved at the temperature T [10].

2.4 Homogeneous and Inhomogeneous Broadening

The effects of line broadening mechanisms in glasses when compared to crystals are evident form figure 2.2. If the crystal and glass have similar chemical composition, the oscillator strength of optical transitions is similar and so the integral of the cross-section for the glass and crystal should be similar too. The difference is that the cross-sections have lower peak values but larger widths for rare-earths in glass as opposed to the case of crystals.

Homogenous broadening (or phonon broadening) takes place because energy exchange in a transition between the two energy levels may include the creation or annihilation of a phonon. It has a Lorentzian type profile therefore, it is clear that this type of broadening is due to the finite lifetime of the metastable state:

(2.10) $$\sigma_a = \frac{1}{\pi} \frac{\Gamma}{(\upsilon - \upsilon_{eg})^2 + \Gamma^2},$$

where υ_{eg} is the frequency of the oscillating dipole and Γ is the full width at half maximum of the resonance.

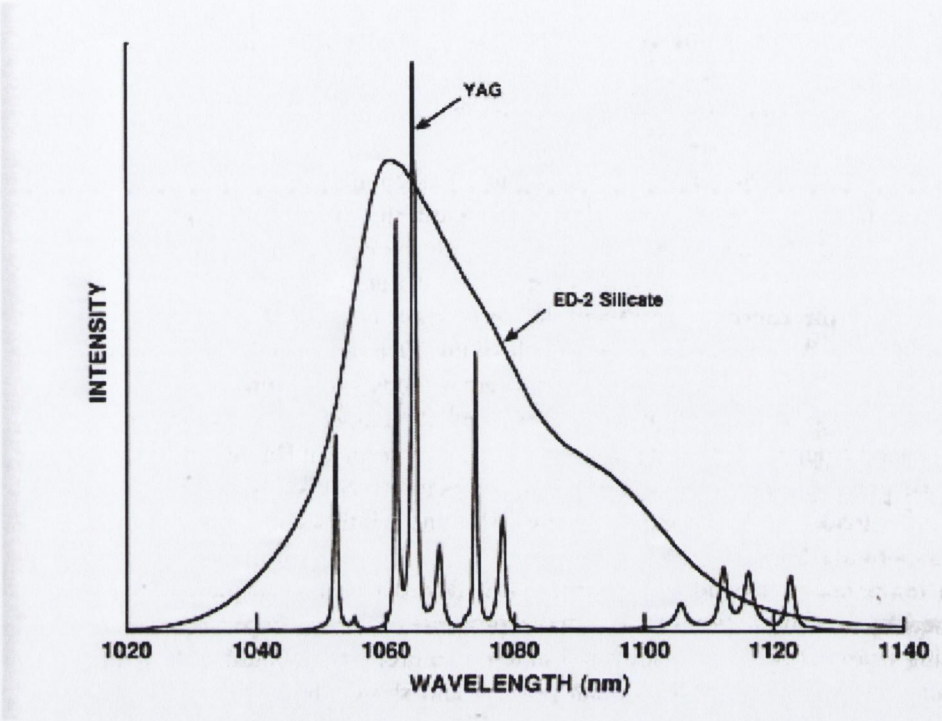

Figure 2.2: Comparison of the emission spectra for Nd^{3+}-doped YAG and Nd^{3+}-doped silicate glass, reproduced from [11]

The inhomogeneous broadening is due to the variation in the host field that each ion in a site glass experiences. The absorption lineshape is Gaussian:

(2.11) $$\sigma_a = \frac{1}{\sqrt{2\pi}\Delta} e^{\left(-\frac{(\upsilon-\upsilon_{eg})^2}{2\Delta}\right)^2},$$

similarly to the previous case Δ is the transition linewidth centred at the frequency υ_{eg}

The observed lineshape is usually complex and cannot be fitted to any of the two broadening types. Observed lineshape in glasses will be a convolution of homogenous and inhomogenous broadening.

The difficulties in obtaining an analytical function in order to fit an absorption or an emission cross section can be overcome by the introduction of the concept of the lineshape function defined as:

$$g(\upsilon) = \frac{\sigma(\upsilon)}{\int \sigma(\upsilon) d\upsilon}$$

However it is not possible to directly measure cross sections, usually a spectrometer measures intensity per unit wavelength so it is more convenient to define the effective line width as:

$$\Delta\lambda_{eff} = \frac{\int I(\lambda) d\nu}{I(\lambda)}$$

So the lineshape function can be rewritten as:

$$g(\upsilon) = \frac{\lambda^2}{c\Delta\lambda_{eff}}. \tag{2.12}$$

The important Fuchtbauer-Landenberg equations connect the emission lineshape with the stimulated emission cross sections and are derived directly from Einstein's A and B coefficients [12]:

$$\sigma_{21} = \frac{\lambda^2}{8\pi n^2} A_{21} g(\upsilon), \tag{2.13}$$

so it is possible to scale the emitted fluorescence to the value of the cross-section while the relative magnitude of the cross-section detuned from its peak value is taken into account by a normalized lineshape function.

The equivalent analysis for the absorption lineshape is less useful since, as will be shown, absolute absorption cross-sections can be directly measured.

2.5 Energy Transfer

Interaction can occur between ions of the same species for a monodoped fibre or between atoms of different species in case of a codoped or multidoped fibre. At low concentrations, ions could be thought to be isolated and with the increase in concentration the two ions become close enough to allow a sharing of energy. Dexter [13] originally proposed the theory for the energy transfer: the interaction between the two ions is described by an interaction operator which decreases with the interionic distance R according to $1/R^s$ (s is an integer) and the short range exchange $exp(-R/R_b)$ where R_b is Bohr radius. The electric and magnetic dipole varies as $1/R^3$ and they dominate at large ion separations in the multipolar expansion. The transition probability is calculated with Fermi's golden rule and is proportional to the square of the

Hamiltonian matrix elements; this means that the transition probability decreases as $1/R^6$. However even if the interaction mechanism is usually known, it is not possible to calculate accurately the dynamics of the transfer, therefore a semi empirical treatment is usually employed.

When energy transfer takes place between two ions, the type of ion that is optically excited is referred to as the donor and the one that receives the excitation is called the acceptor. The donor absorbs the photon of the optical pump and transfers its energy to a nearby acceptor (fig 2.3 a), this process is usually used for sensitising materials as in case of Er^{3+}, Yb^{3+} where poor absorption cross-section of Er^{3+} at 800nm is enhanced by the Yb^{3+} strong absorption in order to obtain amplification at 1550 nm [14].

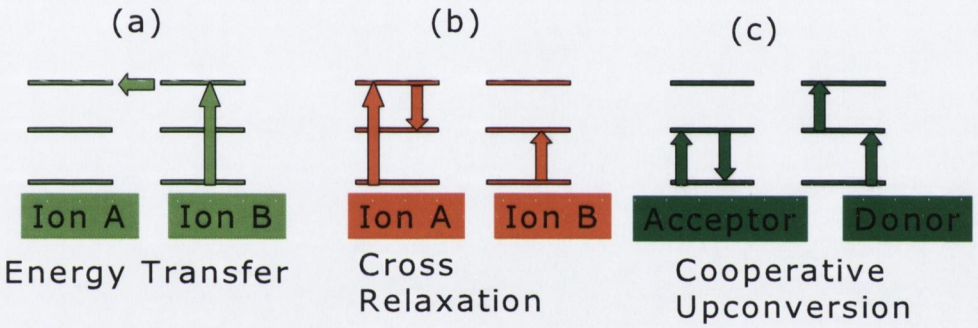

Figure 2.3: The possible resonant transfer mechanisms between ions in a rare earth fibre.

Inokuti and Hirayama [15] modelled the decay with time of the donor fluorescence after a laser pulse as a function of the distance dependence of the transfer rate between centres. In the case of multipolar interaction between donors and acceptors when both fluoresce, the ratio of the donor fluorescence to the total fluorescence intensity is given by:

$$R(t) = \frac{I_D(t)}{I_D(t) + I_A(t)} = \exp\left[-Wt\right]^{\gamma}$$

where the I_D (I_A) is the integrated intensity of the donor (acceptor) fluorescence and W is the mean transfer rate. The exponent γ takes into account the order of the multipolar expansion involved.

Other ion-ion interactions, which happen according to selection rules, can be divided into two classes of categories: Cross-relaxation and Cooperative Upconversion. Cross-relaxation is the process in which an ion in the excited state transfers part of its excitation to a neighbouring ion as shown in fig.2.3 (b).

Cooperative upconversion can be thought of as the inverse of cross relaxation in this case both ions are in an excited state (fig. 2.3, (c)).

An example of interaction between ions of the same species is the degradation of the lifetime of the excited levels with the increase of the doping concentration. In Pr^{3+}doped fibres, for instance, this is a well-known and important effect that usually fixes the upper limit of concentration at 500 ppm. The quenching in the lifetime is plotted in fig. 2.4 versus the concentration of the praseodymium in ZBLAN glass.

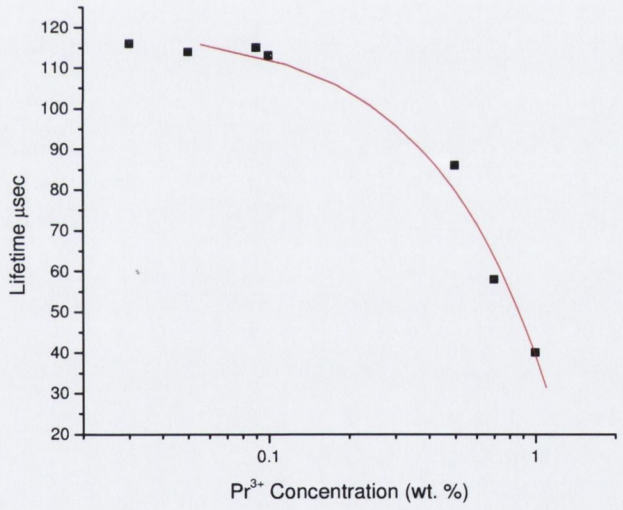

Figure 2.4: The quenching of Pr^{3+} lifetime starts at 200 ppm however until 500 ppm it does not strongly influence the lifetime. From reference [16]

The empirical formula that relates the observed lifetime τ_{obs} to the ion concentration ρ [17]:

$$\tau_{obs} = \frac{\tau_0}{1+\left(\frac{\rho}{Q}\right)^p},$$

where τ_0 is the lifetime in the limit of zero concentration and Q is the quenching concentration, an empirical parameter determined from fitting the experimental data. The exponent p represents the dominant relaxation mechanism, in the case of cross-relaxation its value is 2.

2.6 Fluoride Fibre

Fluoride glass is based on tetravalent, trivalent and bivalent fluorides, usually known as heavy metal fluorides. The more common glasses for telecommunications devices are often made from heavy metal Zirconium (Zr) tetravalent fluoride salt, the glass is called *ZBLAN* after the acronym of the constituent ions (ZrF_4 –BaF_2 –LaF_3 -AlF_3 –NaF). A key difference between silica fibre and fluoride fibre is in the phonon energy. In the silica fibre, the phonon energy is on the order of 1100 cm^{-1} while in the fluoride fibre, the phonon energy is around 580 cm^{-1}. This shifts the absorption edge to wavelengths up to 5 μm in the fluoride glasses. With lower phonon energy, these types of glasses have a reduced non-radiative decay compared with silica glass. The probability for the non-radiative decay is:

$$W_{NR}=B\, e^{-\alpha\Delta E},$$

where ΔE is the energy gap separating the two levels involved in the decay and the two phenomenological parameters B and α are used to take into account the host properties and are independent of the active ions added. In a lower phonon energy material, the ΔE is usually bigger than in silica glass and the non-radiative decay rate is then smaller. This gives stronger radiative emissions and a longer lifetime for the ions. The two parameters B and α are determined experimentally and the values tabulated.[2]

[2] ZBLAN: $B=1.6\ 10^{10}\ s^{-1}$, $\alpha=5.19\ 10^{-3}$ cm.

Table 2.1: Composition and physical properties of the ZBLA glass used in this thesis.

Composition (molar fraction)	ZrF_4 (57), BaF_2 (34), LaF_3 (5), AlF_3 (4)
Glass Transition Temp.	300 ^{0}C
Melting Temp.	550 ^{0}C
Linear expansion coefficient	16 10^{-6} K^{-1}
Refractive Index	1.519
Spectral Window (T=90%, 2mm thick)	0.25-6.5 μm

Fluoride glasses belong to the general family of halide glasses, the binding force of the molecules are mostly ionic, in contrast for instance with silicate glass which are covalently bonded. This has the effect that dopants in fluoride usually emit and absorb at shorter wavelengths than for the same dopant in covalent glasses. Moreover Ω_2 in the Judd-analysis is correlated with the degree of covalency in the glass, fluorides have a tendency to have Ω_2 smaller than silicates.

In conventional laser glass, a high concentration of non-bridging oxygen groups allow an easier incorporation of rare-earth ions. However in silica based optical fibres, a rigid structure exists and there is a lack of non-bridging $Si\text{-}O^-$ groups which gives a low number of networks modifiers that can be replaced by rare-earth ions. This makes the coordination of rare-earth ions difficult and it contributes to a lack of solubility, which usually leads to clustering in the glass. Clustering is particularly harmful since it contributes to local concentration quenching and to working with a low doping concentration [18]. Alternatively, fluoride allows a higher concentration due to the ionic nature of its lattice network; the rare-earths ions usually substitute for LaF_3, greatly reducing the previously mentioned clustering effect.

The methods currently used for the fabrication of rare-earth doped fibres can be divided into three main groups. The first two methods, called vapour phase and liquid phase concern rare-earth doped fibres based on silica glass [19], while the third method concerns fluoride glasses and consists of a liquid phase, melting/casting process. The methods used for silica are inadequate for fluoride based fibre due to a relative high viscosity near the melting point [20]. This creates the necessity to prevent the formation of crystallites because the viscosity decreases rapidly above the transition temperature which is very close to the crystallisation temperature (difference between the two

temperatures $\square 90^0 C$). There are several methods [21, 22] which allows the preparation of a preform from which a fibre can be drawn; a common feature is that they start from melted fluoride powder and cast the preform in an inert crucible and atmosphere (refractive index modifier is added to the core or the cladding) at temperature of the order of $700-800^0 C$. Then the fibre is drawn from the preform in a temperature and speed controlled fibre drawing furnace. The composition and the physical properties of the glass used in the fabrication of the fibres studied in this thesis are reported in table 2.1. However the differences in the final fluoride fibre composition are not particularly relevant in this context. The mechanical properties can be altered by changing the final composition of the glass (see reference for more details [23]) but the optical behaviour of the doped ions are not particularly altered due to the shielding effect described in the section 2.3.

There are several disadvantages in working with fluoride fibres. Fluoride fibres are rather more brittle than silica and more sophisticated technology is needed to handle them. They are also more expensive due to the higher cost of the materials involved in the fabrication. Fluoride fibres are usually coiled around a bobbin, therefore the surface experiences a tensile stress which is generally more severe than for silica fibres. Furthermore, fluoride fibres are subjected to moisture damage, these effects normally have a contribution in reducing the lifetime of fluoride fibre devices [24].

2.7 Introduction to Spectroscopy in Rare-Earth Doped Fibre

Even if many parameters measured for crystalline material are very close to those of heavy metal fluoride glass from which our fibres are made, there is a substantial difference in spectroscopic measurements. The guided nature of the light in glass fibre material substantially alters the spectra. Usually in doped fibre production, preforms are made before the fibre itself is drawn, therefore spectroscopic measurements are carried out mainly on preforms because they are easier to manipulate.

However sometimes it is not possible to have a preform, so the measurements must be conducted directly in the fibre. Due to the guiding nature of the light in the fibre, observations are rather different from crystals or preforms where there is no confinement. Moreover, the fluorescence emitted is also guided and due to its incoherent nature only the solid angle part emitted under the critical cone is detected.

The fractional part of the fluorescence that is guided in the fibre is proportional to the capture angle $\Delta\Omega$ defined as:

$$\Delta\Omega = \pi\left(\frac{n_c^{\,2} - n_{clad}^{\,2}}{n_c^{\,2}}\right), \tag{2.14}$$

where n_c is the core refractive index and n_{clad} is the cladding refractive index.

It is common to specify the fibre with the value of its *numerical aperture* NA, a terminology borrowed from lens design which represents the maximum acceptance angle of the fibre and it describes the capability of the fibre in gathering the light as:

$$NA = \sqrt{n_c^{\,2} - n_{clad}^{\,2}}\,. \tag{2.15}$$

The eq. 2.14 can be rewritten in terms of NA as:

$$\Delta\Omega = \pi\left(\frac{NA^2}{n_c^{\,2}}\right), \tag{2.16}$$

The fluorescence itself can also be subjected to re-absorption and stimulated amplification, making fundamental fluorescence measurements rather more complicated.

Some limits have to be considered in order to define the possible spectroscopy measurements that can be carried out and the relative accuracy that can be expected. Doping levels in a fibre are naturally lower than in a crystal, especially for fibre designed in order to be used as an amplification medium. Many dopants such as Pr^{3+} have a low doping threshold where non-radiative relaxation starts to reduce the lifetime of the excited level, making the doped fibre a rather dilute system. If the fibre is short, stimulated amplification of the fluorescence and re-absorption are consequentially low so they can be neglected, however this leads to very low fluorescence power so a high sensitivity spectrometer is needed. The fluorescence power detected is usually proportional to the acceptance angle (eq. 2.16) and it is quadratic with respect to the NA, and is also proportional to the mode volume which decreases with the NA. A method of checking if the system is short enough is to reflect back the fluorescence into the fibre; if it is twice the power of that detected from a single pass then the system can be considered thin. A 10 cm fibre length is usually so short that most of the excitation radiation is not absorbed and the fluorescence lineshape is not affected by the confinement.

Another important consideration is that a fibre is purely single mode only above a certain wavelength, below this wavelength higher modes are supported. Therefore, the fibre exhibits a multimode nature and so absorption lengths are affected by the distribution of the multimode nature of the electric fields. The measurements reported in this chapter are performed in fibres which have been recorded at wavelengths where the fibre supports a single mode, which means that they can be scaled to the true value, usually by a constant factor. The constant factor is commonly referred to as the confinement factor and represents the fraction of the guided light which is propagated in the core with respect to the total power that propagates either in the core or in the cladding.

In this chapter, a method of measuring the thulium stimulated emission cross-section around 1.47 μm and the absorption cross-sections for three of the IR transitions will be demonstrated. These values are fundamental in the development of a phenomenological model used in the rest of the thesis. Since thulium has a central role in this thesis the spectroscopic analysis in ZBLA in the region between 800 nm up to 1.7 μm will be presented.

2.8 Thulium

The energy level diagram of Tm^{3+} is shown in fig. 2.5. The calculation of the thulium energy levels is more problematic with respect to lighter rare-earth ions. As the atomic number increases, the contribution of spin-orbit coupling increases more rapidly than the electrostatic interaction between 4f-electrons giving a more significant LS mixing. In the first attempt levels $^3F_4$ and $^3H_4$ were reversed, since the spin-orbit contribution was underestimated. Recent calculations, however, proved that the correct labelling is the one reported figure 2.5 [25]. Although recent literature reports the correct labelling system, it is not infrequent to find the reversed one in older books or articles. Thulium spectroscopy in fluoride glasses is well described in the literature: the transition between $^3F_4 \rightarrow {}^3H_6$ peaks at 1.850 μm with a broad strong emission band and a measured lifetime of the level between 9.8 ms and 10.2 ms.

The transition $^3H_6$ to $^3H_4$ has an absorption peak at 790 nm and a strong absorption cross-section ideal for optical pumping with GaAs diode lasers or solid-state titanium-sapphire lasers. Transitions to the lower level are largely dominated by the radiative relaxation to the ground state with branching ratio of 90 %, while 9% decay to the $^3F_4$

peaking at 1.47 μm with 1% decaying to the level $^3H_5$ that emits a fluorescence at 2.3 μm. The lifetime of which transition has been measured to be around 1.6 ms.

The transition at 1.47 μm is located at wavelengths that are important for optical fibre communication, however efficient amplification is prevented by the longer lifetime of the terminating level with respect to the upper level of the transition. Colloquially, this situation is expressed as the "bottleneck effect" which suggests the idea that under the steady state conditions, a large part of the electron population is lying in the terminating level of the 1.47 μm transition and only at high pump rates is a small population inversion appreciable. This topic will be further discussed in chapter 4, 5 and 6 where two different solutions in order to overcome the problem will be presented.

Another effect in rare-earth doped fibres is called upconversion; in the presence of a populated excited state with a rather long lifetime, a second photon can be absorbed from the excitation (Excited State Absorption or ASE). A three-photon upconversion process is also possible and this has an important role as a pumping mechanism in a thulium doped amplifier as will be presented in chapter 6.

Upconversion processes related to a single wavelength has the effect of producing fluorescence close to the double of the frequency of the pump radiation, usually in the visible with blue-green fluorescence that glows from the fibre.
The radiative lifetime for the $^1G_4$-transitions is of the order of 0.68-0.78 ms and the main decay channel is to the ground state (46%) with fluorescence at 480 nm. This transition is responsible for the weak blue fluorescence that can be seen in single pumped 790 nm thulium doped fibre. The ESA centred at 780 nm is weak and usually does not contribute to creating a large population in the $^1G_4$ level.

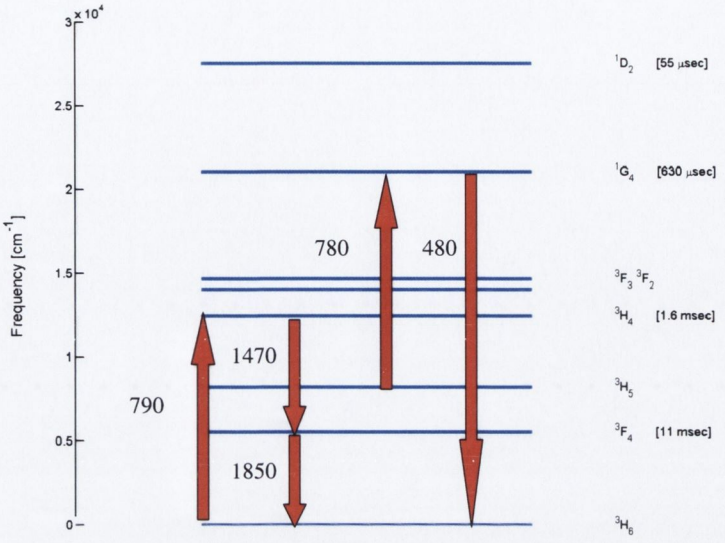

Figure 2.5: Thulium energy levels and their energy in cm^{-1}. A possible transition wavelength can be calculated from the difference in energy between the two levels involved. All the wavelengths are express in nm.

2.9 Praseodymium

Praseodymium received much attention as a promising candidate for an amplifier at 1.3 μm in the zero dispersion telecommunication window, the energy level is shown in fig. 2.6. Moreover, due to a large number of visible transitions it has been considered a good dopant for visible lasers.

The main drawbacks are due to the low absorption at 1 μm ($^3H_4$-$^1G_4$ transition) and the concentration quenching that appears at low doping levels. The decay $^1G_4 \rightarrow ^3H_5$ produces fluorescence around 1.3 μm. This transition, in contrast to the neodymium 1.3 μm-transition, is free from excited state absorption at 1.3 μm, so theoretically a high gain can be achieved.

The high energy multiplet ($^3P_0$, $^3P_1$, $^1I_6$) decays at several wavelengths: 610, 635, 695, 715, 885 and 910 nm [26], 490, 520 540nm [27]. Many of these transitions are suitable for laser oscillations, and make Pr^{3+} doped fluoride fibre an interesting host for this type of application. As shown in the previous section, concentration quenching appears with a relatively low amount of dopant in the fibre, so Pr^{3+} amplifiers tend to have quite a

long cavity, moreover the possible absorption transition is located at around 1 μm where pump diode lasers have generally low power and is a relatively weak transition.

Pr^{3+} is notorious for the inconsistency between the radiative transition probabilities obtained by use of Judd-Ofelt theory and the experimental values. The fluorescence in the measured lifetimes of transitions from levels $^1G_4$, $^1D_2$ and the $^3P_0$, $^3P_1$, $^1I_6$ multiplet, are different from those calculated due to the two additional possible relaxation channels: multiphonons relaxation and cross-relaxation between pairs of ions.

The $^3P_0$, $^3P_1$, $^1I_6$ system is subject to energy migration due to the thermalisation and is characterised by the lifetime of the $^3P_0$ which is the longest lived state (50 μs) [28].

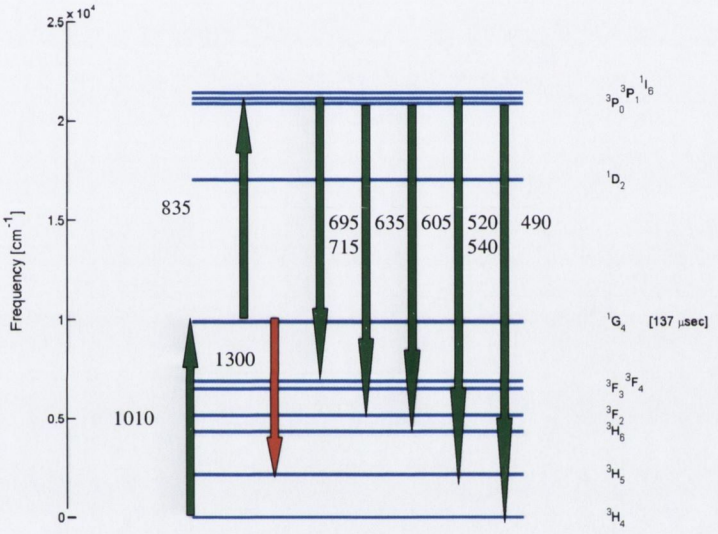

Figure 2.6: Energy levels of Pr^{3+} in fluoride fibre, the upconversion-pumping process and the most important visible laser transitions are shown. All the wavelengths are expressed in nm.

2.10 Introduction to Fibre Lasers and Amplifiers

The basic idea underpinning an optical fibre laser and an amplifier is relatively simple. A diode laser provides the optical power in order to excite the rare-earth ions, the cavity is usually made by two mirrors coated in order to obtain high reflection at the lasing wavelength, which confines the light and provides the optical feedback necessary in order to achieve oscillations. The mirrors are usually transparent at the pump

wavelength, which is filtered out after the mirror output coupler, the layout is shown in figure 2.7 A. Other solutions that have been implemented are based on fibre Bragg - gratings [29] and fibre loops [30], instead of mirrors.

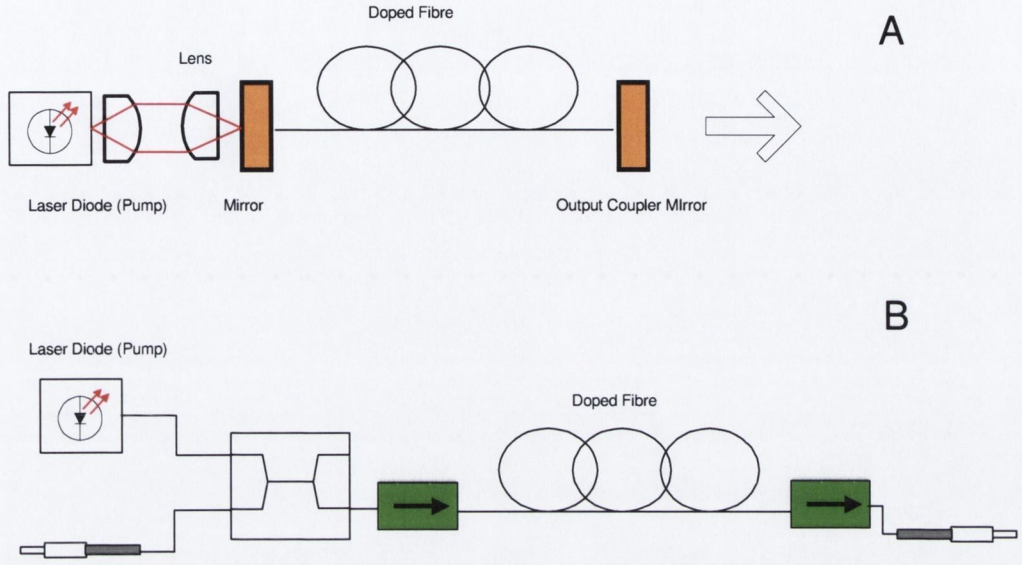

Figure 2.7: Upper, diagram A shows a Fabry-Perot fibre laser while diagram B is a fibre amplifier.

In a rare-earth doped fibre amplifier the mirrors are removed, and the pump is needed to establish population inversion in the fibre active medium. The dopant usually emits fluorescence at wavelengths which are located in the telecommunication band between 1.3 μm up to 1.6 μm; an incoming signal can be amplified by stimulated emission within the amplification bandwidth. This guarantees the coherence of the photons emitted with the signal. Usually, isolators are placed at the end of the active fibre, reducing the impact of back reflection. Low loss-connectors (FC type) are anchored on the front end in order to allow connection with optical cables for the input and the output of the signal (fig. 2.7 B).

The gain in the amplifier is defined as [31]:

$$G = \frac{P_{out} - P_{ase}}{P_{in}}, \tag{2.17}$$

where P_{in} and P_{out} are the amplifier input and output signal power and P_{ase} is the noise power generated by the amplifier, which lies within the optical bandwidth of the measurements. In most cases, P_{ase} is very low compared to the signal and can be neglected, moreover it is common practice to define the gain in dB as:

(2.18) $$G_{dB} = 10\log\left(\frac{P_{out}}{P_{in}}\right).$$

Predicting the gain is complicated by the local changes in power and signal that can affect the population of the excited states. At any given point in the fibre, it is possible to define the so-called gain coefficient as:

(2.19) $$g(z) = \sigma_{se} N_u - \sigma_a N_l ,$$

where the σ_{se} is the stimulated emission cross–section and σ_a is the absorption cross – section experienced by the amplifying signal whilst the N_u and N_1 are respectively the density of ions in the upper and lower levels involved in a transition.

The net gain G can be integrated if the explicit relation of the density with the fibre length is known, as:

(2.20) $$G = e^{\int_0^l g(z)dz},$$

or:

(2.21) $$G_{dB} = 4.3\int_0^l g(z)dz .$$

2.11 Analytical Model

The behaviour of rare earth ions in doped fibre lasers and amplifiers can be modelled by a phenomenological model which takes into account measured parameters of the transitions involved as: cross-sections and decay rates. The time dependent population densities of the excited state are subject to a set of differential equations called *rate-equations*. If the dynamics of the system are not under investigation it is usually possible to calculate directly the steady state value of the population densities without having to integrate a time dependent system of first order differential equations. It is clear that when the system is in the steady state, the rate of change of the population is zero and the *rate-equations* are reduced to a linear equations system. Moreover the system has to include the conservation law:

(2.22) $$N_{tot} = \sum_i N_i ,$$

where N_i are the population densities of each i-excited level and N_{tot} is the total doping density.

The dopant is usually expressed in percentage by weight, this is simply the mass of the dopant added during the preparation of the preform divided by the total mass of the glass and multiplied by 100. Similarly in ppmw (part per million by weight) is the previous fraction multiplied by 10^6:

$$c(ppmw) = \frac{m_d}{m_{ZBLA}} 10^6 . \tag{2.23}$$

One mole of ZBLA weighs (sum of all product of the molar fraction and molecular weight of the fluorides components or *W*) 167.8 gr. so 0.335 gr. of dopant in ZBLA is needed for 2000 p.p.m.-w doped fibre. If the density of the glass δ is known, the density of ions can found for thulium (PM_d=69) as:

$$N_{tot} = 10^{-6} N_a \frac{c(ppm-w)\delta}{PM_d} \approx 3.75\times10^{16} c \left[\frac{ions}{cm^3}\right].$$

In the literature the density is reported to be 4.3 gr/cm^3 [32]. If *c* is express in p.p.m-mol the density of ions is:

$$N_{tot} = 10^{-6} N_a \frac{c(ppm-mol)\delta}{W} \approx 1.64\times10^{16} c \left[\frac{ions}{cm^3}\right]. \tag{2.24}$$

Optical quantities such as pump power usually depend on the position along the fibre and they follow a first order differential propagation equation. Since these quantities appear in both the equations systems, in which they are coupled, a simple analytical solution is rarely possible and numerical methods must therefore be applied.

The full rate-equation numerical description is postponed until chapter 4, whilst here a simplified analytical solution will be given. An approximated analytical solution is essential in order to obtain a numerical solution. Indeed, the numerical integration method relies on a set of *guess solutions,* which will be iteratively relaxed until a converged solution is found.

In this section, the system formed by the four lowest levels of thulium ions will be analysed. This is the building block for the more complex models presented in the rest of the thesis. The energy levels are shown in fig. 2.8. It is possible to ignore *ab initio* the population of the $^3H_5$ level, this has a small impact in the calculation of the population densities, the error of the order of the decay branching ratio (1 %) for the 2.3 μm $^3H_4 \rightarrow {}^3H_5$ transition, moreover the energy gap with the lower lying energy level $^3F_4$

is comparable to the phonon energy of the zirconium glass. This creates a fast depletion by non-radiative relaxation and in the steady state, a population of zero is quite suitable.

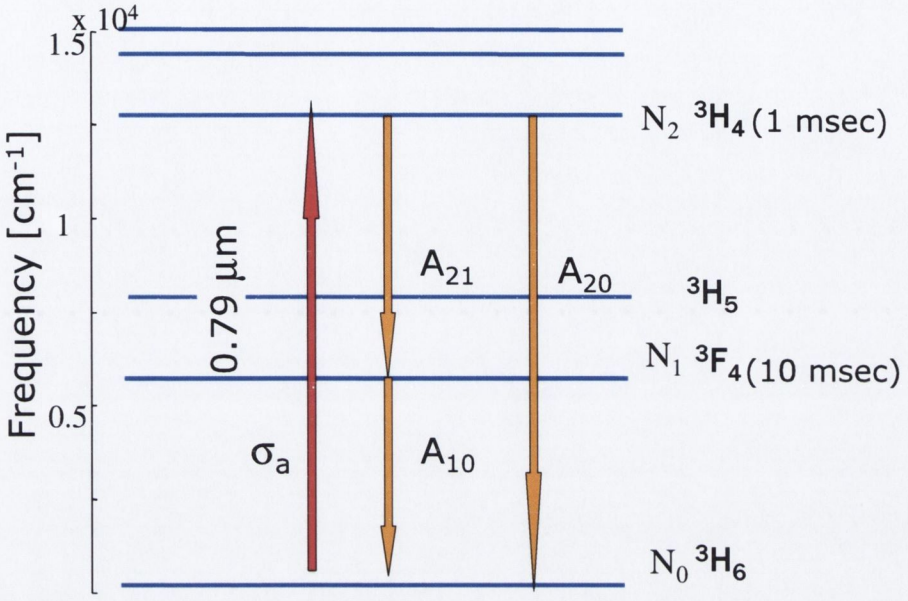

Figure 2.8: Lower energy Thulium levels used in order to give and approximated analytical solution.

The density populations N_i of the levels are filled according to the following set of first order differential equations:

$$\frac{dN_0}{dt} = -\sigma_a N_0 \Phi + A_{20} N_2 + A_{10} N_1,$$
$$\frac{dN_1}{dt} = A_{21} N_2 - A_{10} N_1,$$
$$\frac{dN_2}{dt} = \sigma_a N_0 \Phi - A_{20} N_2 - A_{21} N_2,$$
$$N_{Tot} = \sum_{i=1}^{5} N_i$$

where σ_a is the absorption cross-section for the $^3H_6 \rightarrow {}^3H_4$ transition, and Φ i s the flux pump rate, i.e. number of photons per unit of time and area and the A_{ij} are the transition rates from the level *i* to the level *j*.

Steady state conditions require that the time derivative is zero. It is useful to define two constants in such a fashion that they have the property of being unit-less for the first and for the second, a rate per unit area, which gives the followed equations:

(2.25) $$\beta = \frac{A_{21}}{A_{10}}; \gamma = \frac{1}{\sigma\tau}.$$

From the rate equations it is possible to derive the density of the ground state population as a function of the pump flux within the fibre:

(2.26) $$N_0 = \frac{\gamma N_{Tot}}{\gamma + \Phi(\beta+1)} = \frac{N_{Tot}}{1+\frac{\Phi}{\Phi_{sat}}},$$

where

$$\Phi_{sat} = \frac{\gamma}{\beta+1},$$

is defined as the saturated pump flux, once the pump flux is equal to the saturated flux pump then the ground state population is reduced to half its total value.

The propagation equation of the pump in terms of the rate of photon per unit of second and the fibre mode area can be written as:

(2.27) $$\frac{d\Phi}{dz} = -\sigma_a N_0 \Phi = -\frac{\sigma_a N_{Tot}\Phi}{1+\frac{\Phi}{\Phi_{sat}}}.$$

The previous equation can be analytically integrated up to a fibre length `l` as:

(2.28) $$\ln\frac{\Phi(z)}{\Phi(0)} + \frac{(\Phi(z)-\Phi(0))}{\Phi_{sat}} = -\sigma_a N_{Tot} l.$$

Equation 2.28 does not have a solution that can be written in closed form, however some information can be extracted, the equation can be recast in the following form:

(2.29) $$\ln(a) + a = \ln(b) + b - \sigma_a N_{Tot} l,$$

where $a = \Phi(0)/\Phi_{sat}$ and $b = \Phi(L)/\Phi_{sat}$, if both a and b are smaller than unity (no saturation) then they are negligible in respect to the logarithm and so it is reduces to:

(2.30) $$\Phi(l) \approx \Phi(0)\mathrm{e}^{-\sigma_a N_{Tot} l}.$$

When $a>>1$ then the logarithm can be neglected and the output flux is linearly proportional with the length of the fibre whereupon:

(2.31) $$\Phi(l) \approx \Phi(0) - \Phi_{sat}\sigma_a N_{Tot} l = \Phi(0) - \frac{N_{Tot} l}{\tau(\beta+1)}.$$

Usually 2.30 is taken as the definition of the absorption length. Converting the flux in power means specifying a particular fibre, mode area and laser wavelength, therefore, power, intensity and flux are related by the following equations:

$$\Phi = \frac{I}{h\upsilon} = \frac{P}{A_{eff} h\upsilon},$$

where $h\upsilon$ is the energy of the photons and A_{eff} is the effective mode area.

In other words the absorption length L is the fibre length that reduce the launched power by a factor $1/e$, i.e.:

(2.32) $$P(L) = P(0)e^{-\sigma_a N_{Tot} L} = \frac{P(0)}{e},$$

so in the absence of bleaching of the ground state $L = \frac{1}{N_{Tot}\sigma_a}$.

From eq. 2.28, it is possible to define a generalised absorption length L' where the pump power is 1/e of its initial value as:

(2.33) $$-1 + \frac{\beta+1}{\gamma}\left(\frac{\Phi(0)}{e} - \Phi(0)\right) = -\frac{L'}{L},$$

this yields:

(2.34) $$L' = L\left[\frac{\lambda P(0)}{hcA_{eff}}\frac{\beta+1}{\gamma}\left(\frac{e-1}{e}\right)+1\right],$$

which describes the absorption length as the limit of the generalised absorption length when the power is low. Equation 2.34 does not represent the exact solution however, it provides a useful approximation for the absorbed power in the intermediate regime and can be used in a numerical calculation as a guess solution. It has the desirable property that it explicitly takes into account the dependence on the input power, and so can be easily implemented in computational programs. The effect of the bleaching of the ground state is shown in fig 2.9 where the fraction of the absorbed power is defined as:

(2.35) $$\varphi = \frac{P(0) - P(l)}{P(0)}.$$

For a generic z point in the fibre, the population of the upper level can be calculated as:

(2.36) $$N_2 = \frac{N_{Tot}\Phi}{\gamma + \Phi(\beta+1)} = \frac{N_{Tot}}{(\beta+1)}\frac{\Phi}{\Phi_{sat} + \Phi},$$

and for N_1:

(2.37) $$N_1 = \beta N_2 = \frac{\beta N_{Tot}}{(\beta+1)} \frac{\Phi}{\Phi_{sat}+\Phi}.$$

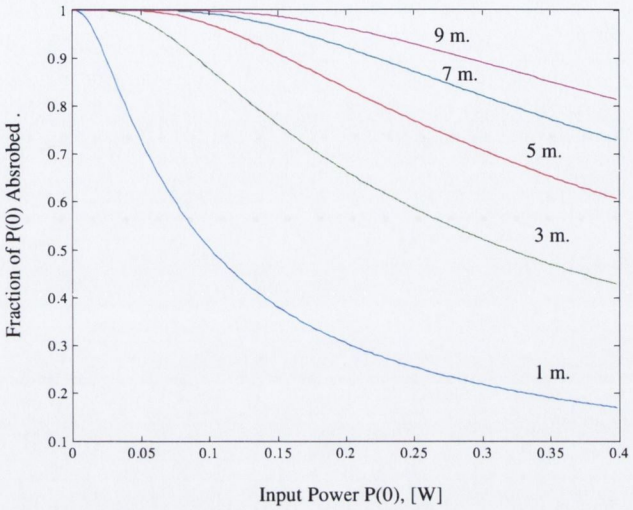

Figure 2.9: Predicted absorption for 800 nm pump in a 2000 p.p.m. thulium doped fibre, this shows how to take into account the approximated bleaching of the ground state with an analytical treatment.

The small gain coefficient for a 1.47 μm signal, if the negative contribution of the ESA is neglected, can be written as:

$$G_{dB}(\lambda) \approx 4.34\sigma_e \int_0^l N_2 dz = 4.34 \frac{\sigma_e N_{tot}}{(\beta+1)} \int_0^l \frac{\Phi}{\Phi_{sat}+\Phi} dz .$$

The previous equation cannot be integrated without knowing explicitly how the pump flux changes with the length, however at high pumping rate when $\Phi \gg \Phi_{sat}$:

(2.38) $$G_{dB} \approx \frac{\sigma_e N_{tot}}{(\beta+1)} l .$$

Equation 2.38 shows that the gain is limited by the factor β which is the ratio between the decay rate for the fluorescence at 1.47 μm and the one at 1.9 μm. Reasoning from the previous equation, increasing the decay rate A_{10} would lead to a higher gain coefficient. Therefore if laser oscillation between the $^3H_4$ level and the ground state can be established this will alter the value of β which will tend to the limit $\beta = 0$.

2.12 Determination of the Ground State Absorption Cross-Section in Thulium Doped Fibre

Usually, precise absorption measurements in fibre are obtained using white light cutback techniques [33]. A light from a high brightness incoherent source is launched into one end of the doped fibre and the spectral power of the unabsorbed light is then detected at the other end by a monochromator and a detector such as a photomultiplier for the visible wavelengths and a Germanium or InGaAs photodiode if we are measuring the IR. The fibre is then cut to a shorter length and the measurement repeated, the difference between the two measurements can be attributed to the amount of fibre removed.

This method is appropriate if the quantity of the fibre available allows cutting into shorter pieces, much of the time this is not possible. Another problem in fibre absorption measurement is that there are large spreads in the absorption cross-section of different absorption peaks, the fibre length should be enough to satisfy a reasonable absorption (usually 10 dB) for all the absorption peaks present in the range of the measurement.

For a given length l of fibre, the attenuation (in dB) is defined as:

$$A(\lambda) = 10\log\left(\frac{P_{in}(\lambda)}{P_{out}(\lambda)}\right), \tag{2.39}$$

where $P_{out}(\lambda)$ and $P_{in}(\lambda)$ are the power at the input end of the fibre and the power after the probe light has travelled along the fibre. Usually attenuation is reported in the literature as specific attenuation $\alpha(\lambda)$ where $A(\lambda)$ of equation 2.39 is normalised by the fibre length and the dopants concentration and expressed in $dB/(km\times ppm)$.
If a broad incoherent source is used, the power is very low and it is possible to assume that the number of ions excited is small. The output power in equation 2.39 can be found from equation 2.32, therefore, the absorption cross-section yields:

$$\sigma_a(\lambda) = \frac{4.3A(\lambda)}{\Gamma_{01}(\lambda)N_{tot}l}.$$

The confinement factor Γ_{01} takes into account the change in the fundamental mode size in the wavelength region where the fibre is single mode.

The absorption obtained is shown in figure 2.9, an arrow points to the Nd:YAG wavelength, information that is needed in order to develop a model for the dual pump amplifier (Chapter 6).

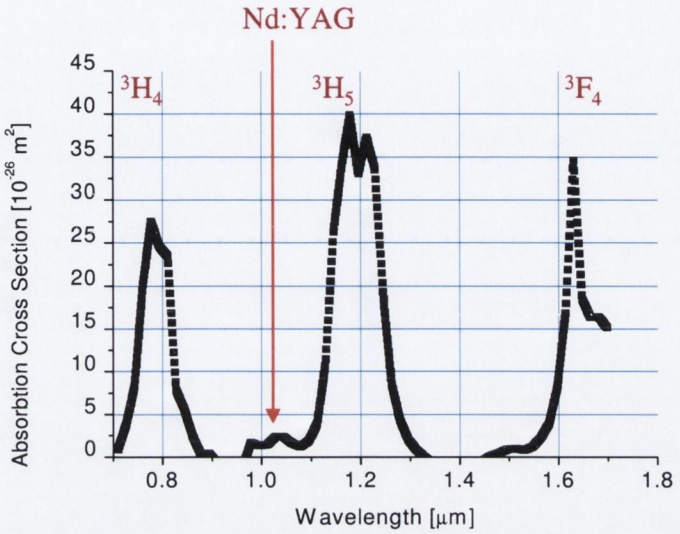

Figure 2.10:Measured absorption cross-section from a 2000 p.p.m. , 10 cm Thulium doped fluoride fibre above the cut-off wavelength.

2.13 Lifetime Measurements

Excited states of metastable levels in rare-earth ions have a finite lifetime ranging from milliseconds down to a few microseconds. In fluoride fibre with its low phonon energy, the lifetimes of most of the rare earth ions dopants are considerably longer than in silica fibres making it relatively easy to obtain accurate measurements.

A direct way of measuring lifetimes is simply by monitoring the decaying fluorescence from a short length of fibre by a square-wave modulated (or a pulsed) laser pump beam. The pump should be modulated at a frequency small enough to allow a build up of the excited state population. Since there is a small pump ESA centred around 780 nm the best operation is to tune the Ti-sapphire pump to wavelengths as high as possible in order to reduce the population of the higher level that can cause non-linear behaviour.

The pump has been selected within the longer wavelength part of the absorption cross-section.

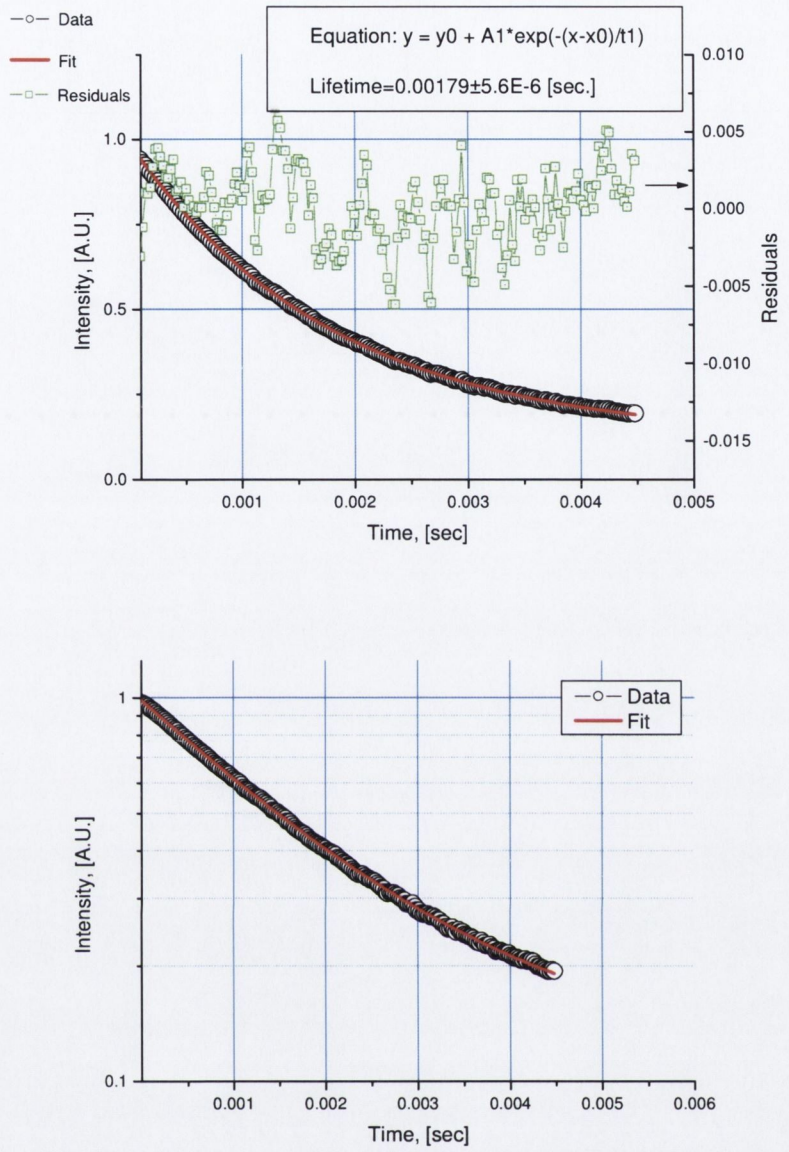

Figure 2.11: Exponential decay of the $^3H_4$ level for the 1.47 μm transition. The upper figure shows the decay fit and the calculated lifetime. The lower figure is the same decay on a log scale.

The time decay is shows in figure 2.11 and gives a lifetime of 1.79 ms which is comparable with the reported 1.55 ms value [34]. The same procedure has been used in order to calculate the lifetime of the $^1G_4$ level, which gives a value of 770 μs.

2.14 Determination of Stimulated Emission Cross-Section

With the lifetime of the $^3H_4 \rightarrow {}^3F_4$ thulium transition measured, it is possible to estimate the stimulated emission cross-section from the fluorescence at 1.47 μm by pumping the

fluoride fibre with an 790 nm Ti:Sapphire laser, the fluorescence can be detected with an optical spectrum analyser. A silicon filter is effective in cutting-off the remaining pump and the fluorescence at 790 nm. The effective line width can be calculated after eliminating any baseline as [12]:

$$\Delta\lambda = \frac{1}{I_{peak}} \int I(\lambda) d\lambda \tag{2.40}$$

where $I(\lambda)$ is the detected power per unit mode area and wavelength, therefore that gives:

$$g(\nu) = \frac{\lambda^2}{c} \frac{1}{\Delta\lambda} \tag{2.41}$$

For a continuous spectrum, the detected total power can be written as:

$$P = \sum_{i=1}^{N} P_i \frac{\Delta N}{R} \tag{2.42}$$

where P_i is the power detected per bandwidth in the optical spectrum analyser, ΔN is the trace point spacing and R is the resolution bandwidth. Therefore, the effective linewidth can be related to the raw data obtained from the optical spectrum analyser as:

$$\Delta\lambda = \frac{\Delta N \sum_{i=1}^{N} \frac{P_i}{R}}{\frac{P_{peak}}{R}} \tag{2.43}$$

The Fuchtbauer-Landenberg equation 2.13 then become:

$$\sigma_{21} = \frac{\lambda^4}{8\pi n^2 c \tau_2 \Delta\lambda},$$

giving the peak value for the stimulated emission cross-section. Figure 2.12 shows the lineshape scaled to the calculated stimulated emission cross-section in good agreement with the reported value [35].

When there is a laser pump source usually the best practice is to detect the fluorescence transversally to the fibre. This method has multiple benefits:

1) The pump is geometrically filtered so high detectivity devices such as photomultipliers can be employed without being affected by pump scattering.

2) The amount of light that can be gathered into the spectrometer can be selected in order to have the required signal to noise ratio and spectral resolution by selecting the appropriate lens.

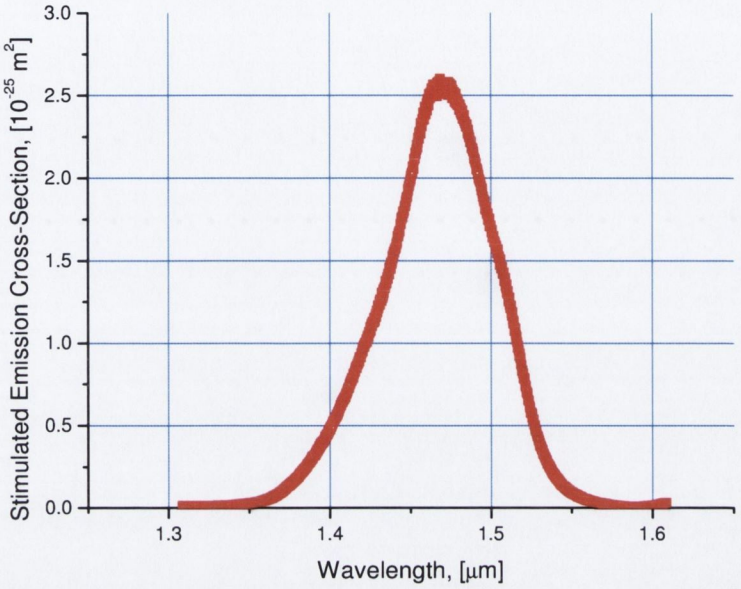

Figure 2.12: Stimulated emission cross-section determined from the measured spontaneous fluorescence spectrum

2.15 Determination of Thulium Excited State Absorption Cross-Sections.

Relevant information can be determined by measuring infrared-excited state absorption of thulium ions in fluoride glass fibre. A fundamental problem in the measurements of an excited state absorption spectrum and its intensity magnitude is the difficulty of building up a controlled population in the excited state. In order to obtain a good signal to noise ratio, a double modulation technique has been employed as shown in figure 2.13.

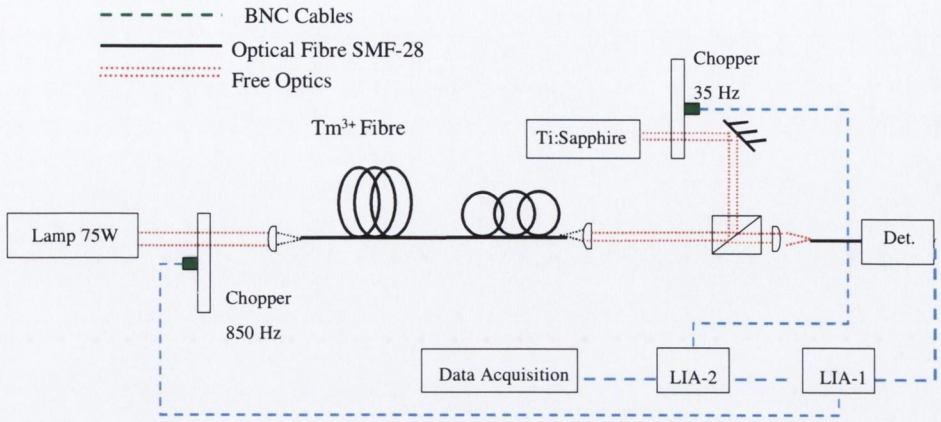

Figure 2.13: Sketch of the experimental system, which was used in order to measure the Thulium ESA between 0.9 μm and 1.6 μm. The time constants used for the two lock-in amplifiers (LIA) are respectively 5 ms for LIA-1 and 15 ms for LIA-2

The optical pump, a Ti-sapphire laser was chopped at 35 Hz, which is slow with respect to the lifetime of the $^3F_4$-transtion, in order to achieve steady state conditions. A broadband incoherent 75 W Xenon lamp modulated by a mechanical chopper at 850 Hz supplies the probe beam.

The length of the fibre must be enough to attenuate the probe light source by 10 dB in order to achieve a good dynamic range, the detector was a liquid nitrogen cooled pin germanium photodiode which allowed large sensitivity and a flat spectral response in the region between 0.7 μm up to 1.6 μm.

A conventional way to perform this type of measurement is to set the integration time constant of the first lock-in at least three times higher than half a cycle of the pump chopper [36]. Because the pump was modulated at 35 Hz, the pump half cycle is around 15 ms. Therefore the first lock-in amplifier (LIA) time constant could safely be selected at 5 ms with a probe frequency of 850 Hz. The transmitted probe intensity of the un-pumped sample is:

(2.44) $$I_{probe} = I_0 e^{-\sigma_{gsa} N_{tot} \Gamma_{01} l}$$

where I_0 is the intensity, N_{tot} is the dopant concentration, l is the length of the fibre and σ_{gsa} is the ground state absorption cross-section.

The change in the transmission of the probe by the effect of the pump can be written as:

$$I_{probe}' = I_0 e^{-\sigma_{gsa}(N_{tot}-N_e)\Gamma_{01}l} + I_0 e^{\sum_i N_i(\sigma_{se}{}^i - \sigma_{esa}{}^i)\Gamma_{01}l}, \tag{2.45}$$

N_e is the total number of the excited ions, taking the logarithm of equation 2.45 and 2.44 yields:

$$\ln\left(\frac{I_{probe}'}{I_{probe}}\right) = \ln\left(1 - \frac{I_{probe}' - I_{probe}}{I_{probe}}\right) \approx \frac{\Delta I_{probe}}{I_{probe}}, \tag{2.46}$$

explicitly this gives:

$$\frac{\Delta I_{probe}}{I_{probe}} = lA\Gamma_{01}(N_e\sigma_{gsa} + \sum_i N_i(\sigma_{se}{}^i - \sigma_{esa}{}^i)), \tag{2.47}$$

where A is the amplification of the lock-in amplifier. The first lock-in amplifier measures the transmitted light signal I_{probe} while the second lock-in amplifier measures the differential transmitted intensity through the sample in the pumped and un-pumped case ΔI_{probe}.

The $^3F_4 \rightarrow {}^1G_4$ transition dominated the ESA at 1 μm see fig. 2.14. While the absorption cross-section from the ground state is low as shown before, it is not possible to efficiently separate the two ESA transitions. The excited state absorption at 1 μm is due to the combined effect of two different excited state absorption transitions. Recently, De Sousa and co-workers separated the two ESA transitions by a pump modulation frequency resolved technique [36]. The ESA centred at 1.4 μm affects the amplification of the signal in an eventual amplifier.

Eq. 2.47 can be specialised for the ESA and GSA around 1 μm as:

$$\frac{\Delta I_{probe}}{I_{probe}} = lA\Gamma_{01}(N_e\sigma_{gsa} + N_1(\sigma_{se} - \sigma_{esa}{}^s) + N_2(\sigma_{se} - \sigma_{esa}{}^w)) \tag{2.48}$$

where $\sigma_{esa}{}^w$ is the weak ESA and $\sigma_{esa}{}^s$ is the strong ESA as shown in fig 2.14. Since it is not possible to separate the contribution of the two ESAs, it is convenient to focus only on the strong ESA, neglecting the contribution of the $\sigma_{esa}{}^w$ and σ_{gsa} in order to obtain the absolute value, moreover for a short fibre, the effect of the spontaneous

emission is low and if the pump power is lower than the saturation power $N_e\sigma_{gsa} \approx 0$, therefore:

$$\frac{\Delta I_{probe}}{I_{probe}} \approx lA\Gamma_{01}N_1\sigma_{esa}{}^{s} \tag{2.49}$$

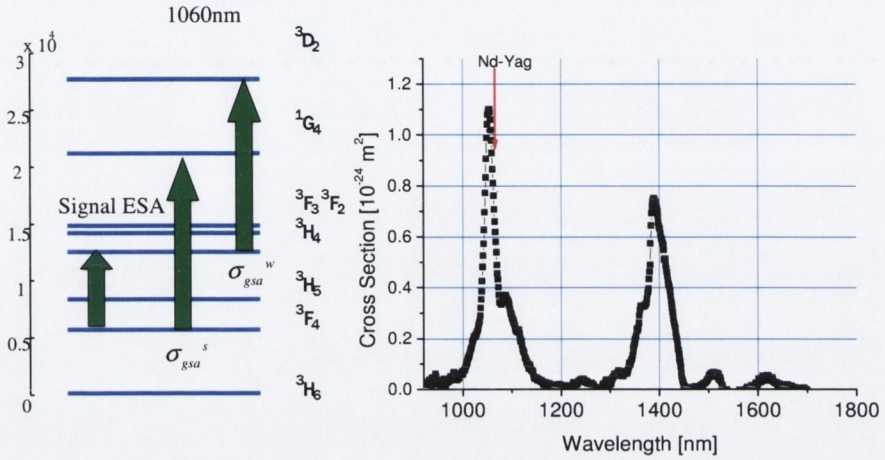

Figure 2.14: Experimentally measured Thulium ESA, the stronger absorption around 1.05 μm is due to the ESA $^3F_4 \rightarrow {}^1G_4$ transition. The peak is broadened by the second ESA $^3H_4 \rightarrow {}^3D_2$ and the ground state absorption. The ESA $^3F_4 \rightarrow {}^3H_4$ is anti-Stokes shifted from the emission cross-section and is quite negligible for signals above 1.45 μm.

For the 1.4 μm ESA, since there is no ground state absorption between 1.35 μm up to 1.5 μm then eq. 2.47 becomes:

$$\frac{\Delta I_{probe}}{I_{probe}} = lA\Gamma_{01}N_2(\sigma_{se} - \beta\sigma_{esa}) \tag{2.50}$$

where the relationship 2.37 between N_1 and N_2 has been used.
If the fibre is short and the pump is low compared to the saturation power, then equations 2.30 and 2.36 give:

$$\frac{\Delta I_{probe}}{I_{probe}} \approx lA\Gamma_{01}\frac{N_T}{\beta+1}\frac{\Phi(0)}{\Phi_{sat}}(\sigma_{se} - \beta\sigma_{esa}) \tag{2.51}$$

and as the cross-section of the spontaneous emission have already been obtained, the excited state absorption can be calculated. The spectral and absolutes values of the excited state absorption cross-section are reported in fig 2.14.

2.16 Conclusions

This chapter reported the description of the behaviour of rare-earth ions, which is relevant in the understanding of their employment in optical devices. Some aspects, due to the complexity of the subject, have been treated from a purely phenomenological point of view. Properties of the fluoride fibres have been discussed outlining the advantages and the disadvantages with respect to silica fibres.

Modelling the rare-earth behaviour in doped fibre lasers or amplifiers starts from a set of rate equations and they have an analytical solution only in asymptotic limits. The case when the pump power is much bigger then the saturation power has been analysed and an approximate expression for the pump absorption has been proposed. Such approximates solutions, will play a central role in the following chapters when a complete numerical model will be developed. They show that a thulium amplifier has limited gain even at high pump power, and the possibility of enhancing the gain is by increasing the 1.9 μm emission decay rate. This will be the strategy pursued in chapters 4 and 5 where a prototype of a thulium amplifier working with a co-operative 1.9 μm laser will be discussed.

The rest of the chapter has been allocated to presenting significant spectroscopic measurements for transitions that are relevant in the following parts of the thesis. IR absorption, emission and excited state absorption cross-sections for single doped thulium fibre have been obtained and the values are in reasonable agreement with those presented by other workers [37].

2.17 References

[1] P. Urquhart, "Review of rare earth doped fibre lasers and amplifiers," *Optoelectronics [see also IEE Proceedings-Optoelectronics], IEE Proceedings J*, vol. 135, pp. 385-407, 1988.

[2] S. A. Payne, L. L. Chase, L. K. Smith, W. L. Kway, and W. F. Krupke, "Infrared Cross-Section Measurements for Crystals doped with Er, Tm, Ho," *IEEE Journal of Quantum Electronics*, vol. 28, pp. 2619-2630, 1992.

[3] L. F. Johnson, "Optical Maser Characteristics of Rare-Earth Ions in Crystals," *J. Appl. Phys.*, vol. 34, pp. 897-907, 1963.

[4] A. J. Freeman and R. E. Watson, "Theoretical Investigation of Some Magnetic and Spectroscopic Properties of Rare-Earth Ions," *Phys. Rev.*, vol. 127, pp. 2016-2023, 1962.

[5] C. W. Nielson and G. F. Koster, *Spectroscopic coefficient for p^n,d^n and f^n configuration*. Cambridge: MIT Press, 1964.

[6] W. T. Carnall, *Handbook Phys. Chem. Rare Earth Vol.3*: North-Holland, 1978.

[7] B. R. Judd, "Optical absorption intensities of rare earth ions," *Phys. Rev.*, vol. 127, pp. 750-773, 1962.

[8] G. S. Ofelt, "Intensities of crystal spectra of rare-earth ions," *J. Chem. Phys.*, vol. 37, pp. 511-517, 1962.

[9] D. E. McCumber, "Theory of phonon terminated optical masers," *Phys. Rev.*, vol. 134, pp. A299–A306, 1964.

[10] J. N. Carter, R. G. Smart, D. C. Hanna, A. C. Tropper, S. F. Carter, and D. Szebesta, "Theoretical and Experimental Investigation of a resonantly pumped doped fluorozirconate fiber amplifier around 810 nm," *J. of Lightwave Tech.*, vol. 9, pp. 1548-1553, 1991.

[11] W. J. Miniscalco, "Optical and Electronic Properties of Rare Earth Ions in Glasses," in *Rare Earth Doped Fibre Laser and Amplifier*, M. J. Digonnet, Ed. New York: Marcell Dekker, Inc., 1993.

[12] W. L. Barnes, R. I. Laming, E. J. Tarbox, and P. R. Morkel, "Absorption and emission cross section of Er^{3+} doped silica fibers," *Quantum Electronics, IEEE Journal of*, vol. 27, pp. 1004-1010, 1991.

[13] D. L. Dexter, "A theory of sensitized luminescence in solid," *J. Chem. Phys.*, vol. 21, pp. 846-857, 1953.

[14] J. E. Townsend, W. L. Barnes, K. P. Jedrzejewski, and S. G. Grubb, "Yb^{3+} sensitised Er^{3+} doped silica optical fibre with ultrahigh transfer efficiency and gain," *Electronics Letters*, vol. 27, pp. 1958-1959, 1991.

[15] M. Inokuti and F. Hirayama, "Influence of Energy Transfer by the Exchange Mechanism on Donor Luminescence," *J. Chem. Phys*, vol. 43, pp. 1978-1988, 1965.

[16] Y. Nishida, M. Yamada, T. Kanamori, K. Kobayashi, J. Temmyo, S. Sudo, and Y. Ohishi, "Development of an efficient praseodymium-doped fiber amplifier," *Quantum Electronics, IEEE Journal of*, vol. 34, pp. 1332-1339, 1998.

[17] S. E. Stokowski, R. A. Saroyan, and M. J. Weber, "Nd doped laser glass spectroscopy and physical proprieties," *Lawrence Livermore National Laboratory*, vol. M-095 Rev2, 1981.

[18] E. Desurvire and J. R. Simpson, "Evaluation of $^4I_{15/2}$ and $^4I_{13/2}$ Stark-level energies in erbium-doped aluminosilicate glass fibers," *Optics Letters*, vol. 20, pp. 547-558, 1990.

[19] B. J. Ainslie, "A review of the fabrication and properties of erbium-doped fibers for optical amplifiers," *Lightwave Technology, Journal of*, vol. 9, pp. 220-227, 1991.

[20] P. W. France, S. F. Carter, M. W. Moore, and C. R. Day, "Progress un fluoride for optical communications," *Br. Telecom Technol. J.*, vol. 5, pp. 28-39, 1987.

[21] S. F. Carter, M. W. Moore, D. Szebesta, J. R. Williams, D. Ranson, and P. W. France, "Low loss fluoride fibre by reduced pressure casting," *Electronics Letters*, vol. 26, pp. 2115-2117, 1990.

[22] Y. Ohishi, S. Mitachi, and S. Takahashi, "Fabrication of fluoride glass single-mode fibers," *Lightwave Technology, Journal of*, vol. 2, pp. 593-596, 1984.

[23] D. Tran, G. Sigel, and B. Bendow, "Heavy metal fluoride glasses and fibers: A review," *Lightwave Technology, Journal of*, vol. 2, pp. 566-586, 1984.

[24] K. Fujiura, Y. Nishida, T. Kanamori, Y. Terunuma, K. Hoshino, K. Nakagawa, Y. Ohishi, and S. Sudo, "Reliability of rare-earth-doped fluoride fibers for optical fiber amplifier application," *Photonics Technology Letters, IEEE*, vol. 10, pp. 946-948, 1998.

[25] M. J. Digonnet, *Rare earth doped fibre lasers and amplifiers*: Marcel Dekker, 1993.

[26] J. Y. Allain, M. Monerie, and H. Poignant, "Tunable CW lasing around 610, 635, 695, 715, 885 and 910 nm in praseodymium-doped fluorozirconate fibre," *Electronics Letters*, vol. 27, pp. 189-191, 1991.

[27] R. D. T. Lauder, J. N. Carter, A. C. Tropper, D. C. Hanna, S. T. Davey, and D. Szebesta, "Room temperature infrared-pumped, visible, praseodymium doped fluorozirconate fibre laser," presented at Fibre and Solid State Lasers, IEE Colloquium on, 1992.

[28] T. J. Glynn, I. Laulicht, L. Lou, A. J. Silversmith, and W. M. Yen, "Trapping of optical excitation by two types of acceptors in $La_{0.72}Pr_{0.25}Nd_{0.03}F_3$," *Phys. Rev. B*, pp. 4852-4858, 1984.

[29] G. P. Lees, M. J. Cole, and T. P. Newson, "Narrow linewidth, Q-switched erbium doped fibre laser," *Electronics Letters*, vol. 32, pp. 1299-1300, 1996.

[30] G. J. Cowle, D. N. Payne, and D. Reid, "Single-frequency travelling-wave erbium-doped fibre loop laser," *Electronics Letters*, vol. 27, pp. 229-230, 1991.

[31] D. Derickson, *Fiber Optic Test and Measurement*. Upper Saddle River, New Jersey: Prentice-Hall, Inc., 1998.

[32] J. McDougall, D. B. Hollis, and M. J. P. Payne, "Spectroscopic properties of Er^{3+} in fluoride glass," *Phys. and Chem . of Glasses*, vol. 37, pp. 256-257, 1996.

[33] H. R. D. Sunak, "Single-mode fiber measurements," *Instrumentation and Measurement, IEEE Transactions on*, vol. 37, pp. 557-560, 1988.

[34] L. Esterowitz, R. Allen, and I. Aggarwal, "Pulsed laser emission at 2.3 μm in a thulium doped fluorizriconate fibre," *Electronics Letters*, vol. 24, 1988.

[35] T. Komukai, T. Yamamoto, T. Sugawa, and Y. Miyajima, "Upconversion pumped thulium-doped fluoride fiber amplifier and laser operating at 1.47 μm," *Quantum Electronics, IEEE Journal of*, vol. 31, pp. 1880-1889, 1995.

[36] D. F. de Sousa, V. Peters, G. Huber , A. Toncelli, D. Parisi, and M. Tonelli, "Pump modulation frequency resolved excited state absorption spectra in Tm^{3+} doped YLF," *Applied Physics B: Lasers and Optics*, vol. 77, pp. 817-822, 2003.

[37] T. Sakamoto, "Spectroscopy of thulium-doped halide glass," *Hewak, D.W. (Ed.), 'Properties, processing and applications of glass and rare earth-doped glasses for optical fibres', EMIS Datareviews Series, no. 22 (Inspec, IEE, Stevenage, UK, 1998), IEE Proc.-Optoelectron.*, vol. Vol. 151, pp. 236, 2004.

Chapter 3

Resonant transfer between Tm^{3+} and Pr^{3+} in ZBLA glass

3.1 Introduction

In the previous chapter, it was shown that Praseodymium (Pr^{3+}) in low phonon energy hosts such as zirconium fluoride based glass has very attractive characteristics for use as an amplifier around 1.32 μm [1] [2]. At 1.3 μm, silica transmission fibres have zero dispersion and historically these wavelengths were selected for optical data communication. High speed optical data communications were developed prior to the advent of the erbium doped amplifier and most of the fibre deployed today around the world are designed to work at wavelengths near 1.3 μm. An efficient amplifier that can work at around 1.3 μm would be useful to upgrade the existing network without the need of laying new optical cables. Several examples of Pr^{3+} doped amplifiers with gain ranging between 20 dB-30 dB have already been reported [3]. Silica glass fibre has relatively large phonon energy and IR transitions on the Pr^{3+} ion in doped fibre are quite inefficient due to the quenching of the lifetime of closely spacing levels by phonon assisted non-radiative transitions. Glasses with reduced phonon energy, such as fluorozirconate glass, must therefore be investigated. A low phonon energy host allows lower non-radiative decay rates, which means longer lifetimes for the metastable levels and better radiative efficiency. The most common fluoride glass for telecommunication devices is called *ZBLAN* after the acronym of the constituent ions (ZrF_4 –BaF_2 –LaF_3 – AlF_3 –NaF). It has a characteristic phonon energy that is half that of silica (500 cm^{-1} compared to 1100 cm^{-1}), making the 1.32 μm transition more efficient. ZBLAN is also the material of choice for many visible fibre lasers. In this work a slightly different fluoride glass will be used (ZBLA), however the same conclusion can be transferred to most of the fluoride hosts known.

Visible fibre lasers still maintain an important role in today laser applications. While semiconductor lasers are available at the most important visible wavelengths and they have considerable advantages over fibre lasers: cost, low power consumption, and small size making them the best candidates for electronic integrated applications such as DVD lasers. Fibre lasers are characterised by a high beam quality, astigmatism free, narrow

linewidth and higher power scaling. Praseodymium, thanks to its electronic configuration, has several fluorescence emission across the visible and Pr^{3+} doped fluoride lasers have demonstrated low oscillation threshold for most of these transitions [4]. Generally what limits the use of Pr^{3+} ions (almost independently of the hosts composition) either in a laser or in an amplifier is the low absorption for direct pumping at 1.02 μm ($^3H_4 \rightarrow {}^1G_4$) in the near infrared. Moreover diode pump lasers (as InGaAs) have low output power (usually about 50 mW at these wavelengths) while solid-state lasers or the Nd-fibre lasers that can also be employed make the Pr^{3+} amplifiers and lasers less compact.

As observed in section 2.5, the doping concentration is limited and so therefore is the obtainable absorption length. The Pr^{3+} :$^1G_4$ transition is quenched by non-radiative decay and concentration quenching appears at the 500 ppm doping level and results in a reduction of the lifetime of the level [5].

The possibility of using a codoped rare earth system, to partially overcome the low absorption and move the pump wavelengths to a region where high power diode lasers are employable is a very attractive solution. Some studies have been carried out on the Yb^{3+}: Pr^{3+} [6] and Er^{3+}: Pr^{3+} [7] coupled systems and these have shown high efficiency for energy transfer.

Thulium also appears to be a good candidate for use in a codoped fibre. Firstly, it is possible to use cheap diode lasers manufactured for erbium amplifiers around 790 nm at thulium's strong absorption band. Secondly, concentration quenching only appears at high doping levels and so high dopant concentrations can be used without appreciable detrimental effects on the optical properties.

Detecting resonant transfer is possible by the direct observation of Pr^{3+} fluorescence since Pr^{3+}-ZBLA singly doped fibre does not absorb directly at the selected wavelength (790 nm), and so the observation of Pr^{3+} fluorescence under 790 nm excitation would occur only by energy transfer by either radiative or non-radiative processes. It is sufficiently clear that Pr^{3+} ions can absorb the guided part of the thulium fluorescence, this process is particularly inefficient since only a relatively small part of the thulium fluorescence is guided and the Pr^{3+} absorption spectra do not fully overlap with the thulium emission, reducing the overall energy transfer achievable.

The aim of this chapter is to study the possibility of resonant transfer in a codoped Tm^{3+}/Pr^{3+} ZBLA fibre. It will be shown that the higher energy levels of the ions are involved in an energy migration from the donor (Tm^{3+}) to the acceptor (Pr^{3+}). Energy transfers dynamic will be characterized by lifetime measurements with its associated transfer rate.

3.2 Energy Levels

An initial analysis of the visible absorption bands and the energy levels of the two ions involved suggests the potential for resonant transfer between the Tm^{3+}:$^1G_4$ level and the Pr^{3+}:$^3P_1$-$^3P_0$ band as sketched in fig.3.1.

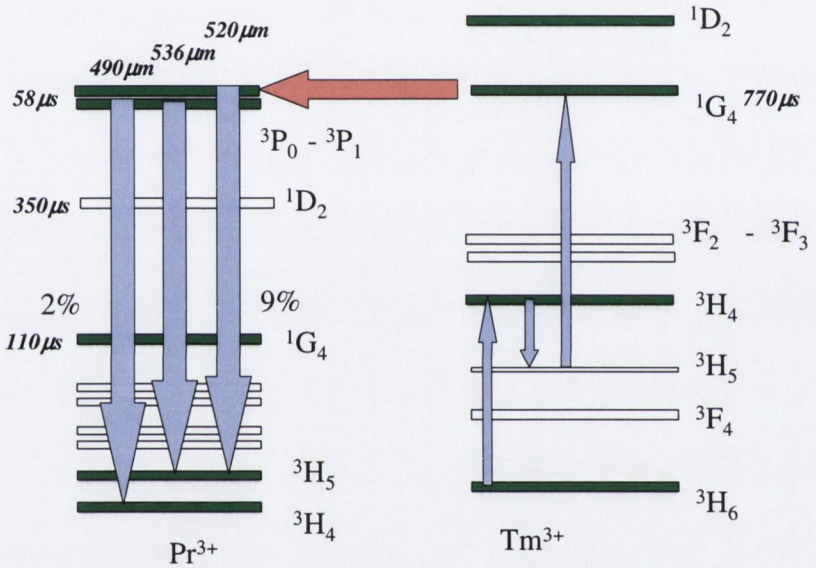

Figure 3.1: Energy levels of the two rare earth ions and the pumping scheme. Optical pumping at 790 nm from a Ti:Sapphire laser excites the Tm^{3+} ions to the higher energy levels through an ESA mechanism. The energy is transferred to the Pr^{3+} ions, where they have a metastable state at the same energy.

The overlap in absorption peaks of the ground state absorption is a good indicator for coupled levels. The Tm^{3+}:$^1G_4$ absorption band mainly overlaps the Pr^{3+}:$^3P_1$, but also partially overlaps the Pr^{3+}:$^3P_0$ absorption peak. It is expected that the net transfer is in favour of the transition from Tm^{3+}:$^1G_4$ to Pr^{3+}:$^3P_1$ and a minor back transfer probability from the Pr^{3+}:$^3P_0$ to Tm^{3+}:$^1G_4$. Energy transfer has been extensively studied by

Murdock and Cockroft in $YLiF_4$ [8] and in $CsCdBr_3$ at 10K [9]. In $CsCdBr_3$ the lifetimes of the $^1D_2$, $^3P_0$ $^3P_1$ are similar to those of ZBLA (150, 20, 50 μs) while for the thulium levels they are usually lower than that reported in low-phonon energy glasses. Thulium is well known to be consistent with regards to Judd-Ofelt analysis, therefore the effect of cross-relaxation between thulium ions at concentrations normally used in glasses (3000 ppm –2000 ppm) is very small. Thulium ions have a preference for clustering in crystals in order to minimise the lattice strength while in fluoride glasses clustering due to the random available presence of network modifiers is reduced.

The energy mismatch between the Tm^{3+}:$^1G_4$ and the multiplet $^3P_0$, $^3P_1$,$^1I_6$, is shown in table 3.1. The two levels $^3P_1$,$^1I_6$ have energy higher than Tm^{3+}:$^1G_4$ so the transfer requires a phonon in order to conserve energy. For the $^1I_6$ level, the mismatch is three times larger than the phonon energy so the energy transfer can be excluded.

The $^3P_0$ level is lower in energy therefore, in this case a phonon is released in order to guarantee energy conservation. A simple but effective way to prove the relative strength of the energy transfer between the Tm^{3+}:$^1G_4$ and Pr^{3+}:$^3P_0$ manifolds and the concurrent transfer Tm^{3+}:$^1G_4$ and Pr^{3+}:$^3P_0$ manifolds is to imagine that the levels are in thermal equilibrium.

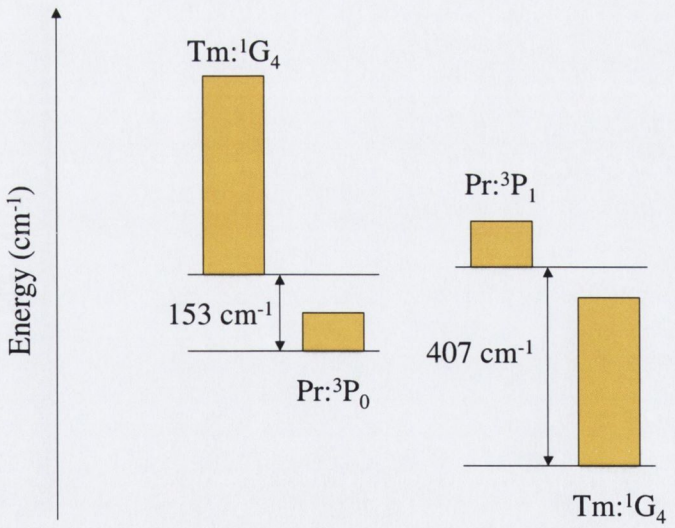

Figure 3.2: Schematic of the energy difference between the two levels involved in the energy transfer.

With regards to figure 3.2, the population ratio between Tm^{3+}:$^1G_4$ and Pr^{3+}:$^3P_0$ can be written as:

$$\frac{N_{tm}}{N_{pr}^0} = \frac{C_{tm}}{C_{pr}} \frac{2J_{tm}+1}{2J_{pr}+1} e^{-\frac{\Delta E}{k_b T}} = 2.51, \tag{3.1}$$

where C_{tm} and C_{pr} are the concentration of the thulium and praseodymium ions while J_{tm} and J_{pr} are the total angular momentum numbers for the two manifolds and the exponent is the ratio between the energy separation and the thermal energy at room temperature.

For the second case similarly:

$$\frac{N_{tm}}{N_{pr}^1} = \frac{C_{tm}}{C_{pr}} \frac{2J_{tm}+1}{2J^1{}_{pr}+1} e^{+\frac{\Delta E}{k_b T}} = 1.33. \tag{3.2}$$

This shows that the energy transfer to the $^3P_1$ praseodymium level is twice as favourable due to the larger degeneracy of the level with respect to the $^3P_0$. Reapplying the previous equation to the $^3P_1$ and $^3P_0$ manifolds for an isolated praseodymium ion only 20 % of the total ion population at the thermal equilibrium is in the $^3P_1$ level while the rest remain in the $^3P_0$ energy level. With these simple considerations it is possible to predict *a priori* that the possible back-transfer should be definitely weaker than the transfer in the forward sense. Similar resonant transfer was also obtained by Goh and co-workers in a Nd^{3+}-Pr^{3+}fluorozirconate glass [10]

Table 3.1: Energy mismatch between the Tm^{3+} energy level and Pr^{3+}multiplet.

Tm^{3+} [11]	Pr^{3+} [12]	Mismatch cm^{-1}
21053	$^1I_6$) 22734	1681
	$^3P_1$) 21460	407
	$^3P_0$) 20900	153

In order to study the resonant transfer, the pump wavelength was selected at 790 nm from a Ti: Sapphire laser, since Tm^{3+} has strong absorption in this region and excited state absorption (ESA) from $^3H_5$ to $^1G_4$ can be used to populate the Tm:$^1G_4$ level, giving blue upconversion fluorescence around 475 nm. We measured the lifetime of the Tm^{3+}:$^1G_4$ level to be 770 μs by pumping at 790 nm using a singly doped 3000 ppm ZBLA-Tm^{3+} fibre. This value is in agreement with the value calculated through the

Judd-Ofelt analysis described in [13] and it is clear that cross-relaxation between thulium ions is low. Due to the large energy gap of 7000 cm^{-1} to the next lowest levels $^3F_3$ and $^3F_2$, transitions from the Tm^{3+}:$^1G_4$ level are completely radiative in a low phonon energy glass.

Since in the codoped fibre the thulium ions are 6 times more concentrated, most of the Pr^{3+} ions will be located in heterogeneous Pr^{3+}-Tm^{3+} pair centres, while more than 80% of the thulium atoms will be in homogenous Tm^{3+}-Tm^{3+} centres and only a marginal amount will be in homogeneous Pr^{3+}-Pr^{3+} centres, so the Pr^{3+} fluorescence will be dominated from centres coordinated with Tm^{3+} ions. The Pr^{3+}:$^3P_{0\text{-}1}$ band has a lifetime around 50 μs in singly doped ZBLA fibre. Coupled resonant transfer with a longer lifetime level is interesting for a codoped system, since the resonant feeding process is controlled by the long lifetime of the donor and the total lifetime of the two coupled level will be the longer one.

The resonant transfer between the two ions has a characteristic dependence on the separation d of the interacting ions, according to Dexter's theory [14]: $W = \beta / d^n$, where W is the transfer rate and β is a parameter which includes all the physical details of the interaction. For a rather dilute sample such as ours, $n=6$ and the interaction is mainly governed by electric or magnetic dipole-dipole interactions, which dominate at large ion separation. The fluorescence intensity $I(t)$ at time t after pulsed excitation can be written in the form of an exponential decay:

$$I = I(0)e^{-\gamma t}, \tag{3.3}$$

where γ is the intrinsic decay rate, which is the sum of the transitions probability involved:

$$\gamma_k = \sum_n A_{kn} + R + W. \tag{3.4}$$

The A_{kn} is the decay probability for the level k for all the possible radiative transitions involved, R is the non-radiative probability for multiphonon decay and W is the resonant transfer rate from the donor to the acceptor. Eq.3.4 shows that the presence of resonant transfer changes the observed lifetime of the donor level.

The observed lifetime is the inverse of the probability decay rate:

(3.5) $$\tau_k^{Obs} = \frac{1}{\gamma_k}.$$

The energy transfer rate can be estimated from the variation of the observed donor lifetime with and without the presence of the acceptor, using:

(3.6) $$W = \frac{1}{\tau_{donor-acceptor}^{Obs}} - \frac{1}{\tau_{donor}^{Obs}}.$$

It is possible to show that if the process is diffusion limited, the energy transfer rate is proportional to both the donor and the acceptor concentrations. A further increase in the donor concentration produces a faster migration of energy from the donor. In this limit, the energy transfer rate is linearly proportional to the acceptor concentration. It was also shown that for very fast diffusion, the decay of the donor fluorescence is purely exponential [15].

However, the observed donor Tm^{3+} fluorescence emission at 475 nm is overlapped and reabsorbed by the acceptor Pr^{3+} that emits in the same wavelength region and lifetime measurements in this region cannot be easily related to a single specific ion. Pr^{3+} emits at longer wavelengths (540 nm) without overlap with the Tm^{3+} emission and because we are dealing with a coupled system with a long donor lifetime and a short acceptor lifetime when singly doped, we expect that the acceptor lifetime is approximately the donor lifetime in the codoped case.

Since the acceptor decay mirrors the donor decay apart from extra processes exclusively present in the acceptor (e.g. excited state absorption), we can show direct evidence of energy transfer by measuring the lifetime of the fluorescence at 540 nm, showing the large difference between the lifetimes of single and codoped cases. This should also be the lifetime of the donor level, except at high pump intensities where non-linear effects such as cross-relaxation between in-homogenous ion centres will further increase the decay rate.

3.3 Lifetime Measurements in the Co-doped Fibre

A preform of ZBLA fluoride doped with Pr^{3+} and Tm^{3+} was made in cubic form with a central cylindrical core diameter of 5 mm and a length of 15 mm. The core was doped with Tm^{3+} at 3000 ppm and Pr^{3+} at 500 ppm, a picture of the preform is presented in fig. 3.3. The fibre was drawn from the preform with a core of 6 μm and a standard single-

mode telecom-cladding diameter of 125 μm. The numerical aperture was 0.15 with the cut-off wavelength at 1.15 μm.

The visible fluorescence emission from the preform and the fibre were recorded with a half-metre spectrometer equipped with a photomultiplier (Hamamatzu 1P-28), which was blind at the pump wavelength. The lifetime measurements were performed by pulsing the CW Ti:Sapphire laser with an acousto-optic modulator. The signal from the PMT was digitised and recorded by a fast digital oscilloscope.

The main experimental difference between the preform and the fibre was related to the pump coupling. In the preform, a convergent long focal length lens (focal length 20 cm) was used to reduce the laser pump spot size and to achieve the high power density necessary for Tm^{3+} upconversion. For the fibre, the pump was coupled through a x20 microscope objective into the fibre end and fluorescence extracted from the other fibre end with a butt-coupled single-mode pigtail. The pump power, in the case of the preform was 150 mW for a spot size of 300 μm, giving an intensity of 200 W/cm^2. This value is two orders of magnitude less than that used in the fibre where the pump power was limited to 20 mW to avoid fibre-end damage. For this reason, the ESA in Tm^{3+} was less efficient in the preform than in the fibre, giving a lower population of the Tm:$^1G_4$ level. Other excited state absorption transitions in Pr^{3+} are negligible in the preform due to the low pump intensity.

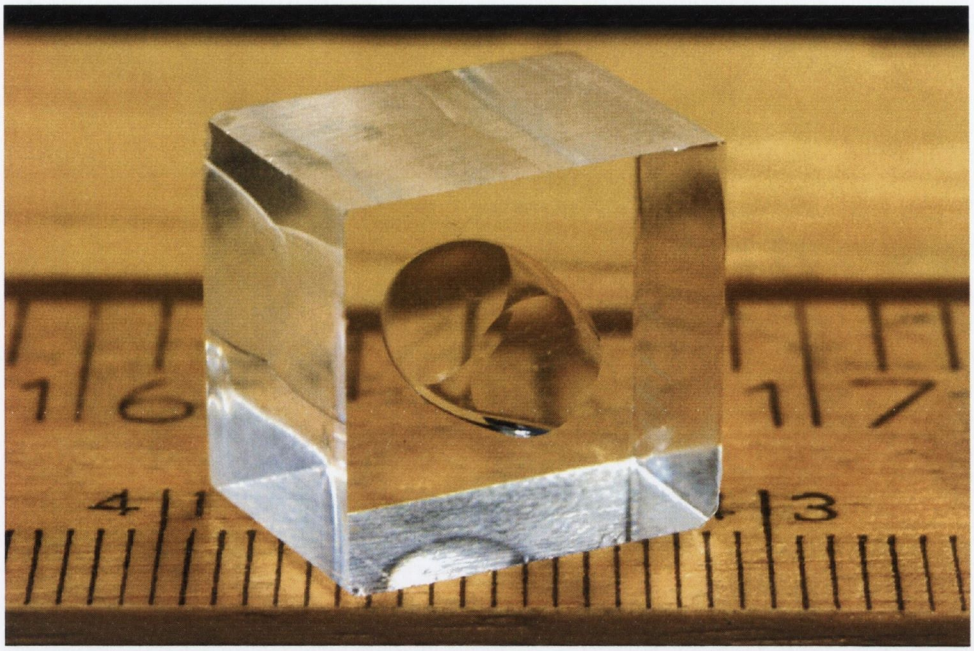

Figure 3.3: Picture of the co-doped Pr^{3+} Tm^{3+}preform used in order to analyse the resonant transfers between the two rare-earth ions.

3.4 Preform Results

Pr^{3+} does not absorb at 790 nm and all fluorescence related to the praseodymium is due to non-radiative transfer between the two ions, since in the preform the contribution of fluorescence re-absorption of the two ions is negligible. The spectral range around 540 nm is free of Tm^{3+} fluorescence and the light detected at 540 nm is direct evidence that we are populating the $^3P_{0\text{-}1}$ band of the Pr^{3+}, as shown in fig. 3.4

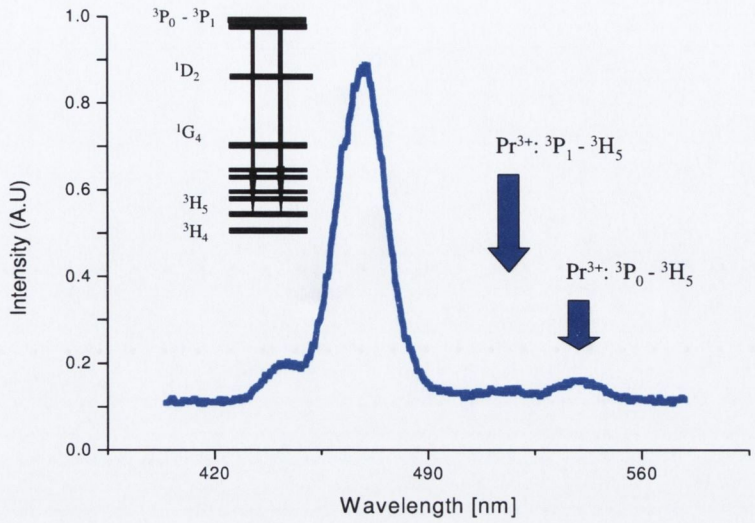

Figure 3.4: Visible fluorescence recorded for the ZBLA Pr^{3+}-Tm^{3+} preform, the band centred at 480 nm is mainly Tm^{3+} blue emission, and the fluorescence centred at 540 nm is pure Pr^{3+} emission from the $^3P_{0\text{-}1}$ band.

The dynamics of the transfer were also confirmed by the lifetime measurement of the 540 nm fluorescence. As shown in fig. 3.5, from the linear fit of the natural logarithm of the intensity we can extract the total decay rate, the lifetime is then 621 μs. This is shorter but comparable to the value of the lifetime of the Tm^{3+} donor (770 μs) which proves that resonant coupling between the two ions is occurring.

We have confirmed our prediction of resonant transfer between the two ions and this is the first evidence of such transfer between Tm^{3+} and Pr^{3+} in heavy metal fluoride glasses. The decay fits quite well to a single exponential, since the pump intensity is not enough to make other non-linear effects in the decay significant.

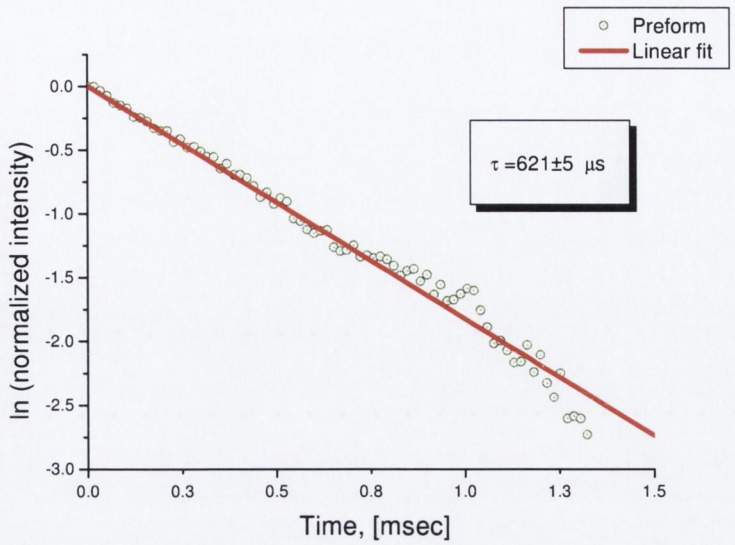

Figure 3.5: Plot of the natural logarithm of the fluorescence decay of the $^3P_0$ of Pr^{3+} in the preform at 540 nm. The points are the experimental data and the solid curve is the best fit to a single exponential decay.

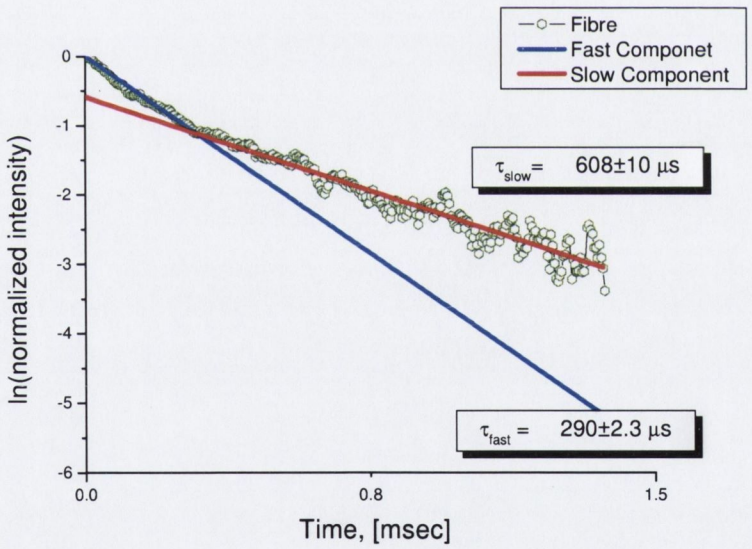

Figure 3.6: Estimation of two decay rates involved in the fluorescence decay of the $^3P_0$ of Pr^{3+} in the fibre at 540 nm. The points are the experimental data and the solid curve is the best fit. The fast component is attributed to the excited state absorption in Pr^{3+} and Pr^{3+}/Tm^{3+} cross-relaxation

3.5 Fibre Results

In the case of the fibre, the visible emission under pumping at 790 nm shows much the same behaviour as seen in the preform. However the light confinement allowed higher intensity. The blue band at 480 nm appears broader than in the preform. In fig 3.7 the blue fluorescence from a Tm^{3+} 3000 ppm 50 cm thulium fibre relative to the Tm^{3+}/Pr^{3+} 3000 ppm/500 ppm 50 cm co-doped fibre with 20 mW pump power is shown.

Lifetime measurements have been performed, in the same way as described for the preform. The selected fluorescence was again the Pr^{3+} fluorescence at 540 nm.

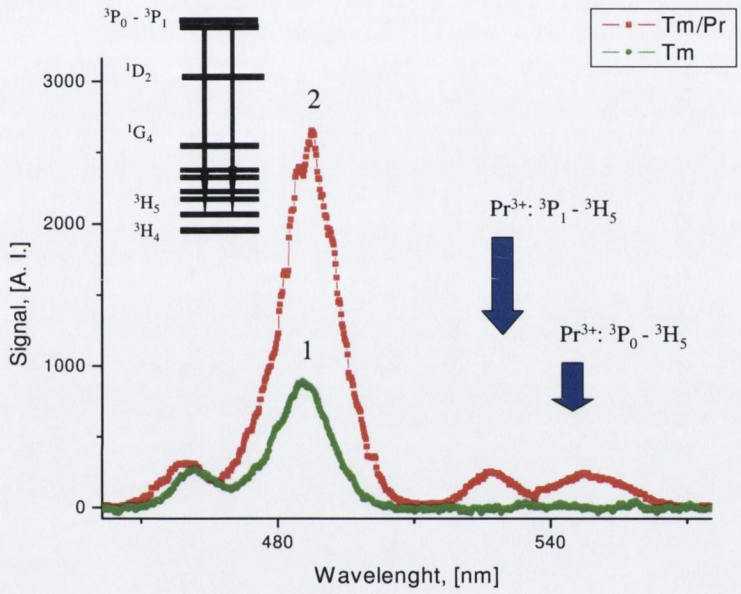

Figure 3.7: Visible fluorescence recorded for the ZBLA Pr^{3+}-Tm^{3+} fibre and ZBLA single doped fibre is shown for comparison detected under similar conditions, the band centred at 480 nm is mainly Tm^{3+} blue emission, and the fluorescence centred at 540 nm is purely Pr^{3+} emission from the $^3P_{0\text{-}1}$ band.

The decay recorded is not a pure exponential as in the case of the preform, however a fit with a double exponential decay gives a satisfactory result and an estimation of the lifetime of the two components involved, as shown in fig.3.6. The two components have lifetimes of 608 μs and 290 μs, the slow component can be related to the resonant transfer process observed in the preform. However due to the presence of an ESA-induced transition by the pump in the Pr^{3+} atoms we are, by contrast with the perform, in the presence of other mechanisms and so a deviation from an exponential decay is expected. The fast component is the due to ESA transitions on Pr^{3+} at the pump

wavelength. Quimby and Zhang [16] reported the determination of the ESA between $^1G_4$ and $^3P_0$ -$^3P_1$. the magnitude and the lineshape is reproduced is figure 3.8.

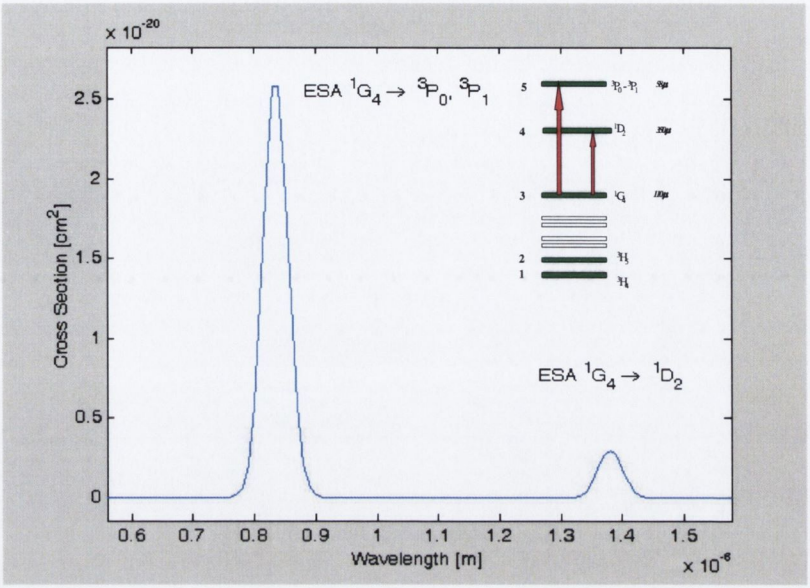

Figure 3.8: Measured cross-section of Pr^{3+} excited state absorption by Quimby and Zheng [16].

The tail in the observed lifetimes is then governed by the pure exponential decay of the Tm^{3+} level feeding the Pr^{3+} therefore we can get an indirect measurement of the lifetime of the Tm^{3+}: $^1G_4$ in the codoped system. The value of 608 μs agrees very well with the value of 621 μs determined from the preform.

Comparing the lifetime value measured for the single Tm^{3+} doped fibre we have a lifetime of 770 μs, while in the case of the codoped preform, the lifetime is reduced to 621 μs due to the presence of the resonant transfer to Pr^{3+}. The estimated rate according to equation (3.6) is then $W \approx 300\ s^{-1}$. We can use the value of 621 μs for the acceptor lifetime because the two levels are resonantly coupled and the transfer is mainly in the direction from Tm^{3+} to Pr^{3+} as previously explained.

Since the two lifetimes have been measured with the same technique and with a degree of confidence of 1 - 2 %, the total degree of confidence in the value of the transfer rate can be estimated to be around 4-5 %, this leads to an uncertainty of maximum $\pm 15\ s^{-1}$ in the value of the estimated W.

In the previous chapter we developed a semi-analytical model, which allows the description of the populations of the three lower levels of thulium ions under 790 nm pumping. A difficulty in modelling the higher Tm^{3+} excited state is that the Tm^{3+}-excited state absorption cross-section at 780 nm is unknown. However some more consideration can be done comparing the relative strength of the blue emission line from the Tm^{3+} doped and Tm^{3+}-Pr^{3+} co-doped fibre shown in figure 3.7.

The time derivative of the ion density of Tm^{3+}:$^1G_4$ (N_{tm}) and Pr^{3+}:$^3P_0$ (N_{pr}) energy levels can be written as two first order differential equations:

$$\begin{aligned} \frac{d}{dt}N_{tm} &= \omega - \left(W + \frac{1}{\tau_{tm}}\right)N_{tm} \\ \frac{d}{dt}N_{pr} &= +WN_{tm} - \left(\frac{1}{\tau_{pr}}\right)N_{pr} \end{aligned} \tag{3.7}$$

where ω is the pumping rate. At the steady state, the two right end side of the previous equations should be equal to zero and then it is possible to express the fraction of Pr^{3+}:$^1P_0$ multiplet compared to the Tm^{3+}:$^1G_4$ as:

$$\begin{aligned} N_{tm} &= \frac{\omega\tau_{tm}}{W\tau_{tm}+1} \\ N_{pr} &= \frac{W\omega\tau_{tm}\tau_{pr}}{W\tau_{tm}+1} \end{aligned} \tag{3.8}$$

The steady state population of the single-doped thulium can be obtained by putting $W=0$ in the first equation of 3.8. If we neglect re-absorption, the value of the integrated visible fluorescence can be express as:

$$P_{fluo} = N\,VA_j 2h\upsilon_j \Delta\Omega\,, \tag{3.9}$$

where the factor 2 is due to the fibre supporting two polarization states [17] and $h\upsilon_j$ is the energy of the photon. V is the modal volume and A_j is the decay probability for the j transition while $\Delta\Omega$ is the fraction of the fluorescence guided as described in the chapter 2, equation 2.16. So the ratio between the power of the fluorescence in the single thulium doped fibre and the total fluorescence power of the codoped fibre yields:

$$\frac{P_{tm}}{P_{tm}+P_{pr}} = \frac{W\tau_{tm}+1}{W\tau_{pr}\dfrac{A_{pr}^{480}}{A_{tm}^{480}}+1} = 0.86\,, \tag{3.10}$$

where the τ_{pr} and τ_{tm} are the lifetimes of the isolated thulium and praseodymium energy levels involved respectively of 50 μs and the measured 770 μs; W is the transfer rate estimated to be 300 $s.^{-1}$ and the two decay probability (A_{pr}^{480} and A_{tm}^{480}) for the transitions at around 480 nm have been taken from [11] and [12].

We can write the ratio of the power of the two fluorescence intensities shown in fig 3.7 as:

$$\frac{P_{tm}}{P_{tm}+P_{pr}} = \frac{I_1^{peak} FWHM_1}{I_2^{peak} FWHM_2} = 0.32, \tag{3.11}$$

where $I_{1,2}^{peak}$ are the intensities at the peak detected and $FWHM_{1,2}$ is the full width at half maximum (FWHM) respectively for the single doped Tm^{3+} fibre and the codoped Tm^{3+}/Pr^{3+} fibre. The difference between the value obtained in eq. 3.10 and eq. 3.11 further confirm that that there is a substantial contribution due to enhancing blue fluorescence at 480 nm from cross-relaxation between Tm^{3+}/Pr^{3+}pairs or Pr^{3+} pump induced excited state absorption.

3.6 Frequency Domain Technique

Frequency domain techniques can be useful in studying complex fluorescence decays and it has the capability of reducing the impact of a high pump noise level.

The technique consists of measuring the phase shift between the pump excitation and the produced fluorescence. Under a sinusoidal modulated excitation, the fluorescence is phase shifted due to the finite lifetime of the excited atom. For a linear system, as depicted in fig. 3.9, the output response *o (t)* is the result of the convolution between the input excitation *m(t)* and the impulse response of the system *h(t)* or:

$$o(t) = m(t) * h(t) = \int_{-\infty}^{\infty} m(t-t')h(t')dt'. \tag{3.12}$$

The input optical pump is modulated in a cosine fashion, its intensity assuming that it is normalised to unity is written as:

$$m(t) = \cos(\omega_0 t), \tag{3.13}$$

where ω_0 is the angular frequency.

For a single exponential decay eq.3.12 can be rewritten as:

(3.14) $$o(t) = \int_0^{\infty} \cos \omega_0 (t - t') e^{-at'} dt',$$

where the assumption is made that the excitation starts at $t=0$. The previous equation can easily be integrated and gives the well-known phase shift expression that depends on the modulation frequency ω_0 and the effective lifetime of the level involved τ:

(3.15) $$tan\theta = \omega_0 \tau \ ,$$

where $\theta = \theta_{pump} - \theta_{fluorescence}$ and it is positive since the fluorescence is retarded with respect to the pump. The tangent value of the phase shift is thus linearly proportional to the lifetime and independent of any intensity variation of the signal. This is justified when the fluorescence is emitted from a population of electrons which experience the same decay dynamic.

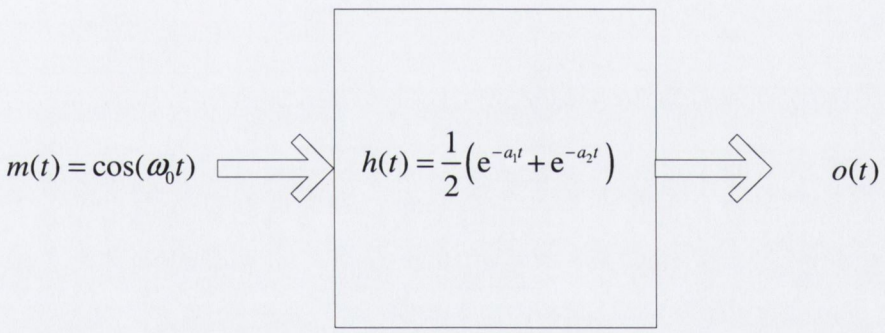

Figure 3.9: The *o(t)* is the time dependent output function which is the convolution between the input function *m(t)* and the system response function *h(t).*

It is possible however, to give a general theory treatment in the case where the response function of the system is not a pure exponential decay by the aid of the convolution theorem applied to eq. 3.14. The Fourier transform of the output function can be written as the product of the Fourier transform of the input modulation multiplied by the Fourier transform of the system response. The Fourier transform of the cosine modulation is two delta functions symmetrically located about the angular frequency $\omega_0 = 2\pi f$:

(3.16) $$M(\omega) = \pi\left(\delta(\omega-\omega_0)+\delta(\omega+\omega_0)\right),$$

while the Fourier transform of the two exponentials due to the linearity of the Fourier operator is:

(3.17) $$H(\omega) = \left(\frac{1}{a_1+i\omega}+\frac{1}{a_2+i\omega}\right)$$

If we multiply the two expressions of the two calculated Fourier transforms, it is possible to obtain the response function in the frequency domain by using Dirac delta distribution property $\delta(x-x_0)f(x) = \delta(x-x_0)f(x_0)$ as:

(3.18) $$O(\omega) = \pi\left(\delta(\omega-\omega_0)\left[\frac{1}{a_1+i\omega_0}+\frac{1}{a_2+i\omega_0}\right]+\delta(\omega+\omega_0)\left[\frac{1}{a_1-i\omega_0}+\frac{1}{a_2-i\omega_0}\right]\right).$$

Comparing with the Fourier transform of a phase shifted cosine function:

(3.19) $$F(\cos(\omega_0 t+\theta)) = \pi(e^{-i\theta}\delta(\omega-\omega_0)+e^{i\theta}\delta(\omega+\omega_0))$$

The phase shift of the output, which is due to the finite lifetime of the excited atoms, can be written with some easy but tedious calculations as:

(3.20) $$\tan\theta = \omega_0\frac{(a_1^2+\omega_0^2)+(a_2^2+\omega_0^2)}{a_2(a_1^2+\omega_0^2)+a_1(a_2^2+\omega_0^2)}$$

Eq. 3.20 correctly reduces to the case of single lifetime in eq. 3.15 when $a_1=a_2=\frac{1}{\tau}$.

Equation 3.20 is valid to the extent that the first decay has much grater intensity that the second decay, this is mostly true when the effect of the resonant transfer is small compared to the natural decay of the level. However in our case the difference between the two time constants is too close to be detected simultaneously. An RC circuit is presented in fig 6.11 (A) and can be used to describe the phase shift experience by a sinusoidal modulation when the system response is a exponential decay, the lifetime of the metastable level is represented by the product of resistance and capacitance.

The phase shift generated by the first path when R_a is equal to10 Ω, C_a is 20 μF is illustrated in fig 3.10, this is the phase shift of the decay component that is unknown and we set a value of 200 μs as measured in the time domain. Adding an extra RC with R_b=*10 kΩ*, C_a= *60 nF* should simulate the presence of a decay channel that hides the previous decay with a decay time of 600 μs. Since it is known from the time domain that the slow decay is of the order of 600 μs, a way to illustrate this problem is to

implement a circuit able to cut off the phase shift due to the slow decay, leaving the phase shift due to the fast decay to be detected.

A schematic diagram of the electronic circuit is shown in fig 3.11, an operational amplifier is used in its inverted configuration. The transfer function of the amplifier is:

$$A(\omega) = -\frac{C_1}{C_F}\frac{i\omega + \dfrac{1}{R_1 C_1}}{i\omega + \dfrac{1}{R_F C_F}}, \tag{3.21}$$

and should be the inverse of the transfer function of a single exponential decay. Thus setting the product of C_1 and R_1 equal to the slow decay time constant and since there is no interest in amplifying the signal it is convenient, even if it is arbitrary, to set C_F=C_1, then the value of R_F has to be the inverse of the C_F. The phase shift after the two RC and the amplifier is equal to the one due to the slowest process but advanced by a angle of $\pi/2$ and the lifetime that can be detected when the phase shift reaches $\pi/4$ as shown in fig 3.10.

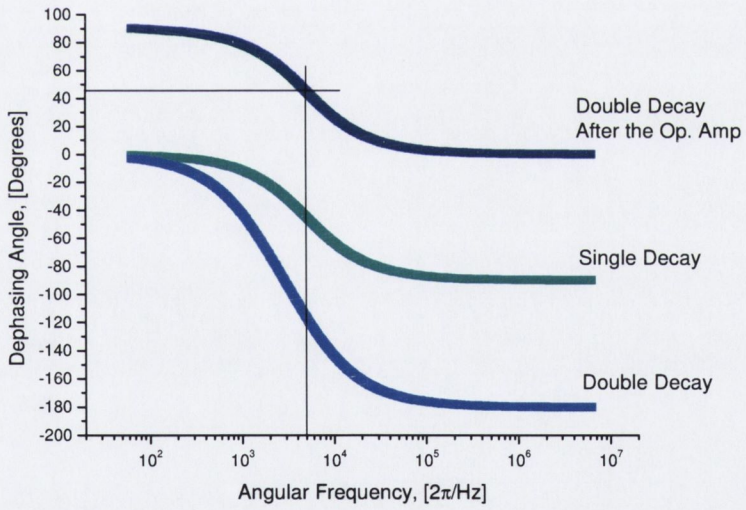

Figure 3.10: Phase shift simulated with the frequency domain technique, which allows filtering the slow decay component.

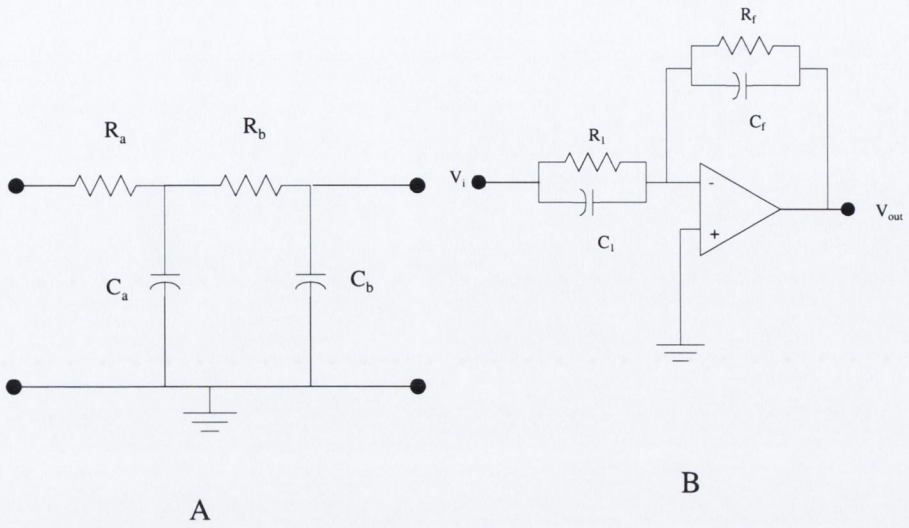

Figure 3.11: (A) A double RC circuit simulates the double decay detected for the Pr^{3+}: $^3P_0 \rightarrow {}^3H_5$; (B) the circuit that in the simulation shows effective to remove a known decay for the previous double decay.

The frequency domain technique has been implemented using the set-up in fig. 3.12. The high impedance input into the lock-in amplifier has been rendered usable at high frequency with a load resistor; in this configuration the frequency bandwidth is 5 kHz.

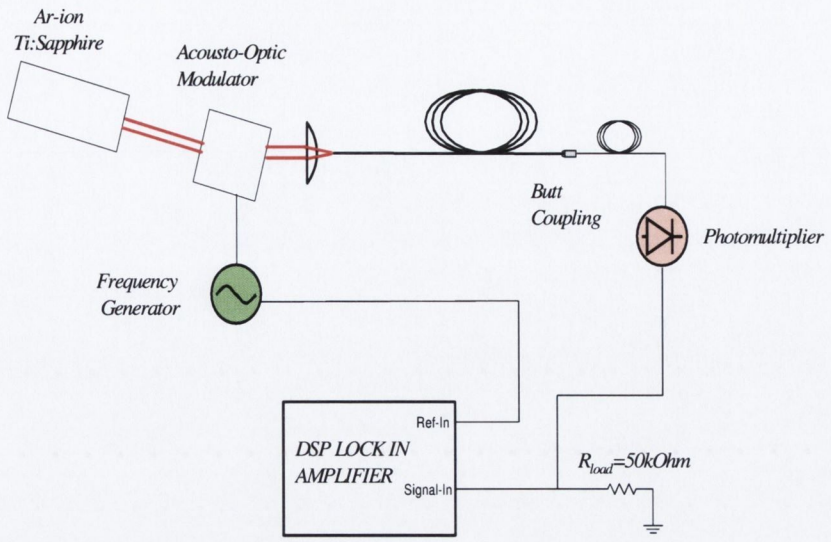

Figure 3.12:Set-up for the time domain technique, the digital oscilloscope is equipped with an input load resistor or a trans-impedance amplifier for compatibility with high frequency operation.

Even if the data taking is usually more time consuming, the phase shift is effective when a high noise background level is present which usually considerably affects the amplitude frequency roll-off.

With the set up in figure 3.12 we detected the pump frequency response (phase and amplitude) which provide the dynamic range of the system and after we detected the frequency response of the fluorescence at 540 nm of the Pr^{3+}:$^3P_0 \rightarrow {}^3H_5$ decay.

Off-line we create the frequency response of the operational amplifier using equation 3.21 then multiply the frequency response of the fluorescence by the generated $A(\omega)$.

Furthermore it was possible to extract the phase from the previously complex data and subtract it from the phase frequency response of the pump. The result is reproduced in fig. 3.13 and it shows that the phase shift approaches $\pi/4$ at a frequency of 4000 rad/s which corresponds to a lifetime of 320 μs closely in agreement with the value obtain with the time domain method.

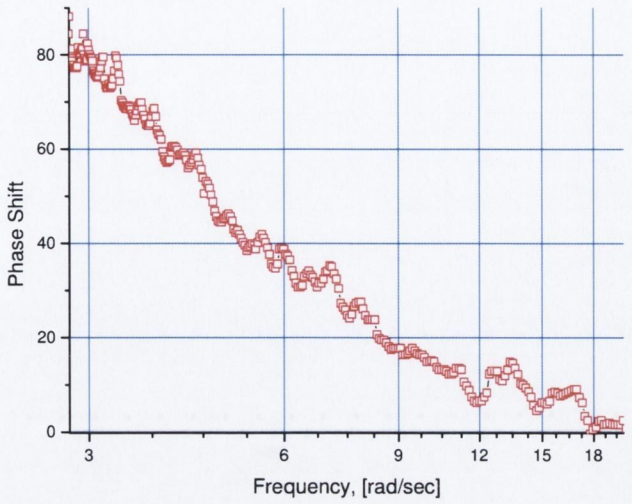

Figure 3.13: Detected phase shift with a component at 600 μs subtracted as previously discussed. The phase shift of π/4 is around 4000 rad/s which corresponds to a lifetime of 320 μs.

This method can be useful when a known decay makes difficult the identification of a second decay channel, for instance effects from cross-relaxation which usually have more complex transfer. According to the theoretical work of the Inokuti-Hirayama model [18] the transfer function for the donor ions is:

$$h(t) = e^{\left(-\frac{t}{\tau_0} - Wt\right)},$$

where the transfer rate W depends to the separation of the two ions and the type of multipolar interaction. Filtering the phase shift with a complex transfer for the known decay can be effective in calculating the dynamic of second decay mechanism usually unknown. The similarity with RC circuits enables the use of many circuit simulation programs and it allows easy off-line analysis of the frequency response of a multidecay system without the needs to solve complex integral equations.

3.7 Conclusions

In conclusion, we have demonstrated the presence of resonant transfer between Pr^{3+} and Tm^{3+} ions in ZBLA fibre at room temperature. The transfer is between the excited levels Tm^{3+}:$^1G_4$ and Pr^{3+}:$^3P_1$ and is dynamically in favour of the forward sense, due to the presence of a thermally coupled, lower energy level $^3P_0$ in the Pr^{3+} P band. The green praseodymium transition $^3P_0 \rightarrow {}^3H_5$ at 540 nm was used for monitoring the

dynamics of the transfer. Lifetime analysis of the decay of the $^3P_0 \rightarrow {}^3H_5$ transition clearly indicates that we have a coupled system. Comparison between results in fibre and preform show that in the former case there is a more complicated process of decay. Fluorescence re-absorption excited state absorption and cross-relaxation between Pr^{3+} and Tm^{3+} are the probable factors that cause the faster decay. These processes are all pump power dependent and this explains why they would appear only in the fibre.

From the reduction of the lifetime between the singly doped Tm^{3+} sample and that measured in the case of the codoped fibre, we found a resonant transfer rate for direct energy transfer of $W \approx 300 \pm 15\ s^{-1}$.

The possibility of pumping praseodymium resonantly can be advantageous for the construction of visible fibre lasers, whilst in an amplifier at 1.3 μm this option will require investigations with an optical pump source at wavelengths different than 800 nm. The presence of the excited state absorption $^1G_4$-$^3P_0$ as reported in section 3.5 is indeed an obstacle for the correct functioning of the amplifier. The small branching ratio for the $^3P_0$-$^1G_4$ relaxation seems to indicate that the resonant transfer detected would have a small impact in respect to the existing technology in an eventual amplifier.

3.8 References

[1] Y. Durteste, M. Monerie, J. Y. Allain, and H. Poignant, "Amplification and lasing at 1.3 μm in praseodymium-doped fluorozirconate fibres," *Electronics Letters*, vol. 27, pp. 626-628, 1991.

[2] Y. Nishida, M. Yamada, T. Kanamori, K. Kobayashi, J. Temmyo, S. Sudo, and Y. Ohishi, "Development of an efficient praseodymium-doped fiber amplifier," *Quantum Electronics, IEEE Journal of*, vol. 34, pp. 1332-1339, 1998.

[3] T. J. Whitley, "A review of recent system demonstrations incorporating 1.3-μm praseodymium-doped fluoride fiber amplifiers," *Lightwave Technology, Journal of*, vol. 13, pp. 744-760, 1995.

[4] J. Y. Allain, M. Monerie, and H. Poignant, "Tunable CW lasing around 610, 635, 695, 715, 885 and 910 nm in praseodymium-doped fluorozirconate fibre," *Electronics Letters*, vol. 27, pp. 189-191, 1991.

[5] M. Naftaly, A. Jha, and G. Jordan, "1.3 μm Fluorescence quenching in Pr-doped glasses," *J. Appl. Phys.*, vol. 84, pp. 1800-1806, 1998.

[6] J. Y. Allain, M. Monerie, and H. Poignant, "Energy transfer in Pr^{3+}/Yb^{3+}-doped fluorozirconate fibres," *Electronics Letters*, vol. 27, pp. 1012-1014, 1991.

[7] J. Y. Allain, M. Monerie, and H. Poignant, "Energy transfer in Er^{3+}/Pr^{3+}-doped fluoride glass fibres and application to lasing at 2.7 μm," *Electronics Letters*, vol. 27, pp. 445-447, 1991.

[8] N. J. Cockroft and K. M. Murdoch, "Energy transfer between thulium and praseodymium ions in solid," *J. of Luminescence*, vol. 60&61, pp. 891-894, 1994.

[9] N. J. Cockroft and K. M. Murdoch, "Energy-transfer processes between Tm^{3+} and Pr^{3+} Ions in $CsCdBr_3$," *Physical Reviw B*, vol. 54, pp. 4589-4602, 1996.

[10] S. C. Goh, R. Pattie, C. Byrne, and D. Coulson, "Blue and red laser action in Nd^{3+}:Pr^{3+} co-doped fluorozirconate glass," *Appl. Phys. Lett*, vol. 67, pp. 768-770, 1995.

[11] T. Sakamoto, "Spectroscopy of thulium-doped halide glass," *Hewak, D.W. (Ed.), 'Properties, processing and applications of glass and rare earth-doped glasses for optical fibres', EMIS Datareviews Series, no. 22 (Inspec, IEE, Stevenage, UK, 1998), IEE Proc.-Optoelectron.*, vol. Vol. 151, pp. 236, 2004.

[12] M. Eyal, E. Greenberg, R. Reisfeld, and N. Spector, "Spectroscopy of Praseodymium (III) in Zirconium Fluoride Glass," *Chemical Physics Letter*, vol. 117, pp. 108-114, 1985.

[13] B. R. Judd, "Optical absorbtion intensities of rare earth- ions," *Phys. Rev.*, vol. 127, pp. 750-764, 1962.

[14] D. L. Dexter, "A theory of sensitized luminescence in solid," *J. Chem. Phys.*, vol. 21, pp. 846-857, 1953.

[15] R. K. Watts and H. J. Ricther, "Diffusion and Transfer of Optical Excitation in YF_3: Yb, Ho," *Phys. Rev. B*, vol. 6, pp. 1584, 1972.

[16] R. S. Quimby and B. Zheng, "New excited-state absorption measurement technique and application to Pr^{3+} doped fluorozirconate glass," *Appl. Phys. Lett*, vol. 60, pp. 1055-1057, 1992.

[17] C. R. Giles and E. Desurvire, "Modeling erbium-doped fiber amplifiers," *Lightwave Technology, Journal of*, vol. 9, pp. 271-283, 1991.

[18] M. Inokuti and M. Hirayama, "Influence of energy transfer by the exchange mechanism on donor luminescence," *J. Chem. Phys.*, vol. 43, pp. 1978, 1965.

Chapter 4

Design and Modelling of a Thulium Doped Amplifier

4.1 Introduction

Silica optical fibres usually employed in optical communication have the lowest value of losses due to absorption from impurity and Rayleigh scattering at 1.55 μm, while the molecular resonance of SiO_2 dominates above 1.8 μm. A water absorption peak is present at wavelengths around 1.4 μm and it prevents the employment of these fibres for high speed, long haul data communication. Since this absorption peak has recently been eradicated, it has become important to find an amplifier with performances comparable to an erbium-doped amplifier.

Chapter two has underlined the capability of using Tm^{3+} doped fluoride fibres as the active medium of an amplifier for signals centred around1.47 μm. It has also been shown that Tm^{3+} doped amplifiers have limited gain due to the self-terminating nature of the 1.47-μm transition, and that they might require either two distinct optical pumps at different wavelengths or a codopant, in order to reduce the population of the terminating level.

The solution here adopted was introduced in chapter 1.1, where a Tm^{3+} doped amplifier was described, which works co-operatively with a laser at around 1.88 μm; the scope of this chapter is to address the design of this amplifier. This chapter also aims to present a theoretical model able to describe and predict the performance of the amplifier in terms of gain and threshold. This will help in the construction of the amplifier prototype, which is described in the next chapter.

It is important to underline that the amplifier will work with a single pump at 800 nm. This is a considerable advantage since it reduces the complexity which is associated with the presence of a second pump, and the wavelength is the same as the pumps used for Er^{3+} amplifiers, therefore the technology for these diode lasers exists and high powers are already available.

The energy levels of the thulium ions and the transitions involved are reported in figure 4.1. A cavity transparent to the signal wavelength is necessary in order to obtain laser oscillations between the terminating level of the 1.47 μm-transition ($^3F_4$) and the ground

state. This will reduce the steady state population of the $^3F_4$ under a 790 nm optical pump and therefore will improve the amplification within the band of wavelengths comprised between 1.47 μm and 1.52 μm. It has been shown that the transition $^3H_4 \rightarrow {}^3F_4$ peaks at 1.47 μm, however most of the values presented in this chapter are calculated at a wavelength of 1.49 μm since in the next chapter the measurements will be performed with a diode laser as reference signal emitting at 1.49 μm. Comparison between calculated and measured gain values will therefore be possible.

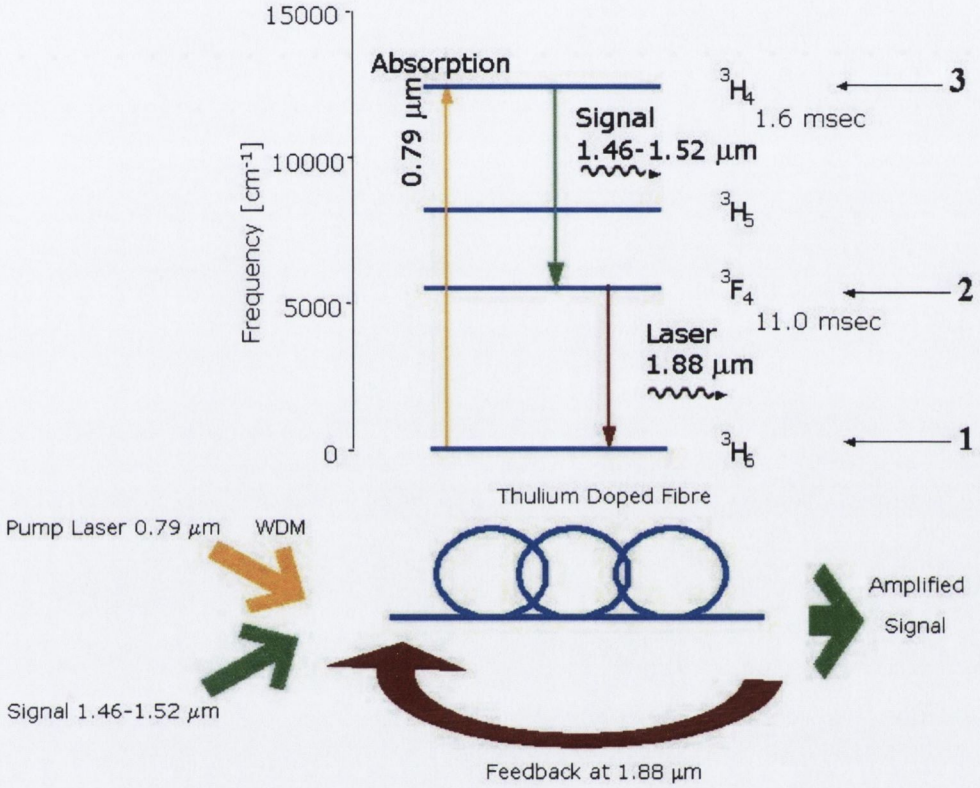

Figure 4.1: Energy levels of the Tm^{3+} ions in fluoride glass and the transitions associated with the cascade process. Below, a simple schema shows how the cooperative lasing amplification works.

4.2 Mode Analysis

A mode is a three dimensional field configuration (**E,H,k**). It is characterized by a single propagation constant β connected to the phase speed. It represents one of the possible solutions of Maxwell equations for the geometry and refractive index profile. A preliminary study of the modes supported by both the active and the transmission fibre is essential in order to design the amplifier. The fundamental equation, which governs the propagation of the light in a guiding medium as an optical fibre is the Helmholtz equation:

(4.1) $$\nabla^2 U + n^2 k_0^2 U = 0,$$

where the refractive index n is equal to the refractive index of the core n_1 when $r<a$ and $n=n_2$ in the cladding ($r>a$). The usual way to solve this problem for the cylindrical symmetry of the fibre is to express U in cylindrical coordinates as reported in figure 4.2. U which represents any of the axial components of E_z and H_z in the cylindrical coordinates can be factorised as:

(4.2) $$U(r,\phi,z) = u(r)\Phi(\phi)e^{i\beta z},$$

since solutions take the form of waves travelling in the z direction with a propagation constant β. Equation 4.2 represents a single mode while the space of the solutions is any linear system that satisfies equation 4.1 (multimodes). It is obvious that the radial and angular part of the 4.2 are independent and the solution can be separated in two equations by introducing a constant l^2. It is easy to observe that the solution of the angular part of equation 4.1 is a harmonic function $\Phi(\phi) = e^{il\phi}$ where `l` is an integer called the azimuthal mode number in order to satisfy the periodicity.

The wave is guided if the propagation constant is smaller than the wavenumber in the core and greater than the wavenumber in the cladding or:

$$n_2 k < \beta < n_1 k .$$

A way to solve the radial part $u(r)$ is to define k_T in the core and γ in the cladding as follow:

$$k_T^{\,2} = n_1^{\,2} k^2 - \beta^2,$$
$$\gamma^2 = \beta^2 - n_2^{\,2} k^2,$$

so they are both positive by definition. The radial part of eq. 4.1 for the core and the cladding can be written as:

(4.3) $$\frac{d^2u}{dr^2} + \frac{1}{r}\frac{du}{dr} + \left(k_T^2 - \frac{l^2}{r^2}\right)u = 0, (core)$$
$$\frac{d^2u}{dr^2} + \frac{1}{r}\frac{du}{dr} - \left(\gamma^2 + \frac{l^2}{r^2}\right)u = 0, (cladding)$$

Equations 4.3 have Bessel function solutions.

The parameters k_T^2 and γ^2 are associated with the rate of change of the function $u(r)$ respectively in the core and in the cladding. A large k_T^2 means a faster oscillation in the radial distribution in the core while a large γ^2 means a faster decay and a smaller

penetration of the wave into the cladding. The two bounded solutions of equations 4.3 are the Bessel's functions compatible to the present boundary conditions:

$$u(r) \propto \begin{cases} J_l(k_T r) \\ K_l(\gamma r) \end{cases} \tag{4.4}$$

The first part of 4.4 is valid within the core and is the Bessel function of the first kind, which has finite value when r tends to 0. The second is a modified Bessel function of the second kind that tends to zero as the limit when r tends to infinity.

It is useful to define the normalised frequency V, which is a dimensionless number and is connected to the number of modes that a fibre can support, as:

$$V = 2\pi \frac{a}{\lambda} NA ,$$

where λ is the wavelength and a is the radius of the fibre core and NA is the numerical aperture as defined in eq. 2.15.

The analysis presented so far is absolutely general, however an analogy with the optical ray tracing is useful in order to define a simpler representation for the solutions of equation 4.1. Meridional rays have no θ component and have transversal electric and magnetic (TE and TM) field configurations, however in the general case rays can propagate in the fibre by a spiral-like path without crossing the z axis (Surface modes). These rays (skew rays) have a mode field with both components E_z and H_z and they are usually called hybrid modes.

Usually in telecommunication single mode fibre the difference in the refractive index between core and cladding is approximate 1%, therefore the critical angle of the fibre is small and the rays guided are only paraxial. In this scenario, hybrid modes with nearly the same propagation constant can be combined in a field that is polarised in only one Cartesian direction.

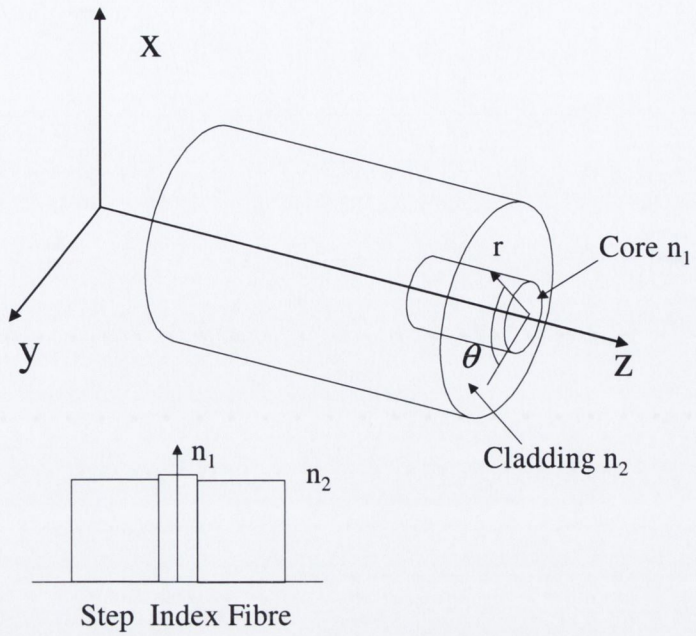

Figure 4.2 shows the cylindrical coordinate system used for analysing the mode propagation in an optical step index fibre, below: the refractive index distribution between the core and the cladding.

4.3 Characteristic Equation for the Weakly Guided Fibre

In a fibre, the paraxial limit can be obtained when $n_1 \approx n_2$, the solutions of the Helmholtz equation thus degenerate into two linear polarized modes usually noted as LP_{lm} modes and called weakly guided modes. The radial scalar function $u(r)$ is continuous and derivable, and therefore has to satisfy these conditions when the two solutions 4.4 are connected at the interface between core and cladding.

Using the normalized parameters $X = k_t a$ and $Y = \gamma a$ and imposing the condition that the radial solution is continuous and has a continuous derivative at the core-cladding boundary; from equation 4.3 the characteristic equation can be written as:

$$X \frac{J_{l\pm1}(X)}{J_l(X)} = \pm Y \frac{K_{l\pm1}(Y)}{K_l(Y)} \tag{4.5}$$

Solutions can be found graphically by plotting the right hand side against the left hand side after selecting the operation wavelength and the fundamental mode l.

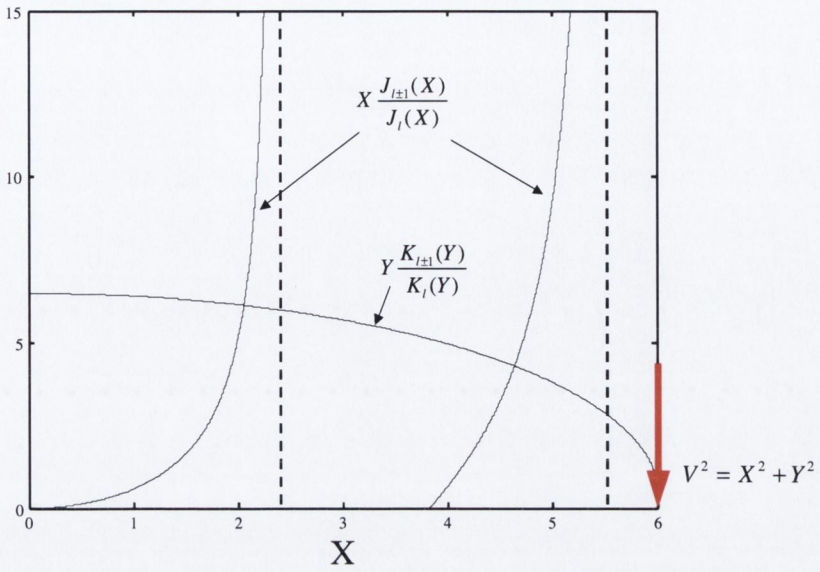

Figure 4.3 Graphic construction for solving the characteristic equation. The left- and right side of eq. 4.5 are plotted as a function of X. The number of modes is equal to the number of intersection points.

Figure 4.3 demonstrates an example for *l=0* at 633 nm in an SMF28 fibre, the right hand side and the left hand side of equation 4.5 give two intersection points which correspond to a value of *m=1,2*. The same procedure has to be repeated for integer values of `l` until the cut-off conditions where the RHS and LHS have no intersections. A preliminary analysis of the modes propagating in the fibre design to be used as the cavity of the fibre amplifier has been performed. The aim is to obtain information in the way that the optical fields propagate in the fluoride fibre and how the quality in butt-coupling the fluoride fibre with common silica transmission fibre, for instance Corning SMF28. The characteristics of the two active fluoride fibres that will be used in order to construct the amplifier cavity are given in table 4.1

Table 4.1: ZBLA thulium doped fibres characteristics that will be used in the construction of the amplifier

	Unit	*Fibre #1*	*Fiber#2*
NA		0.234	0.17
Core Diameter	μm	3.2	4.4
Length	m.	2.4	4.0
Cut-off λ	μm	1.05	1.0
Doping	p.p.m.	2000	2000

4.3.1 **Single Mode**

The fundamental mode supported by the two fibres above the cut-off wavelength is the quasi-Gaussian intensity profile shown in fig.4.4. The shape closely fits a Gaussian function, having a width ω and this defines the mode field diameter as:

$$I(r)=E_{LP01}^2(r)=\exp\left(-2\left(\frac{r}{\omega}\right)^2\right).$$

The confinement factor is defined as the fraction of the total power that resides in the core:

$$\Gamma=\frac{P_{core}}{P_{core}+P_{clad}}=\frac{\left(\int_0^a E_{LP01}^2 dr\right)}{\left(\int_0^\infty E_{LP01}^2 dr\right)}, \tag{4.7}$$

where a is the radius of the core. Equation 4.7 can be integrated numerically, or recalling the approximation for the error function:

$$erf(x)\approx 1-\frac{e^{-x^2}}{\sqrt{\pi}}\left(1-\frac{1}{2x^2}+\frac{3}{4x^4}-\frac{15}{8x^6}\right),$$

it is possible to obtain an approximated function for the core confinement as:

$$\Gamma=\frac{\sqrt{\pi}}{2}\left[1-\frac{e^{-\frac{2a^2}{\omega^2}}}{\frac{\sqrt{2\pi}a}{\omega}}\left(1-\frac{\omega^2}{4a^2}+\frac{3\omega^4}{16a^4}-\frac{15\omega^6}{64a^6}\right)\right].$$

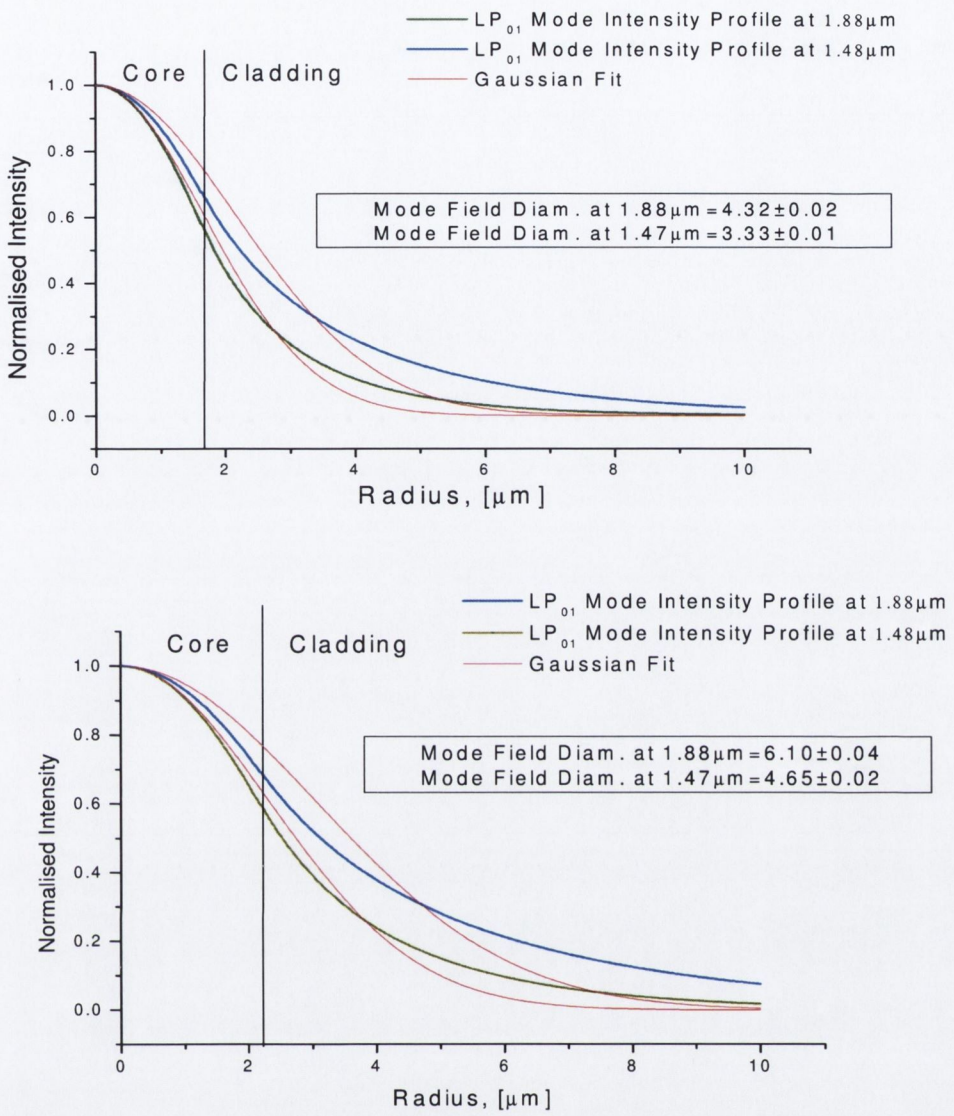

Figure 4.4: LP_{01} intensity profile for the two fibres at the signal and laser wavelengths.

The results are reported in table 4.2 and in figure 4.5. At higher wavelengths it is noticeable that an increasing amount of power travels in the cladding, therefore the amount of photons that interact with the core dopant is necessary smaller.

Table 4.2: Values for the core confinement factor at the signal end laser wavelngths

Integrals:	**Fibre#1**	**Fibre#2**
Mode Field Diameter Signal 1.49μm	3.33 μm	4.65 μm
Core Confinement %, Signal 1.49μm	94%	80%
Mode Field Diameter Laser 1.88μm	4.32 μm	6.10 μm
Core Confinement %, Laser 1.88μm	83%	68%

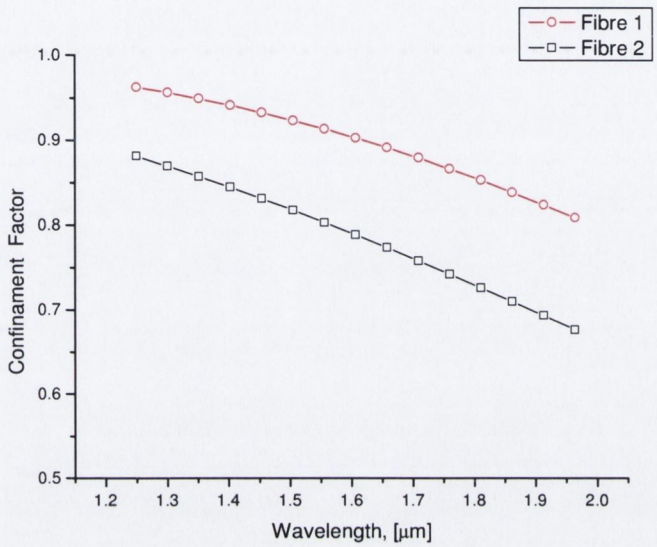

Figure 4.5: Power of LP_{01} mode in the core for the two fibres tested, at different wavelengths.

4.3.2 **Multimode**

Below the cut-off wavelength, the two fluoride fibres also support higher order modes. Together with the fundamental LP_{01}, the characteristic equation 4.5 has a solution for $l=1$ so the LP_{11} mode is also supported. The intensity plots for the two modes and the two fibres are presented in fig. 4.6, the central cylinder represents the core of the fibre. It is evident that the higher NA of the fibre 1 gives better core confinement than the lower NA of fibre 2. This gives fibre 1 a smaller absorption length and a smaller sensitivity to losses due to fibre bending.

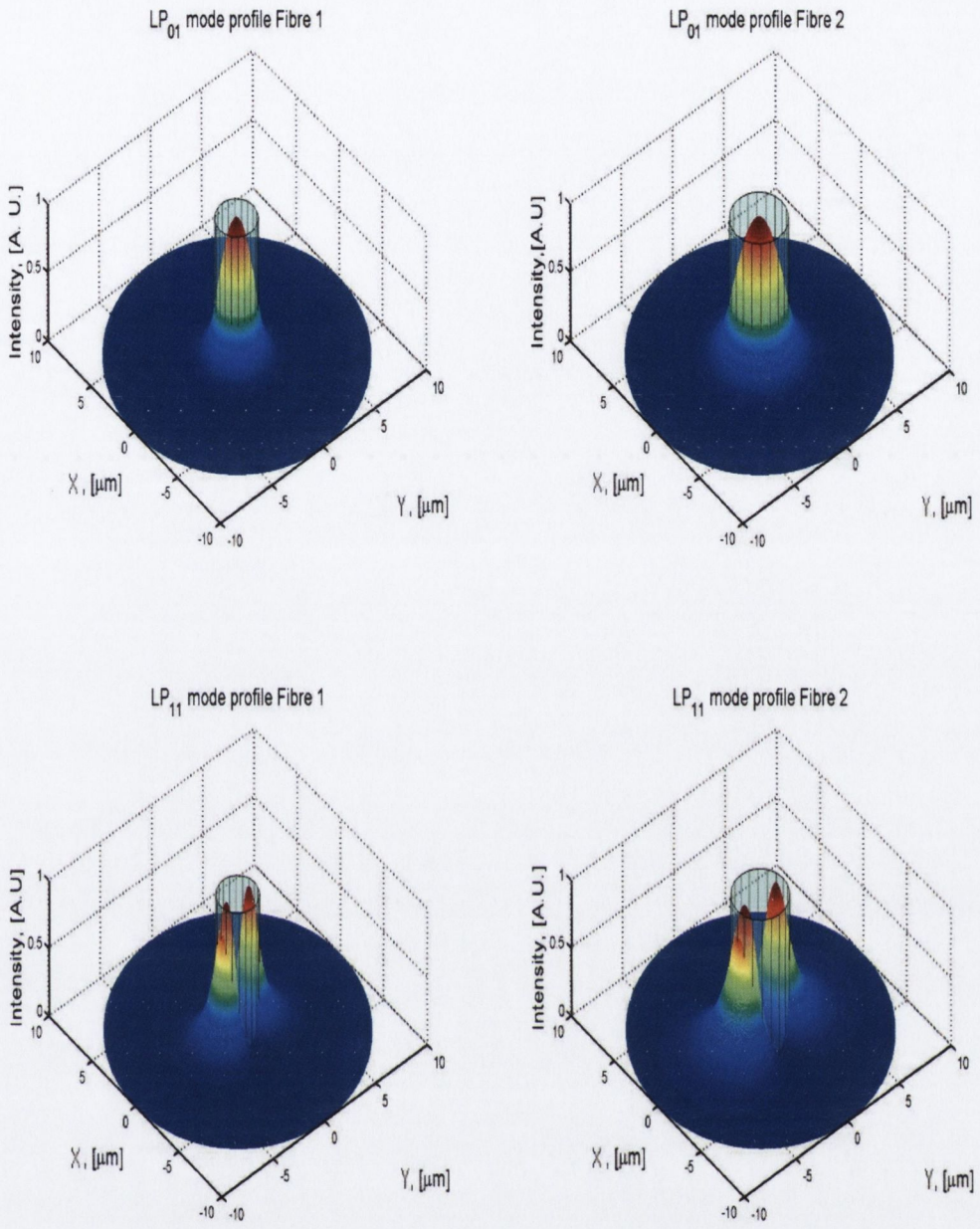

Figure 4.6: Intensity profile of the LP_{01} and LP_{11} for the two thulium doped ZBLA fibres. The cylinder shows the core of the fibre. Fibre 1 with large NA has greater confinement with respect to the fibre 2, which has lower NA.

4.4 Interface Losses

The calculation above can be used to analyse the theoretical losses due to the mismatch in radius and NA between the active and the transmission fibre when the two fibres support only the fundamental LP_{01} mode.

The transmission at the interface can be calculated by numerical integration of the two fields involved according to:

(4.8)
$$\eta = \frac{\left(\int_0^\infty E_f E_s \, dA\right)^2}{\left(\int_0^\infty E_f^2 \, dA\right)\left(\int_0^\infty E_s^2 \, dA\right)}$$

where E_f is the LP_{01} electric field in the fluoride fibre while E_s is in the SMF28 fibre over the cross-section A. The result for the two fibres is shown in table 4.3, the value for 1.49 μm can be directly compared with the one experimentally observed, since the thulium fibre is transparent at this wavelength. Usually this value strongly depends on the quality of the cleaving and how accurately the two fibres have been joined together and is typically slightly worse than the estimate. A detailed description of the problems related to fibre butt coupling is postponed to the next chapter.

In figure 4.7 the expected transmission for the two fibres are shown when they are butt-coupled with a transmission fibre SMF 28, the test point represent the transmission measurements performed for comparison with the previous calculations. The mode matching for the two fibres therefore improves with the increase of the wavelength.

Table 4.3: Extimated transmission at the fluoride-transmission fibres interface.

Integrals:	**Fibre#1**	**Fibre#2**
Interface transmission at 1.88 μm	92-94 %	96-98 %
Interface transmission at 1.49 μm	84-82 %	94-92 %

4.5 Thulium Doped Fibre Laser and Amplifier Model.

Modelling rare-earth doped fibre lasers and amplifiers is well described in the literature. It is worth mentioning some work relating to thulium doped fluoride fibre lasers and amplifiers: Jackson [1] describes a model for thulium in silica fibre laser, Duclos and Urquhart [2] Paschotta *et al.*[3] have reported models for blue fluoride Tm^{3+} fibre lasers, Komukai and Kasamatsu [4, 5] have modelled an upconversion thulium fluoride fibre amplifier at 1.47 μm.

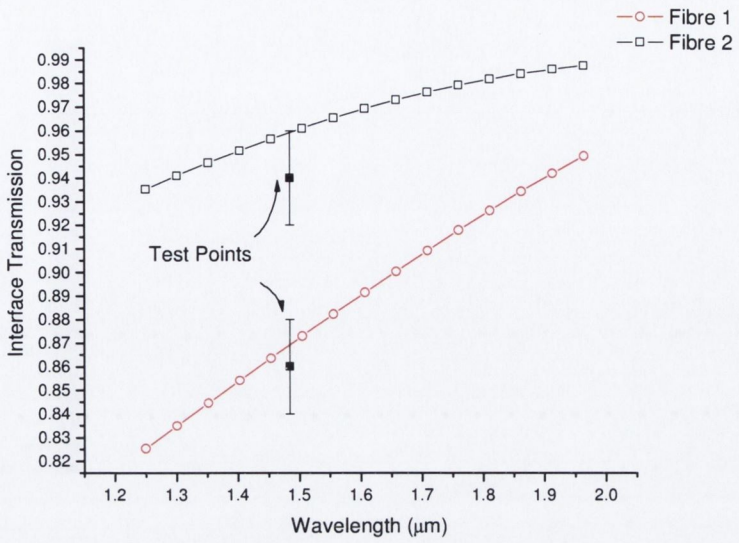

Figure 4.7: Transmission due to the presence of the interface between the two fluoride fibres and the transmission fibre. The two test points are directly measured values for the two fibres.

The previous models are based on the numerical integration of rate equations which describe the dynamics of the occupation number of the relevant energy levels, and the propagation equations of the fields. Usually these types of models are referred to as phenomenological as they are based on a set of measured parameters that need to be evaluated for each type of dopant in each type of host material.

There are a considerable amount of spectroscopic studies available and most of the physical quantities in the literature are reliable and verified; other parameters have been directly calculated in chapter 2.

The solution of the rate equations may have a possible analytical solution [6] as was shown in section 2.11, however the analytical solution ,despite giving insight into the physical process involved in a fibre amplifier or laser, is usually quite complex and a poor engineering tool, moreover the effect of saturation is not analytically obtainable due to its non-linear nature [7]. Numerical solutions are very well known and they represent a more flexible tool in terms of design and simulation of the performance of a fibre oscillator. However there are some limitations, especially if multiple solutions at different wavelengths are required. If the number of differential equations that has to be solved became excessive the computational time needed to achieve a converging solution could be unsustainable.

Models for a fibre laser are generally more complex than the amplifiers and require the solutions of differential equations with two given boundary conditions that give the reflectivity of the cavity, while the general solution for the ion populations is usually calculated algebraically in the steady-state limit.

Currently there are numerical engines based on the fourth order Runge-Kutta or similar algorithms, which are able to solve two boundary condition problems. The concept underpinning the solution is the splicing of the active fibre (specific to our case) into small incremental lengths Δz where the model's variables are constants as shown in fig. 4.8. Most engines are based on a variable incremental length and so it is essential to write the equations in such a fashion that the length of the slice does not appear explicitly. It is worth stressing the importance of creating proper guess solutions for the equations involved in order to have a fast and reliable convergence.
Working with population density as the number of Tm^{3+} ions per unit of volume is usually the best approach; for consistency the power of the optical fields P_j have to be expressed in term of photon flux i.e. the photon rate per unit of mode field area:

$$\Phi_j = \frac{P_j}{\left(\frac{\pi\omega_j^2}{4}\right)h\nu_j}, \tag{4.9}$$

with $j = p, s, l$ where p is for pump (790 nm), s is for signal (1.47 μm) and l is for laser (1.88 μm).

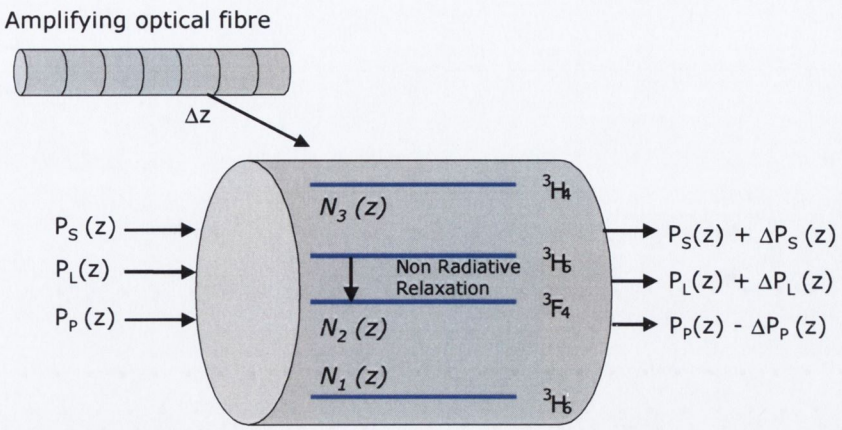

Figure 4.8: Graphical representation of the idea behind the construction of the model.

Due to the bi-directional nature of the laser oscillator, at 1.88 μm, it is necessary to take into account the two fluxes, one counter propagating to the other.

The possibility of simultaneous optical pumping from the both ends of the amplifier exists and so a possible co and counter-propagating scenario has also been considered so the following equations will contain two pump fluxes one propagating in the z positive direction and one propagating in the z negative direction.

The rate equations for each level are expressed in terms of the population density N_i (Number of ions per unit of volume) of all the relevant levels ($i=1$ $^3H_6$, $i=2$ $^3F_4$, $i=3$ $^3H_4$, reproduced in fig.4.1) as:

$$\begin{aligned}
\frac{dN_1}{dt} &= -w_p N_1 + w_l^e N_2 - w_l^a N_1 + A_{31} N_3 + A_{21} N_2, \\
\frac{dN_2}{dt} &= -w_l^e N_2 + w_l^a N_1 - w_s^a N_2 + w_s^e N_2 + A_{32} N_3 - A_{21} N_2, \\
\frac{dN_3}{dt} &= +w_s^a N_2 - w_s^e N_2 - A_{32} N_3 - A_{31} N_3.
\end{aligned} \tag{4.10}$$

where A_{ij} is the probability of spontaneous emission between the levels i and j and w_p is the pump transition rate expressed as:

$$w_p = \sigma_{abs}^{1-3}(\Phi_p^{+}(z) + \Phi_p^{-}(z)),$$

with $\Phi_p^{\pm}$ the co (+) and counter (-) propagating power for the pump. In the case of a single pump the counter propagating flux has been taken as the Fresnel reflection at the opposite fibre end.

The transition rates $w_l^{a,e}$, $w_s^{a,e}$ are respectively the absorption (superscript a) and stimulated emission (superscript e) rates at the signal and the laser wavelengths:

$$\begin{aligned} w_l^{a,e} &= \sigma_{a,e}^{1-2}(\Phi_l^{+}(z)+\Phi_l^{-}(z)), \\ w_s^{a,e} &= \sigma_{a,e}^{2-3}\Phi_s(z). \end{aligned} \qquad (4.11)$$

$\Phi_l^{\pm}$ are the laser fluxes which are created by the feedback and Φ_s is the signal photons flux which propagates in a single direction. The population densities are also subject to the conservation law: $N_{tot} = N_1 + N_2 + N_3$. The steady state solutions of equations 4.10 at the z point of the fibre can be obtained by setting the derivatives to zero and solving the associated linear equation system.

The evolution of the signal, pump and laser fields in the fibre has to be solved simultaneously with the rate equations for the levels:

$$\begin{aligned} \frac{dP_p^{\pm}}{dz} &= \mp\Gamma_p\sigma_a^{1-3}N_1; \\ \frac{dP_l^{\pm}}{dz} &= \pm\Gamma_l(\sigma_a^{1-2}N_1 - \sigma_e^{1-2}N_2) \\ \frac{dP_s}{dz} &= +\Gamma_s(\sigma_e^{3-2}N_3 - \sigma_a^{3-2}N_2) \end{aligned} \qquad (4.12)$$

These equations take into account the evolution of the power in the LP_{01} mode for the signal and laser along the fibre length. The signs are related to the forward and backward propagation in the cavity.

The signal power boundary condition is uniquely determined by the geometry where the signal is injected to the fibre at $z=L$ for both of the configurations so:

$$P_s(L) = P_s \qquad (4.13)$$

For the pump there are two different boundary conditions for the two configurations for the fibre 1 where a single pump with pump power P_0 will be used:

$$\begin{aligned} P_p^{-}(L) &= R_p P_p^{+}(L), \\ P_p^{+}(0) &= R_p P_p^{-}(0) + P_0. \end{aligned} \qquad (4.14)$$

The R_p is the reflectivity at both ends of the thulium fibre, this value is of the order of 5% since the contribution of the amount of power that travels through the loop is negligible due to an isolation of –15 dB.

When two pumps are present, the pump for the other end of the fibre has to be considered, supposing it has the same power P_0 then 4.12 changes to:

$$P_p^-(L) = R_p P_p^+(L) + P_0,$$
$$P_p^+(0) = R_p P_p^-(0) + P_0. \tag{4.15}$$

Finally, the boundary condition for the laser can be written as:

$$P_l^-(0) = R_l P_l^+(L),$$
$$P_l^+(L) = R_l P_l^-(0), \tag{4.16}$$

where R_l is the total transmission of the fibre loop at the laser wavelength with the losses due to the transmission fibre and fluoride fibre subtracted.

The bimodal nature of the pump where also the higher order mode LP_{11} is supported make the determination of the confinement factor rather difficult due the unknown distribution of the power between the two travelling modes. This problem has been evaluated by scaling that estimated in the model with the experimental absorption length observed in terms of the residual pump at the fibre end. The previous measurements have been performed for a power lower than threshold in order to avoid laser oscillation that will change the absorption length.

The two parameters $\Gamma_p(fibre\#1) = 0.72 \pm 0.02$ and $\Gamma_p(fibre\#2) = 0.52 \pm 0.16$ have been found experimentally, no others parameter have been used. The values are reported in table 4.4, together with the spontaneous emission rate A_{ij}. The population of the intermediate level $^3H_5$ has been taken equal to zero since this level is strongly depopulated by non-radiative relaxation.

In figure 4.9 the expected power for the laser at 1.88 μm is shown, it is interesting to notice that as expected in the case of fibre two due to the longer cavity the saturation is not achieved and at 400 mW is still exponential.

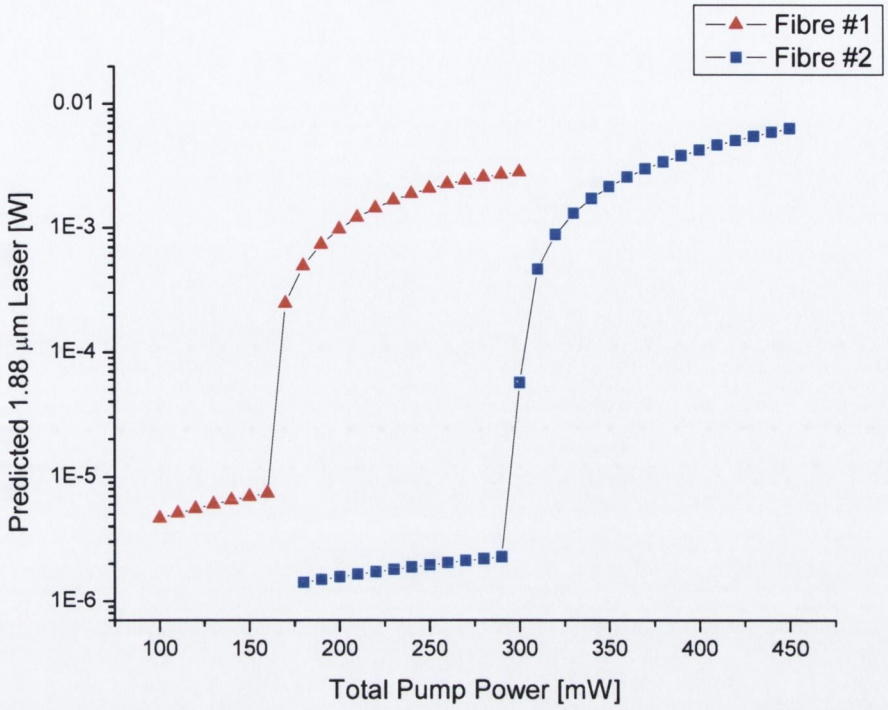

Figure 4.9: Predicted value of the power of the laser and the relative threshold.

The lower value of the fluorescence for the fibre 2 is due to the lower NA of the fibre that allows a lower amount of fluorescence light to be gathered along the cavity.
The gain expected in the small-signal limit is reported in figure 4.10 for the two fibres and the two different pumping schemes, the longer cavity again shows no gain saturation up to 450 mW total pump power.

Table 4.4: Values used in the model.

Parameter	Unit	Symbol	Value	Remarks
Tm^{3+} conc.	$1/m^3$	ρ	$3.2x10^{25}$	Estimated
GSA	m^2	σ_a^{1-3}	$2.3x10^{-25}$	Measured (ch. 2)
Stimulated Emission Cross Section 1.49μm	m^2	σ_e^{2-3}	$1.5x10^{-25}$	Measured (ch. 2)
ESA 1.49 μm	m^2	σ_a^{2-3}	$0.9x10^{-25}$	Measured (ch.2)
Stimulated Emission Cross Section 1.88μm	m^2	σ_e^{1-2}	$7.1x10^{-25}$	[8]
GSA 1.88 μm	m^2	σ_a^{1-2}	$1.2x10^{-25}$	[8]
Spontaneous rate level 3-1	s^{-1}	A_{31}	1271.9	[9]
Spontaneous rate level 3-2	s^{-1}	A_{32}	75.1	[21]
Spontaneous rate level 2-1	s^{-1}	A_{21}	123.8	[21]

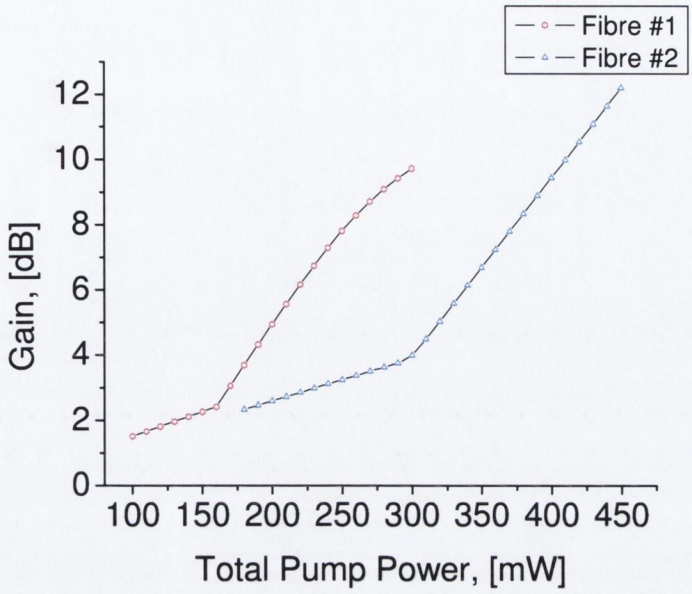

Figure 4.10: Expected gain for the two cavity lengths and the two pumping schemes

In figure 4.11 the predicted gain of the amplifier versus the signal input power is shown, which shows the good saturation characteristic of the amplifier for the longer cavity length. The gain is constant up to a launched signal power of approximately 0.1 mW (-10 dBm) when the gain starts to roll-off. The region where the signal amplification does not reduce, appreciably, the gain of the amplifier is usually called small-signal region. Therefore, the small-signal gain is defined as the gain corresponding to a small but practical input level within this region.

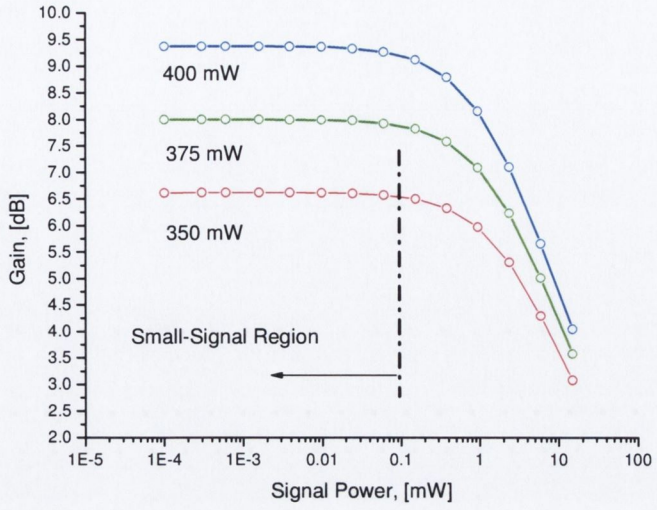

Figure 4.11: Predicted saturation point of the amplifier with a 4 m. cavity length. The 3 dB compression point is around 10 mW. In the plot, the vertical line corresponds to the boundary of the small signal region (≈ 0.1 mW)

The model has been fully written in MATLAB using the function bvp4c [10] for the resolution of two boundary condition problems. The bvp4c is a finite difference code that implements the 3-stage Lobatto IIIa formula, which provides a continuous and continuous first derivative (C^1) solution in the integration interval. Mesh selection and error control are based on the residual of the solution, the solver determines a numeral solution; a global system of algebric equations compatible with the boundary conditions and the relative error is accounted. If the determined error does not satisfy the tolerance criteria, the solver re-adapts the mesh and repeats the process.

The guess solutions for the pump absorption used is:

$$P(z) = P(0)e^{-\frac{z}{L'}},$$

where L' is the generalised absorption length defined in section 2.11 whilst for the signal propagation the gain coefficient along the fibre is derived from the equation 2.38. Above threshold, the power for the 1.9 μm radiation inside the cavity can be assumed constant. Starting for high pump power the system proceeds to calculate the output gain, lowering the pump power for each step of the calculation. The semi-analytical guess solution is used only for the first point, while for the following points, the solution previously obtained is used as guess solution.

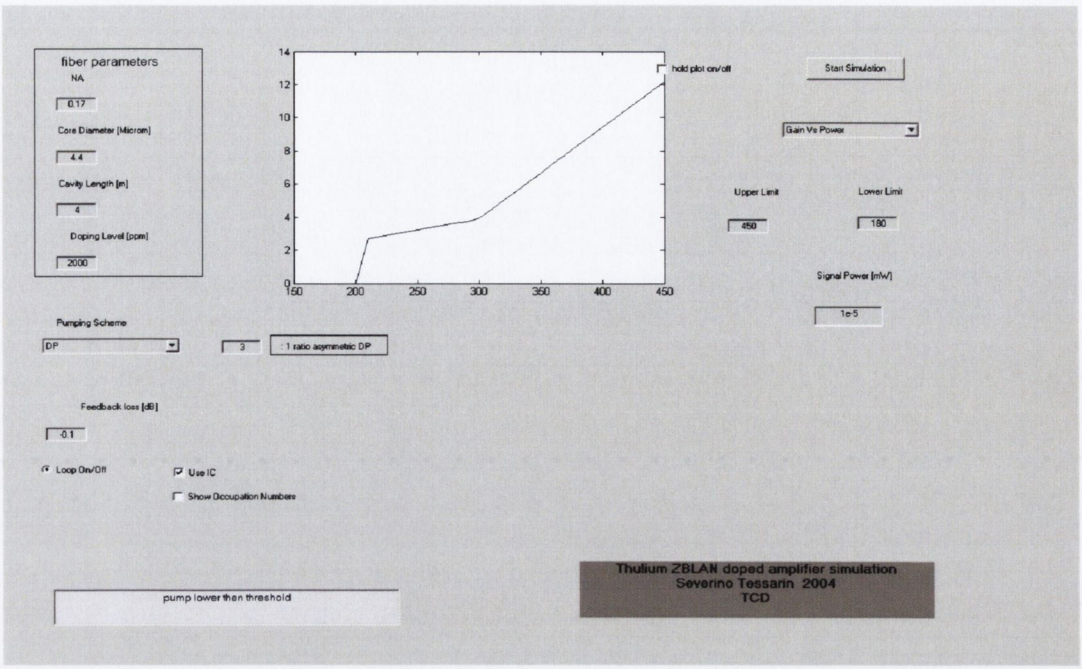

Figure 4.12: GUI of the model.

A Graphical User Interface (GUI), presented in figure 4.12 has been designed to aid the user for creating different simulations.

4.6 Conclusions

In this chapter a comprehensive description of the rate equation model has been given. The model has been adopted in order to describe a Tm^{3+} doped amplifier working in cascade with a laser at 1.88 μm which allowed the enhancement of the population inversion between the amplifying levels, in which the long lifetime of the terminating level reduces the available gain.

The two fibres that will be used in order to create the cavity were studied in terms of the relevant parameters that appear in the model; confinement factor and losses between the active fibre and the transmission fibre at the two important expected wavelengths of the laser and the signal were determined. The bimodal nature of the pump creates problems in the theoretical determination of the confinement factor and losses. The former were determined experimentally while the latter will be estimated in chapter 5.8.

The model was written in order to support different pumping schemes and large signal dynamic ranges. It shows the possibility of predicting the threshold of the laser at 1.88 μm with an output of several mW. Moreover the model gives a preliminary

characterization of the amplifier in terms of pump power required and expected gain at 1.49 μm.

4.7 References

[1] S. D. Jackson and T. A. King, "Theoretical modeling of Tm-doped silica fiber lasers," *Lightwave Technology, Journal of*, vol. 17, pp. 948-956, 1999.

[2] F. Duclos and P. Urquhart, "Thulium-doped ZBLAN blue upconversion fibre laser: theory," *J. Opt. Soc. Am. B*, vol. 12, pp. 709-717, 1995.

[3] R. Paschotta, P. R. Barber, A. C. Tropper, and D. C. Hanna, "Characterization and modelling of thulium ZBLAN blue upconversion fibre lasers," *J. Opt. Soc. Am. B*, vol. 14, pp. 1213-1218, 1997.

[4] T. Komukai, T. Yamamoto, T. Sugawa, and Y. Miyajima, "Upconversion pumped thulium-doped fluoride fiber amplifier and laser operating at 1.47 μm," *Quantum Electronics, IEEE Journal of*, vol. 31, pp. 1880-1889, 1995.

[5] T. Kasamatsu, Y. Yano, and T. Ono, "1.49-μm-band gain-shifted thulium-doped fiber amplifier for WDM transmission systems," *Lightwave Technology, Journal of*, vol. 20, pp. 1826-1838, 2002.

[6] C. Barnard, P. Myslinski, J. Chrostowski, and M. Kavehrad, "Analytical model for rare-earth-doped fiber amplifiers and lasers," *Quantum Electronics, IEEE Journal of*, vol. 30, pp. 1817-1830, 1994.

[7] C. R. Giles and E. Desurvire, "Moddeling erbium-doped fiber amplifiers," *Lightwave Technology, Journal of*, vol. 9, pp. 271-283, 1991.

[8] R. M. Percival, D. Szebesta, C. P. Seltzer, S. D. Perin, S. T. Davey, and M. Louka, "A 1.6-μm pumped 1.9-μm thulium-doped fluoride fiber laser and amplifier of very high efficiency," *Quantum Electronics, IEEE Journal of*, vol. 31, pp. 489-493, 1995.

[9] T. Sakamoto, "Spectroscopy of thulium-doped halide glass," *Hewak, D.W. (Ed.), 'Properties, processing and applications of glass and rare earth-doped glasses for optical fibres', EMIS Datareviews Series, no. 22 (Inspec, IEE, Stevenage, UK, 1998), IEE Proc.-Optoelectron.*, vol. Vol. 151, pp. 236, 2004.

[10] L. F. Shampine, M. W. Reichelt, and J. Kierzenka, "Solving Boundary Value Problems for Ordinary Differential Equations in MATLAB with bvp4c ftp://ftp.mathworks.com/pub/doc/papers/bvp/."

Chapter 5

Fibre Ring Amplifier: Results

5.1 Introduction

Erbium doped silica amplifiers cover the region of wavelengths around 1.55 μm, their development was boosted by the research in the Optical Research Centre (ORC) in Southampton University which extended the vapour deposition process in order to fabricate single mode rare earth doped fibres [1]. In the short period from1988-2002, a prototype dye laser pumped amplifier [2] moved from research laboratories to industrial applications with erbium amplifiers pumped with laser diodes at 0.98 μm in the form of compact and highly efficient modules with a gain in excess of 30 dB [3].

The zero dispersion 1.3 μm telecommunications window still maintains a large importance since most of the fibre deployed worldwide operates at this wavelength. Nd^{3+} doping failed to be effective since large signal excited state absorption remains even in zirconium based fibre [4]. Praseodymium doped fluoride fibres were shown to be a possible dopant in fluoride fibres, and most of the research effort was aimed at solving the problem of the low efficiency of the 1.3 μm-transition and low absorption cross-section at the most effective 1.06 μm pump wavelength [5] [6].

Thulium doped zirconium fluoride based fibres seem attractive in covering the region around 1.47 μm as has been demonstrated theoretically in the previous chapter, but the self-terminating nature of the amplifying transition requires either a second suitable acceptor that is able to reduce the lifetime of the terminating level or a two-wavelength upconversion pumping scheme.

The previous chapter described a possible design of a thulium doped fluoride amplifier where the terminating level is depopulated by establishing laser oscillation between the terminating level of the 1.47μm-transition and the ground state. With this approach significant amplification will be obtainable with a single 790 nm pump. A phenomenological model was developed in order to predict the amplifier performance; parameters such as the lifetime of the metastable states, absorption and emission cross-sections have been either taken from the literature or experimentally estimated. Further studies of the mode confinement allowed the determination of the impact on the amplifier performance of the fibre's physical proprieties. Fibre NA, core radius and the

length of the cavity have therefore been related to the expected behaviour of the amplifier.

The characteristic of the active fibres used in this work were the same as reported in table 4.1, the two fibres have length of 2.4 and 4 m and are the available quantity, but they are also, as we have seen in the previous chapter, a good compromise between the expected threshold and the pump power available from the *in situ* Ti:Sapphire lasers.

The two fibres available have different NA and different radii; the fibre with higher NA needs a lower fibre radius in order to allow monomode operation at telecommunication wavelengths. This gives higher losses between the active fibre and the transmission fibre; however higher NA fibres produce higher optical gain coefficient due to the higher confinement factor. The fibre with lower NA will reduce the cavity losses so reducing the threshold power needed in order to establish oscillation at 1.88 μm, this allows the use of a longer active fibre length.

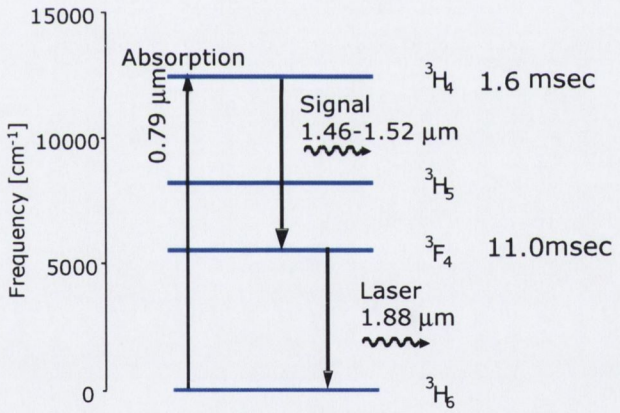

Figure 5.1: Energy levels and transitions of the Tm^{3+} ions in fluoride glass

The relevant energy levels for trivalent Tm^{3+} ion in fluoride glass are shown in figure 5.1. The transition $^3H_6 \rightarrow {}^5H_4$ centred at 0.79 μm, is ideal for optical pumping since it has a large absorption cross-section and cheap and reliable GaAs laser diodes for pumping have already been manufactured at this wavelength.

In order to improve the steady state population difference between the two states a lasing transition at 1.88 μm between the $^3H_4$ and the ground state has been created. The

supporting laser oscillation will keep the population of the level lower level just above inversion, reduces the bottleneck effect and allows higher efficiency for amplification. The enabling oscillation at 1.88 μm has been achieved by embedding the active Tm^{3+} doped fibre in a ring cavity formed by two chromatic fibre couplers.

The fluorescence of the transition $^3H_4 \rightarrow {}^3F_4$ is peaked at 1.47 μm, however gain measurements performed in this chapter used a laser diode as reference with wavelength of 1.49 μm, the spectral characterization will show that at this wavelength the gain is maximum.

5.2 Construction and Characterization of the Chromatic Couplers

The main feature of the amplifier is the ring-cavity configuration, the ring cavity has been constructed with the aid of two identical 2x1 chromatic couplers knows as Y-coupler see fig.5.2

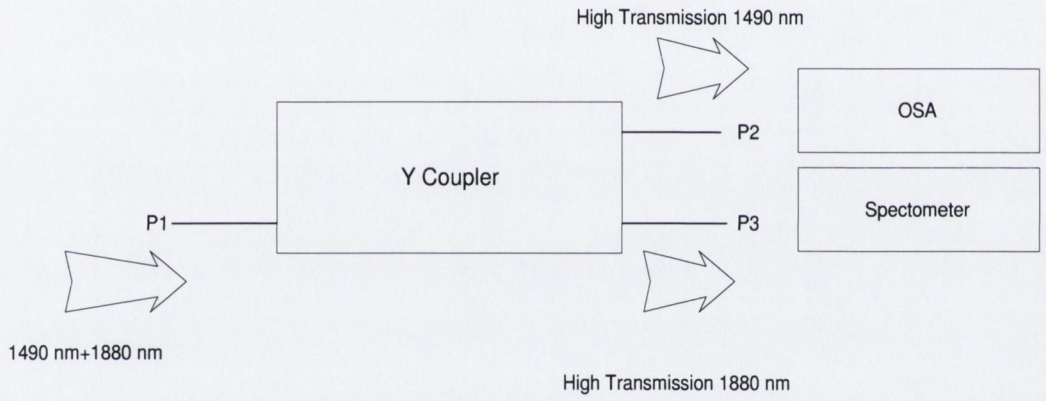

Figure 5.2: Schematic diagram of the chromatic couplers used in the construction of the amplifier.

A thulium-doped fibre has been placed between two ports of two Y-couplers produced from Corning SMF28 fibre. One port has been designed in order to be highly transparent around 1.88 μm, the other port has high transmission centred at 1.47-1.50 μm.

The chromatic fibre couplers are the fibre equivalent of optical beam-splitters. They can be manufactured by the fused biconical taper technique, in which two fibres twisted around each other are heated and fused while the two stages of the fusion system are moved steadily apart. A real-time monitoring will stop the fusion process when the couplers meet the required transmission at the required wavelength. After being fused, the fibres form a single waveguide so the propagation does not occur in the core but in

the common cladding, because the fundamental mode in the input fibre is at cut-off (V<<1).

The major construction difficult is due to the difficulty of measuring the transmission at 1.88 μm during the construction process; since the real-time monitor works only up to 1.6 μm so the transmission at 1.88 μm should be measured after the fibre coupler has been made. It might require several trials before obtaining a fibre coupler which has the expected performance.

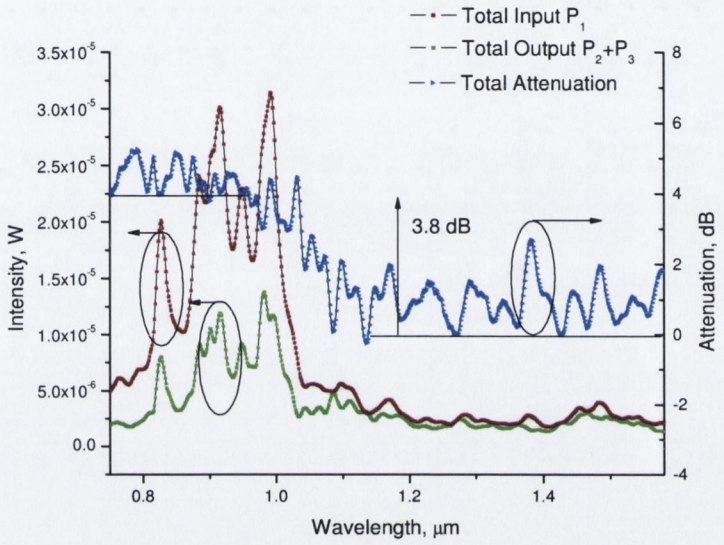

Figure 5.3: On the left is shown the total power coupled in the port P_1 and the sum between the output power from the port P_2 and P_3 of the chromatic coupler. Right the total attenuation is calculated.

Figure 5.3 shows the total power injected from a high power incoherent polychromatic source (Xenon-Lamp) and the total output power detected in the two couplers output ports. Notice that the total power drops of a factor of 3.8 dB from wavelength below 1 μm to the low-loss region above 1.2 μm. This difference in the low and high loss region is essentially due to the presence of higher order modes and to the geometry of the tapered part of the coupler. During the fabrication the core radius decreases while the ratio between core and cladding remains constant; if the angle is small there is low coupling between the fundamental and the higher mode (adiabatic coupling).

A length scale L can be defined, according to scattering theory as [7]:

$$L = \frac{a(z)}{\tan \Omega(z)}, \tag{5.1}$$

where $a(z)$ is the local core fibre radius and $\Omega(z)$ is the angle between the tangent of the core cladding interface and the fibre axis z as depicted in fig.5.4. If the length scale L that defines the uniformity of the taper is bigger than the wavelength in silica:

$$\frac{\lambda}{n} < L, \tag{5.2}$$

there is substantial loss and a non-adiabatic behaviour for the different guided modes.

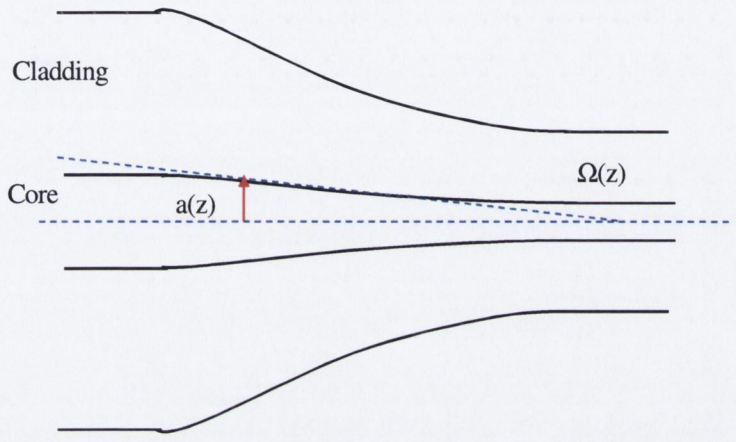

Figure 5.4 Schematic diagram of the tapered region of the chromatic coupler, measurements show that the length scale of uniformity is of the order of 0.8 μm

The spectral response of the chromatic coupler was characterised by detecting the attenuation from the output port 1 with an OSA and from the output port 2 with a half-meter spectrometer equipped with an InGaAs photodetector with a spectral response peaked at 2.1 μm. The difference in the maximum attenuation visible in fig 5.5 with respect to the attenuation measured from the two ports of the chromatic fibre couplers, is due to the larger dynamic range of the OSA compared with the spectrometer.

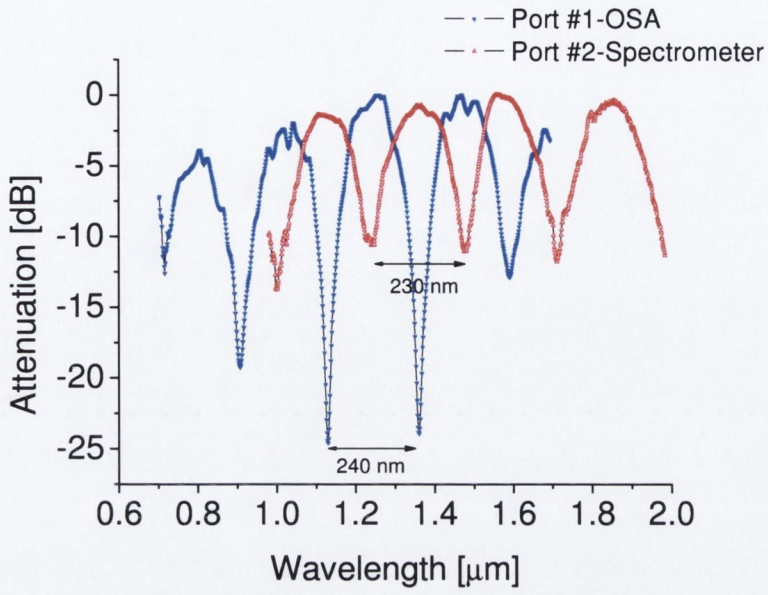

Figure 5.5: Attenuation measured in the two ports of the chromatic coupler.

A sinusoidal function fits the coupler wavelength response:

$$P(\lambda) = \frac{1}{2}\left[1 + \sin\left(\frac{2\pi}{\delta\lambda}(\lambda - \lambda_m)\right)\right], \tag{5.3}$$

where $\delta\lambda$ is the coupler period which is an average value of 235 nm.

For port 1, the first maximum that is taken into account is around 1 μm so λ_m=0 while for port 2 the maximum is shifted to 1.12 μm giving a value for λ_m=0.12. The transmission calculated with equation 5.3 is reported in figure 5.6.

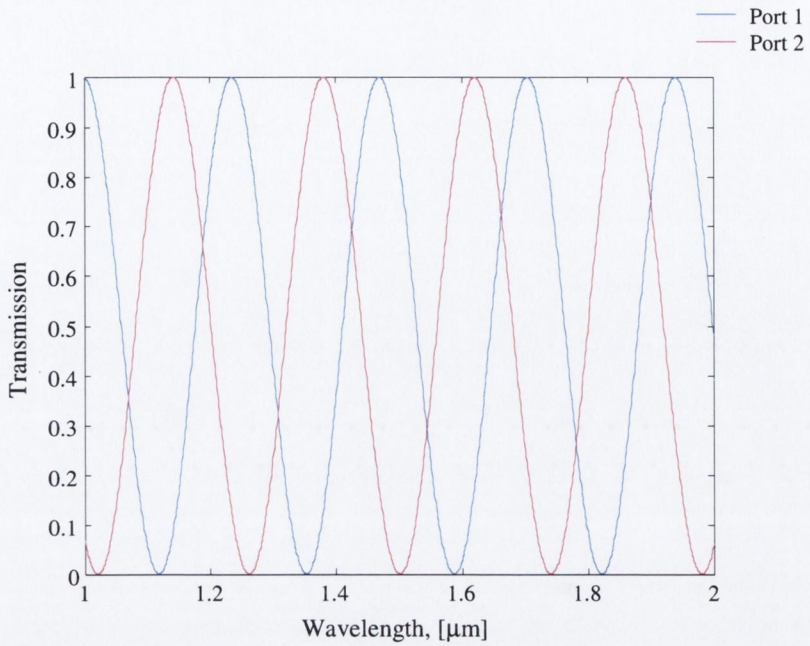

Figure 5.6: Theoretical transmission for the fibre chromatic coupler calculated from equation 5.3.

5.3 Construction of the Amplifier.

The following section will provide a description of the other factors that have to be taken into account relating to the hardware upon which the construction of the amplifier is based.

The previous chapter reported the studies carried out in order to predict the theoretical losses based on the matching of the MFD (mode field diameter) of the two fibres for single mode operation. An easier way to calculate the geometrical spot size is by the aid of the Marcuse polynomial formula. According to Marcuse-Wyatt [8, 9], equation 5.4 should be precise to few percent with respect to the full calculation reported in chapter 4. The results for the two wavelengths 1.49 μm and 1.88 μm are shown in the table 5.1 below for the two-fluoride fibre and the transmission fibre Corning SMF-28.

The ratio between the spot size ω and the core radius a can be evaluated when the normalized frequency V is between 1.2 and 2.4 (single mode operation limits) as:

$$\frac{\omega}{a} = 0.64 + \frac{1.619}{V^{3/2}} + \frac{2.879}{V^{6}}. \tag{5.4}$$

Table 5.1 : Spot size diameter obtained for the fibres by the polynomial equation 5.4

	SMF 28 Corning	Fibre 1	Fibre 2
MFD at 1.49 μm	4.24 μm	2.62 μm	3.60 μm
MFD at 1.88 μm	5.34μm	4.06 μm	5.61 μm

Even if the single mode mismatch is the lowest theoretical limit that can be achieved when two different types of fibres are butt-coupled, several other issues have to be taken into account in order to understand the factors that intervene in setting the value of cavity losses. The quality of the contact between the two fibres is not simply the theoretical limit but it is highly dependent on the operator skill in order to achieve high quality fluoride fibres' ends. The fluoride fibres were cleaved using a York FK 11 fibre cleaver, with tension set to a value 130 g. After cleaving, the fibre end is inspected with a high magnification microscope. The surface should appear smooth and free from microscopically visible defects. Upon inspection, the cleaved fibre end should be free from jagged edges, bulges or dips, otherwise the process has to be repeated.

A small amount of index matching fluid (Thorlabs G608N) was added in between the fluoride and the transmission fibre. It prevents the presence of air at the junction of the two optical fibres, which would cause signal reflection due to the large differential optical refractive index that exists between air and optical fibre.

Another important issue is the mechanical alignment that is required for the two fibres in order to reduce the causes of any eventual misalignments. The studies of misalignment losses have been carried out by the authoritative and elegant work of Marcuse [8]. Following Marcuse the alignment losses are essentially due to three major factors as shown in figure 5.7:

- Longitudinal Misalignment: the fibres are placed in the same direction with the core centred but separated by a length z normally filled with air.
- Angular offset or tilt misalignment
- Lateral Misalignment.

Longitudinal misaligment

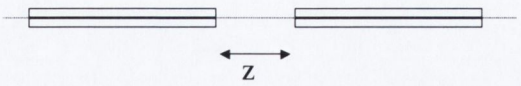

Tilt misaligment

Lateral misaligment

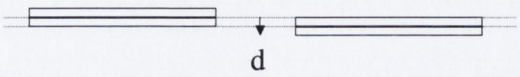

Figure 5.7: Possible causes of splice misalignments.

Lateral misalignment is the dominant type of losses among the three mechanical misalignments, it reduces the overlap area of the two fibre core end faces and consequently reduces the amount of power that can be coupled from one fibre into the other [10]. In lateral misalignment the losses are a function of d, the power loss in dB can be written as [11]:

$$\Lambda(dB) = -10\log\left(\frac{2\omega_1\omega_2}{\omega_1^2+\omega_2^2}\right)e^{\left(\frac{-2d^2}{\omega_1^2+\omega_2^2}\right)}, \tag{5.5}$$

where ω_1 is the mode field diameter for the transmission fibre while ω_2 is the mode field diameter for the fluoride active fibre calculated in table 5.1.

The expected losses from the function of the lateral offset are depicted in fig 5.8 for the two fibres used at the signal and laser wavelengths.

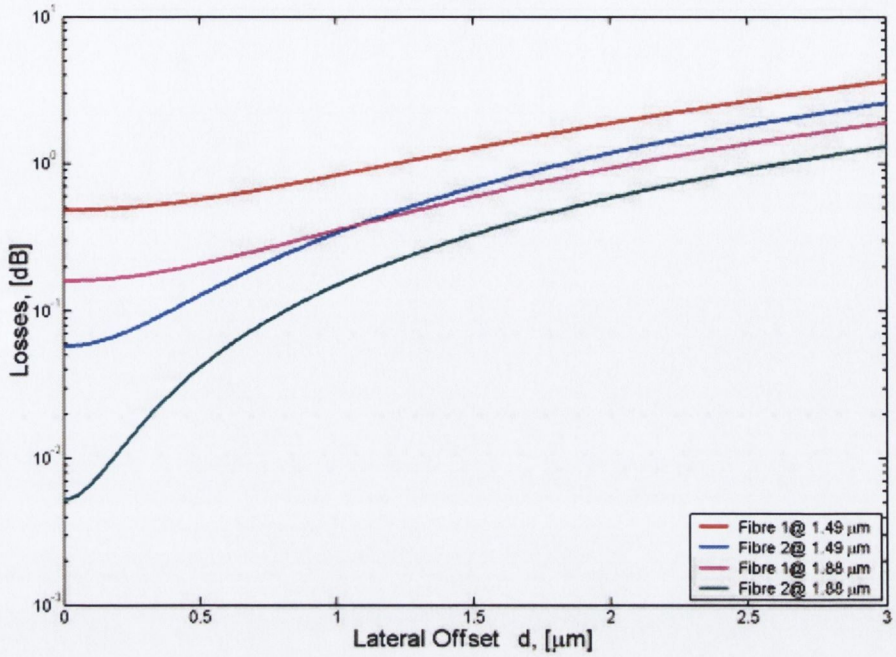

Figure 5.8: Calculated losses for lateral offset for laser and signal wavelength of the two fibres used in the construction of the cavity. The losses in dB are reported in a logarithmic scale in order to magnify the behaviour at short distance from the contact point

In order to reduce the losses caused by lateral misalignment the two fibres have been mounted on a 3-axis fibre stage with sub-micrometer precision.

The general equation for fibre misalignment can be obtained by simultaneously taking into account all the three sources of misalignment and it is:

$$\Lambda(dB) = -10\log(A)$$

$$A = \left(\frac{4\alpha}{\left(\frac{2z}{k\omega_1}\right)^2 + (\alpha+1)^2} \exp\left(- \frac{\frac{(k\omega_1)^2}{2}\left[(\alpha+1)\left(\frac{2d}{k\omega_1}\right)^2 + 2\alpha \frac{2d}{k\omega_1}\frac{2z}{k\omega_1}\sin\theta + \alpha\sin^2\theta\left(\left(\frac{2z}{k\omega_1}\right)^2 + \alpha + 1\right)\right]}{\left(\frac{2z}{k\omega_1}\right)^2 + (\alpha+1)^2} \right) \right)$$

α is the squared ratio of the mode field diameter of the two fibres, and k is the wave number referred to the refractive index of the substance between the two fibres. Equation 5.5 previously reported is a particular case when θ and z are equal to zero. In the case when the only losses are due to the tilt of the two identical fibres previous equation can be reduced to:

$$\Lambda(dB) = -10\log\left(\exp\left(\frac{k\ \omega\ \sin\ \theta}{2} \right)^2 \right). \tag{5.6}$$

It is interesting to observe that k the wavenumber scales as the inverse of the wavelength while the mode field diameter scales according to the V-number as [12]:

$$\omega \approx \frac{a}{\sqrt{\ln V}}. \tag{5.7}$$

Therefore, the mode field diameter increases with respect to the wavelength for a given radius and fibre NA. For fibre #2 the minimum value calculated is centred at 1.45 μm, although it is possible to design the fibre in order to shift the minimum to 1.88 μm where it is most needed. Expressing k in terms of the V number, the derivative with respect to V of equation 5.6 is calculated and gives a minimum when V is equal to $e^{1/2}$ (1.648). The radius and NA can then be extracted in order to minimise the loss at the required wavelength. The laser cavity is extremely sensitive to angular misalignment and generally they are difficult to reduce mechanically, it might be important to design the cavity in order to keep them at a minimum value for the laser wavelength.
It is important to underline the fact that the air separation at the two-fibres ends causes a Fresnel reflection. In the presence of air, the power coupled into the fibre is reduced by a factor R [13]:

$$R = \left(\frac{n_{fibre} - 1}{n_{fibre} + 1} \right)^2$$

where n_{fibre} is the refractive index of the fibre core. However, as will be demonstrated in section 5.8, the mismatch of the refractive index between silica fibre and fluoride fibre, even in the event that they are carefully butt-coupled and in perfect contact, will still cause a reduction in the coupling efficiency.

A thin film of index matching fluid can largely eliminate Fresnel reflection at both glass end interfaces. The use of index matching fluid cannot be avoided due to the different value of melting points of the silica and fluoride fibres making fusion splicing of the two fibres impossible.

5.4 Fibre Amplifier Set-up.

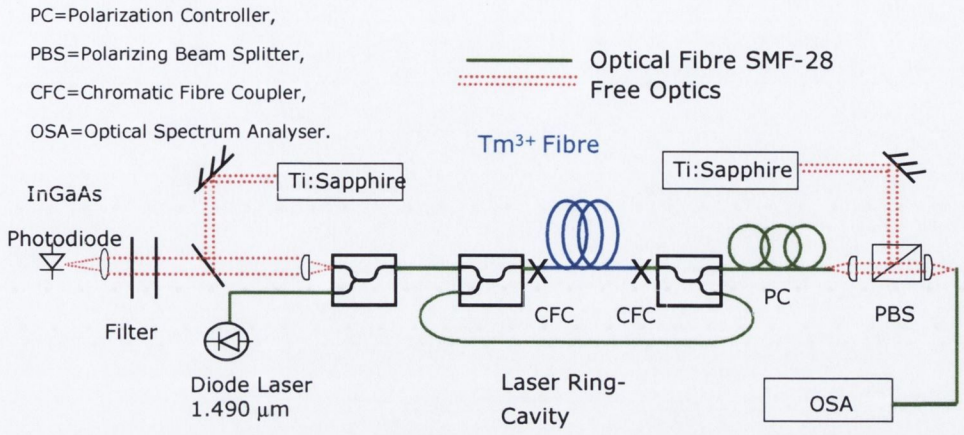

Figure 5.9: Schematic diagram showing the outline of the Tm^{3+} ring-cavity amplifier. From left to right: (PD) Photodiode with maximum efficiency at 1.9 µm; (LD) 1.49-µm single-mode laser diode; (CFC) chromatic fibre coupler; (PC) polarization controller; (PBS) polarizing beam-splitter; (OSA) optical spectrum analyser. A single Ti:Sapphire laser counter-propagating with the signal was used for the short 2.4 m cavity while a second Ti:Sapphire was added in order to pump the long 4 m cavity.

Due to the difficulties in optimising the coupler for the signal and pump wavelengths, the best pump transmission obtained over several trial couplers was –3dB at 790 nm. The two 1.88-µm outputs connected together form a ring cavity, which allows circulation of the broadband 1.8-µm fluorescence. The residual transmission through the coupler is detected with a long-wavelength InGaAs photodiode through a low-pass filter in order to cut off both signal and pump wavelength. Fluorescence at 1.88 µm can then be monitored while the amplifier is pumped with a CW Ti:Sapphire laser. A single mode laser diode with a wavelength at 1.49 µm, was used as the signal for measuring the gain in the amplifier. The power of the laser diode was limited to –40 dBm so the signal would not change the observed gain (small signal gain regime, see section 4.5).

The experimental layout is depicted in figure 5.9. The difference between the single and double pump configuration is that, a second Ti:Sapphire was used for pumping the 4-meter fibre while only a single Ti:Sapphire was used with the shorter fibre cavity.

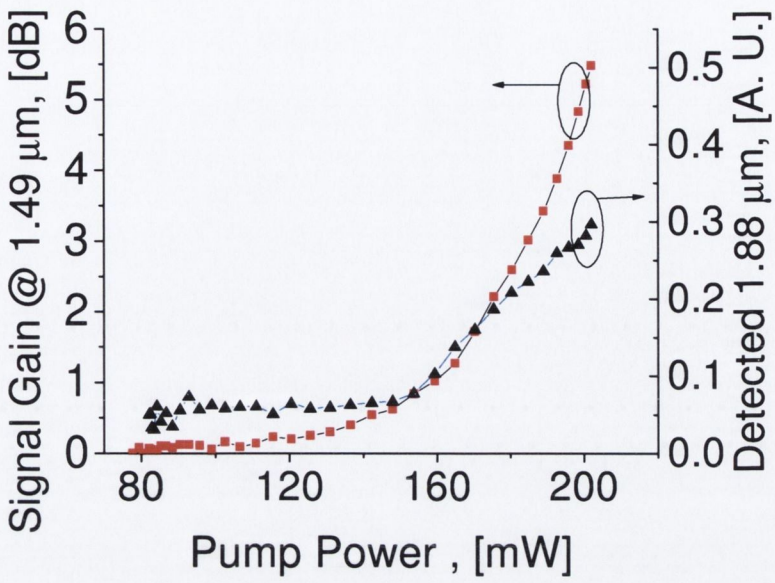

Figure 5.10: Gain for signal at 1.49 μm (left) and fluorescence detected 1.88 μm (right) measured for the 2.4 m cavity length, high NA fibre, pumped with a single Ti-Sapphire laser.

5.5 Experiment

For fibre #1, the overall losses for the cavity at 1.88 μm were estimated to be 8-10 % by adding the measured losses for the two couplers and the estimated values for the losses between the active fibre and fluoride fibre interface. Optical pumping was by a CW-Ti:Sapphire laser counter-propagating with the signal in the amplifier . Laser threshold at 1.88 μm in the ring cavity was found to be 160 mW. The gain obtained with 200 mW pumping was around 6 dB which is 4 dB higher than that observed when the ring cavity is interrupted. The detected 1.88 μm emission is shown in fig. 5.10 together with the achieved amplification. The 1.88-μm transition is a three-level system and this accounts for the relatively high threshold for lasing [14].

The second fibre tested has lower overall losses at 1.88 μm compared to the previous situation of about 2-4 %. In this case a second Ti:Sapphire pump laser was used in a counter-propagating geometry. The lasing oscillation at 1.88 μm started at a total power around 300 mW and at 400 mW an 11 dB gain was observed, compared with 4 dB with the ring cavity disconnected. The gain obtained is shown in fig. 5.11, which is linear with the total pump power.

The specific gain rises from 0.02 dB/mW below the lasing threshold up to 0.07 dB/mW above threshold.

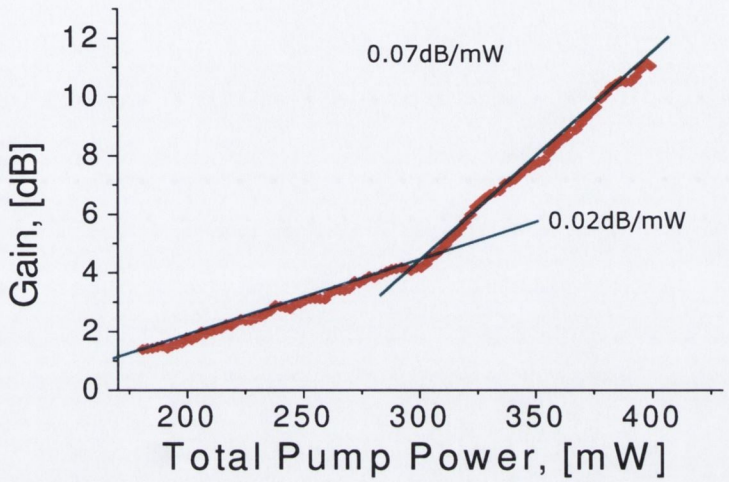

Figure 5.11: Gain at 1.49 μm measured for the 4 m. cavity length. Laser oscillation occurs at a power of 300 mW.

The tuning range has been evaluated for fibre 1 with tuning an OPO (Ti:Sapphire pumped) at different wavelength using a power lower then –40 dBm in order to remain within the case of small-signal gain.

The gain is relatively flat between 1.46 μm and 1.51 μm as shown in figure 5.12.

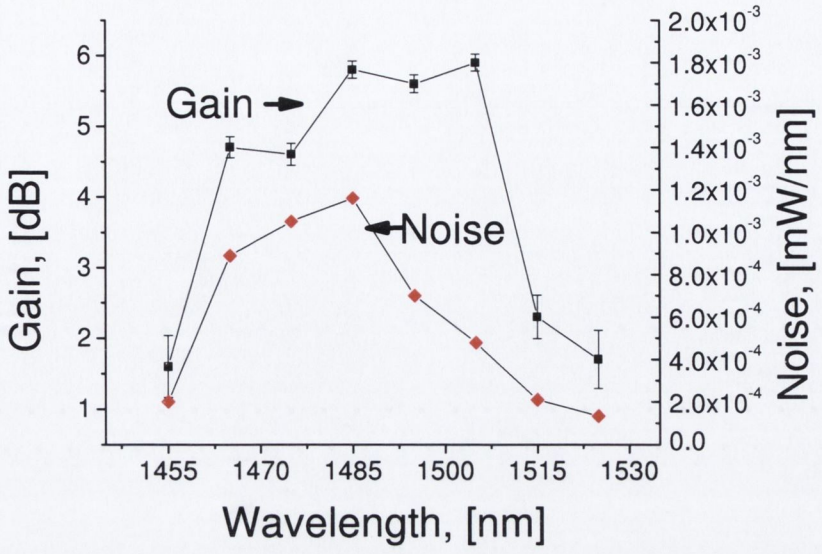

Figure 5.12: Gain and noise figure vs. signal wavelength for fibre #1

5.6 Noise Measurement

The noise in a fibre optical amplifier is due to the incoherent (random direction and phase) fluorescence that is emitted in the propagation modes and amplified while travelling through the amplifier. It is generally called amplified spontaneous emission and is usually given the acronym ASE.

There are various methods of calculating the ASE. The following method minimizes the error due to the noise contribution added by the spontaneous emission of the laser. The noise caused by the amplified spontaneous emission has been evaluated by rotating the polarization controller until the signal transmission is minimized. This allows measurement of the noise close to the optical carrier.

Half of ASE power can be estimated at 0.3 nm around the signal wavelength and then normalized for the 1 nm noise bandwidth, such a procedure is normally called the polarization-nulling method [15].

The value of the noise due to the ASE is reported in figure 5.12 along with the amplification band measured with a –40 dB tuneable optical parametric oscillator (OPO) as the input source.

5.7 Comparison with the Model

The model produced in the previous chapter can be compared with the results obtained. Both the results are shown in figure 5.13 and the predicted performance agrees quite well with the experimental data recorded for the two fibres.

The threshold expected for 1.88 μm laser oscillation appears to be well described by the model while the slope efficiency is underestimated and the error rises with the total optical pump power up to around 15% in the gain.

In contrast the gain below threshold is relatively overestimated. This is due to the difficulty in measuring small values of gain and because the absorption of the fluorescence due to the excited state absorption at 1.4 μm has not been taken into account.

The difference between the modelled and the detected gain at high power can be related to some approximations that have been made in the model: amplified spontaneous emission at 800 nm has been neglected and can have an impact in reducing the efficiency at high power. Moreover the weak pump excited state absorption at around 800 nm that produces a faint blue fluorescence has been neglected as well. Despite the approximations the model gives satisfactory results in predicting the behaviour above threshold and the threshold value. It also describes well the gain versus pump power above the threshold.

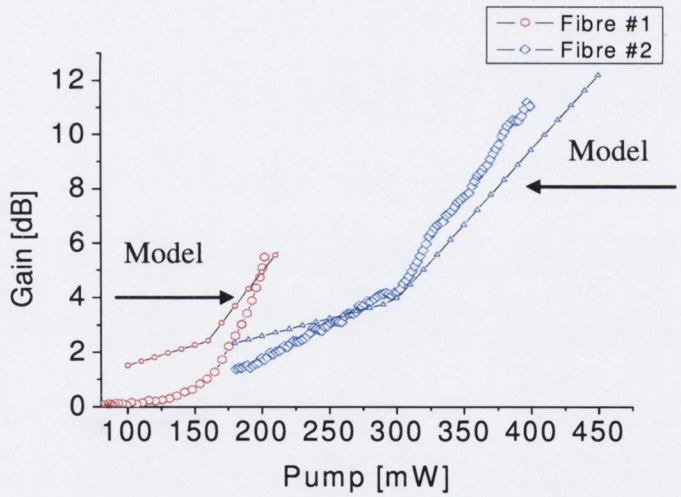

Figure 5.13: Comparison between the experimental and modelled results.

A laser rate-equations model is generally accepted as giving results with a confidence interval of around 10%

The confidence interval in the measurement of the gain can be related to two distinct sources of errors: one induced by effects related to the amplifier (such as amplified spontaneous emission) and the other related to the devices used in measurement. The

accuracy of the OSA is ±0.5 dB at –20dBm and the power stability of the diode laser is around 5% without temperature stabilization at 1 mW. The error in the measurement of the gain can be estimated as [16]:

$$\frac{G_m}{G} = 1 + B_0 \frac{Fh\upsilon}{P_s},$$

where G_m and G are respectively the measured gain and the real gain which are equal for infinite input signal power P_s. F is the noise figure and B_0 is the bandwidth of the measurement. In ref. [16] there is a useful approximation of the error in the measurement of amplifier's gain. The estimated degree of confidence in the measured and modelled values of the amplifier gain is reported as error bars in figure 5.14, it is therefore possible to conclude that the major systematic difference between the model and the experimental data is present at high pump powers where the previous mentioned approximations become more important.

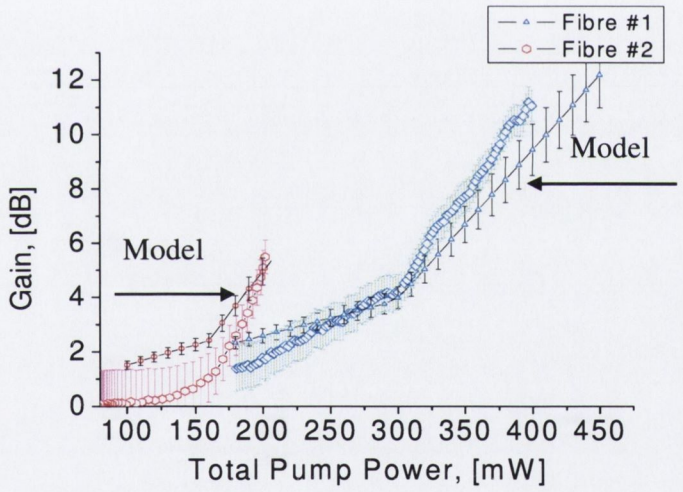

Figure 5.14:Estimated confidence interval of the measured and simulated gain for a signal at 1.49 μm. The major systematic difference is related to high power operations.

5.8 Consideration of Pump Coupling Efficiency

The optical pump at 790 nm, produced by the Ti:Sapphire laser is below the cut-off wavelength of all the fibres that have been used in this work. This causes the propagation in the fibres of higher order modes.

The number of modes that propagated in the fibre can be estimated by a simple formula allowing for two degrees of freedom for positive and negative l and two polarizations for each index (l,m). The number of modes M per unit of solid angle is given by:

$$\frac{dM}{d\Omega} = \frac{2A_{eff}}{\lambda^2}, \tag{5.8}$$

where A_{eff} is the average mode area. By substituting A_{eff} calculated with eq. 5.7 into equation 5.8 and integrating along the solid angle (eq. 2.16), the equation 5.8 gives:

$$M \approx \frac{V^2}{2n_c^{\,2}\ln(V)}. \tag{5.9}$$

The range of validity of the previous equation is related to equation 5.7. The equation 5.7 was calculated with the variational method and is reliable at low V-numbers. Equation 5.9 can provide a better estimate of the number of modes supported at low values of V in contrast to most of the estimations that can be found in literature, which are developed in order to predict the number of modes for fibres with multimode nature. In fig. 5.15 compares the exact cut-off points for the Bessel function with the approximated equation 5.9 and the approximated equation for multimode fibre found in literature are compared [16].

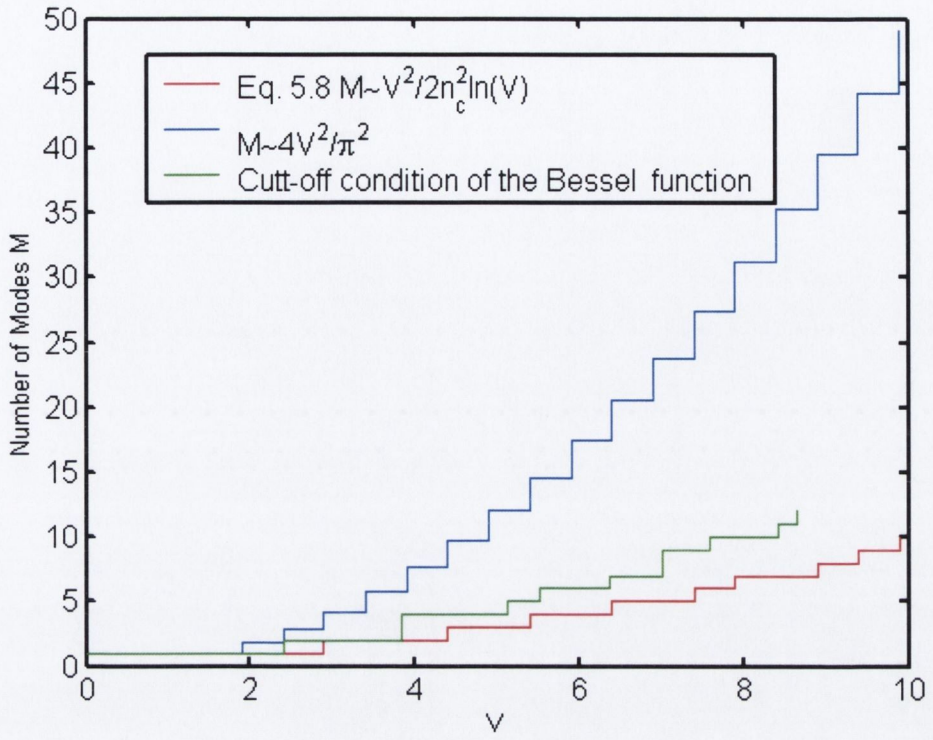

Figure 5.15: Comparison between the number of modes supported by a fibre at low V-numbers. (Blue) The approximation reported in [17]; (Green) the cut-off conditions of the Bessel function, (Red) eq. 5.9.

The V number for the three fibres involved in the previous analysis at 790 nm and the respective number of modes are given in the table 5.2 below.

At 790 nm the two active fibres support both LP_{01} and LP_{11}. The cut-off point of the LP_{01} mode is 3.832 so it is expected that a considerable amount of the power in the LP_{11} mode is travelling into the cladding while the LP_{01} is far from cut-off and so most of its power is concentrated in the core.

Table 5.2: V number and number of mode supported at 790nm

	SMF-28 Corning	**Fluoride 1**	**Fluoride 2**
V	2.96	2.99	2.93
M	2	2	2

The optical power that travels in the cladding for each mode is calculated in [18] and at $V \approx 2.9$ the fraction of the power that travels in the cladding is 35 % for the LP_{11} and 12% for the LP_{01}.

It is very difficult however to know the exact amount of the fraction power that is shared between the two modes, this forced us in the previous chapter to estimate the core confinement factor from experimental measurements. Similarly, as a bimodal system the losses between the active and transmission fibres cannot be easily expressed in a simple way, as overlap integrals between the intensity profiles of the modes. This is due to the difficulties in calculating the fraction of the total power present in each of the modes.

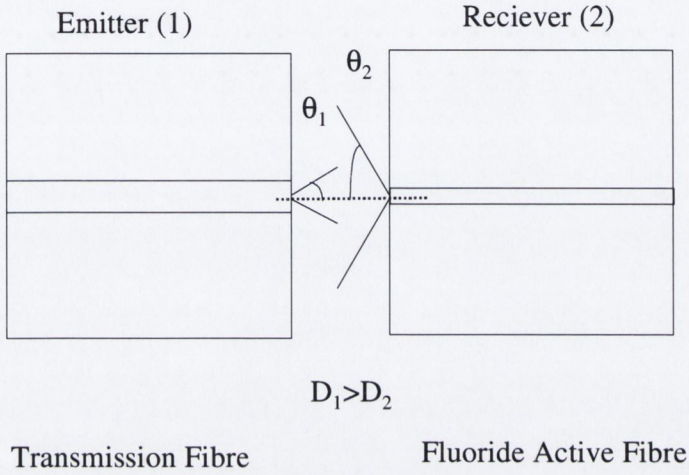

Figure 5.16: Multimode efficiency calculation from the transmission fibre (right) numbered 1 to the active fibre numbered 2.

A simple method based on the optical fibres' brightness function can be effective. Recalling the definition for the coupling efficiency with reference in fig 5.16, if P_1 the pump power emitted by the fibre 1 and P_2 the pump power coupled in the fibre 2, the coupling efficiency can be written as [10]:

$$\eta = \frac{P_2}{P_1}.$$

The transmission fibre emits at the ranged angles $0 < \theta_1 < \theta_1^c$, while the receiving fluoride fibre accepts light over the range $0 < \theta_2 < \theta_2^c$ where θ_1^c and θ_2^c are the critical angle of the two fibres. The brightness function is usually a cosine like function in the near field but due to the close proximity of the two fibres can be taken as constant for small angles:

(5.10) $$B = B_0 \cos\theta_1 \approx B_0 .$$

The total power radiated to the first fibre and the one coupled to the fluoride fibre can be calculated solving the integrals:

(5.11) $$P_1 = 2\pi A_1 B_0 \int_0^{\theta_c^1} \sin\theta d\theta,$$
$$P_2 = 2\pi A_2 B_0 \int_0^{\theta_c^2} \sin\theta d\theta,$$

since the area of the first fibre is bigger than the receiving fibre.

At small angles the sin is nearly equal to the angle itself, eq. 5.11 can be rewritten as

(5.12) $$P_{1,2} = 2\pi A_{1,2} B_0 \int_0^{\theta_c^{1,2}} \theta_c d\theta .$$

Integrating equation 5.12 with the explicit relationship between the critical angle and the numerical aperture:

(5.13) $$NA = n\sin\theta_c \approx n\theta_c ,$$

we can write for the coupling efficiency:

(5.14) $$\eta = \frac{P_2}{P_1} = \frac{A_2}{A_1}\frac{NA_2^2}{NA_1^2}\frac{n_{fluoride}^2}{n_{silica}^2} .$$

This gives an efficiency of 59%, for the case where the two fibres are directly connected. The use of an intermediate index matching fluid not only helps to align the fibre and eliminate the Fresnel reflection due to the eventual air gap but also has a considerable impact in the enhancing the overall efficiency by reducing the refractive index mismatch between fluoride and silica fibre in bare contact.

The refractive index for the fluoride is 1.52 while the one for silica is 1.46, giving an extra 8% of losses due to the refractive index mismatch between the two fibres. With the index matching fluid therefore, the efficiency will rise to 67% for multimode operation. A lens could improve the performance of the system, however even a well corrected spherical lens with a 1 cm focal length can seriously degrade the coupling for the signal and laser wavelengths due the chromatic aberration which can not be completely corrected over a spectral range of 1 μm. Other types of improvements that can be useful to obtain better performance and have not been implemented due to cost and time budget are listed below:

1 The two output ports that form the fibre loop can be spliced together in order to reduce the reflection effects that can arise from the connection between the two fibre connectors.

2 The ring fibre laser has a bi-directional output and the conversion efficiency can be increased if an isolator is introduced into the cavity. Higher and better stability in the laser oscillation for single mode operation can be achieved by the introduction of an isolator in the fibre loop [19]. This will force a single propagating direction; narrowing the line width of the laser at 1.88 μm and reducing the circulation of unwanted fluorescence emission. However, isolators usually produce losses and the threshold will inevitably rise. The best practice is to force the laser to counter-propagate with the signal; with this method the laser does not propagate along the fibre link in the same direction of an incoming signal. This allows a possible use of multiple amplifiers in cascade.

5.9 Conclusions

In this chapter, the experimental evaluation of the fibre ring cavity amplifier for signals in the telecommunications window between 1.46 μm up to 1.52 μm with a solution to overcome the relatively low efficiency of the Thulium doped fluoride amplifier has been presented. The amplifier has an all fibre ring cavity produced with cheap and easy to manufacture fibre chromatic couplers. It works with a single 790 nm relatively inexpensive pump laser in contrast to the existing double pump configuration and does not require co-doping with other rare earth ions.

The fibre material is ZBLA doped with 2000-ppm thulium. The ring cavity allows lasing at the 1.88-μm transition, thereby reducing the population of the terminating level in the amplifier. Gain enhancement up to 7dB has been observed in both high NA and standard NA fibre with cavities of different lengths and two different pumping systems.

The noise spectrum was estimated by reducing the signal at the receiver by changing the signal polarization. This allows the measurement of the amplified spontaneous emission, which has random polarization, close to the optical signal carrier.

The engineering of the cavity was extensively analysed to make it as efficient as possible. It has also been observed that losses between transmission and active fibres needed to be addressed in the early stage of the fibre design. The angle mismatch between the two fibres can in this way be minimized for the laser wavelength making the construction of the fibre-ring cost effective.

Such a scheme has the potential to further the deployment of thulium amplifiers in optical communications networks.

5.10 References

[1] S. B. Poole, D. N. Payne, and M. E. Fermann, "Fabrication of low loss optical fibres containing rare earth ions," *Electronics Letters*, vol. 22, pp. 159-161, 1985.

[2] R. I. Laming, L. Reekie, D. N. Payne, P. L. Scrivener, F. Fontana, and A. Righetti, "Optimal pumping of erbium-doped-fibre optical amplifiers," presented at Optical Communication, 1988. ECOC 88. Fourteenth European Conference on (Conf. Publ. No.292), 1988.

[3] M. Shimizu, M. Horiguchi, M. Yamada, I. Nishi, J. Noda, T. Takeshita, M. Okayasu, S. Uehara, and E. Sugita, "Compact and highly efficient fiber amplifier modules pumped by a 0.98-μm laser diode," *Lightwave Technology, Journal of*, vol. 9, pp. 291-296, 1991.

[4] Y. Miyajima, T. Komukai, and T. Sagawa, "1.31-1.36 μm Optical amplification in Nd^{3+} doped fluorozirconate fibre," *Electronics Letters*, vol. 26, pp. 2042-2044, 1990.

[5] Y. Ohishi, T. Kanamori, J. Temmyo, M. Wada, M. Yamada, M. Shimizu, K. Yashino, H. Hanafusa, M. Horiguchi, and S. Takahashi, "Laser diode pumped Pr^{3+}-doped and Pr^{3+}-Yb^{3+}-codoped fluoride fiber amplifiers operating at 1.3 μm," *Electronics Letters*, vol. 27, pp. 1995-1996, 1991.

[6] M. Shimizu, T. Kanamori, J. Temmyo, M. Wada, M. Yamada, Y. Terunuma, Y. Ohishi, and S. Sudo, "28.3 dB gain 1.3 μm-band Pr-doped fluoride fiber amplifier module pumped by 1.017 μm InGaAs-LD's," *Photonics Technology Letters, IEEE*, vol. 5, pp. 654-657, 1993.

[7] J. D. Love, W. M. Henry, W. J. Stewart, R. J. Black, S. Lacroix, and F. Gonthier, "Tapered single-mode fibres and devices. I. Adiabaticity criteria," *Optoelectronics [see also IEE Proceedings-Optoelectronics], IEE Proceedings J*, vol. 138, pp. 343-354, 1991.

[8] D. Marcuse, *Principles of Optical Fiber Measurements*. New York, 1981.

[9] T. J. Whitley and R. Wyatt, "Alternative Gaussian spot size polynomial for use with doped fiber amplifiers," *Photonics Technology Letters, IEEE*, vol. 5, pp. 1325-1327, 1993.

[10] J. P. Meunier and S. I. Hosain, "An efficient model for splice loss evaluation in single-mode graded-index fibers," *Lightwave Technology, Journal of*, vol. 9, pp. 1457-1463, 1991.

[11] D. Marcuse, "Loss Analysis of Single Mode Fibre Splices," *Bell System Tech J*, vol. 56, pp. 703-718, 1976.

[12] A. W. Snyder, "Understanding monomode optical fibers," *Proceedings of the IEEE*, vol. 69, pp. 6-13, 1981.

[13] G. Keiser, *Optical Fibre Communications*: McGraw-Hill, 1983.

[14] J. Y. Allain, M. Monerie, and H. Poignant, "Tunable CW lasing around 0.82, 1.48, 1.88 and 2.35 μm in thulium-doped fluorozirconate fibre," *Electronics Letters*, vol. 25, pp. 1660-1662, 1989.

[15] G. Vespasiano, P. Di Cesare, M. Artiglia, and T. Tambosso, "Measurement of noise figure in erbium doped fiber amplifiers," presented at Electrotechnical Conference, 1996. MELECON '96., 8th Mediterranean, 1996.

[16] D. Derickson, *Fiber Optic Test and Measurement*. Upper Saddle River, New Jersey: Prentice-Hall, Inc., 1998.

[17] B. E. A. Saleh and M. C. Teich, *Fundamentals of Photonics*: John Wiley & Sons, 1991.

[18] D. Gloge, "Weakly guiding fibers," *Applied Optics*, vol. 10, pp. 2252-2258, 1971.

[19] G. J. Cowle, D. N. Payne, and D. Reid, "Single-frequency travelling-wave erbium-doped fibre loop laser," *Electronics Letters*, vol. 27, pp. 229-230, 1991.

Chapter 6

Optimisation of an Up-conversion Thulium Doped Power Amplifier

6.1 Introduction

The development of dense wavelength division multiplexing (DWDM) operation in optical fibre telecommunication at wavelengths regions between 1.43 μm –1.53 μm (the S^+-band extends from 1.43 μm to 1.49 μm and S-band extends from 1.49 μm to 1.53 μm) [1, 2] was the driving force behind the work on thulium doped fluoride fibre amplifiers. However there has been a recent increase in the importance of high power fibre amplifiers since new developments in optical satellite communication will require more than 1 W with high beam quality and controlled polarization.

Another area where high power amplifiers could face rapid growth is medical or welding applications. The maximum power obtainable from a fibre laser is 2 kW (CW) [3] but it is located at 1.075 μm. Future power scaling in these areas of applications will require "eye safe" operation, since scattering from the atmosphere is harmful for human eyes at high power for visible and near infrared radiation. Therefore it is important to shift to mid-IR where there is lower risk for human sight and meanwhile preserving the diffraction limited beam quality and the conversion efficiency from electric to optical power.

Over the past few years an area where the power amplifier has been successfully employed is MOPAs (master oscillator optical power amplifier) where a low power seed laser, normally a DFB laser, is sequentially amplified by a series of amplifiers in order to achieve high output power. Despite the fact that silica with its better thermal properties seems advantageous with respect to fluoride-based fibre, the latter optimised for power amplifiers can be employed as a first stage amplifier in MOPAs where thermal issues are not as important [4].

As we have seen in the previous chapters, thulium (Tm^{3+}) as a dopant in glass has a fluorescence transition centred at 1.47 μm, which can be used as an amplifier in the S^+- and S-bands. Our studies have focused on thulium in a low-phonon-energy host glass (ZrF_4-BF_2-LaF_2-AlF_2 a heavy metal fluoride glass) in which the 1.47-μm transition of the Tm^{3+} ions has higher radiative efficiency and transition from the metastable level

has a longer lifetime compared with silica. However, as depicted in the energy level diagram (figure 6.1), the upper level for the transition $^3H_4$ has a lifetime of 1 ms, while the lower level $^3F_4$ has a lifetime on the order of 10 ms. This type of situation has been referred to as a self-terminating transition and creates a "bottleneck", where the population builds up in the terminating level, reducing the overall efficiency of the amplifier.

Higher efficiency can be achieved by up-converting the excess $^3F_4$ ion population to the $^3F_2$-$^3F_3$ thermally coupled levels through an excited state absorption (ESA), which has an energy corresponding to wavelengths from 1.040 μm to 1.070 μm. A residual ground state absorption is also present at these wavelengths so single-wavelength pumping with Nd-YAG (1.064 μm) or Yb fibre lasers (1.047 μm) will generally produce some low level of amplification [5]. However, because of the low pump absorption, long fluoride fibre lengths are necessary in order to obtain a large gain.

Improved efficiency can be obtained by directly pumping one of the ground state absorption transitions, while the 1 μm radiation will be used essentially for up-converting the excess population in the $^3F_4$ level. This type of configuration has been used to obtain the highest conversion efficiency observed to date for Tm^{3+}-doped fibre amplifiers with pumping at 1.56 μm (ground state transition) and 1.40 μm (excited state transition) [6].

The 800 nm technology for high power semiconductor diode lasers is well established due to the market for pump lasers for erbium fibre amplifiers [7] and for this reason we have focused on this wavelength for pumping the strong thulium ground state absorption centred at 790 nm. In contrast, technology for high power laser diodes at 1.05 μm is not yet developed. There is clearly a need to investigate the performance of these dual pumped systems, particularly with regard to balancing the power of the pump lasers for optimum power amplifier performance. The aim of this chapter is to present the experimental results that we have obtained for a thulium amplifier pumped at 1.06 μm and at tuneable wavelengths in the 0.79 μm absorption band.

The measurements carried out represent a validation and a starting point for the construction of a model of the amplifier. This will allow us to optimise the ratio of the two pump powers involved.

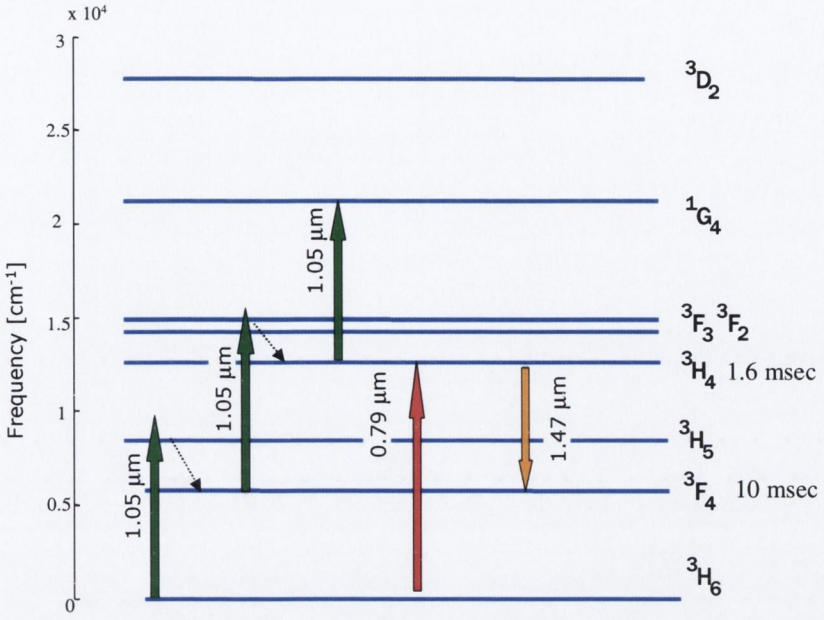

Figure 6.1: Diagram of the Tm^{3+} energy levels: the upward arrows represent the pumping scheme of the upconversion amplifier where photons are absorbed from the 1.064 µm and 790 nm pump radiation. The downward arrow represents the transition responsible for the amplification process around 1.47 µm.

6.2 Amplifier Set-Up

A Nd-YAG- Coherent 1.064 µm laser has been coupled in a 40-metre single mode Corning SMF 28 fibre since the laser was located in a different laboratory. The fibre was connected directly to the second port of the coupler described in chapter 5 and as shown in fig.6.2

The active fibre is a 4 m. length of ZBLA fluoride glass fibre with 2000 p.p.m thulium doping level, 4.4-µm core diameter and NA=0.17. As previously demonstrated (Chapter 4) it produces low losses when connected to the SMF 28 Corning transmission fibre.

The fibre was cleaved at both ends and butt-coupled with the common port of the chromatic fibre couplers by a film of index matching fluid (Thorlabs G608N). This prevents the presence of air at the junction of the two optical fibres, which would otherwise cause signal reflection due to the large differential optical impedance that exists between air and optical fibre as was discussed in chapter 5.

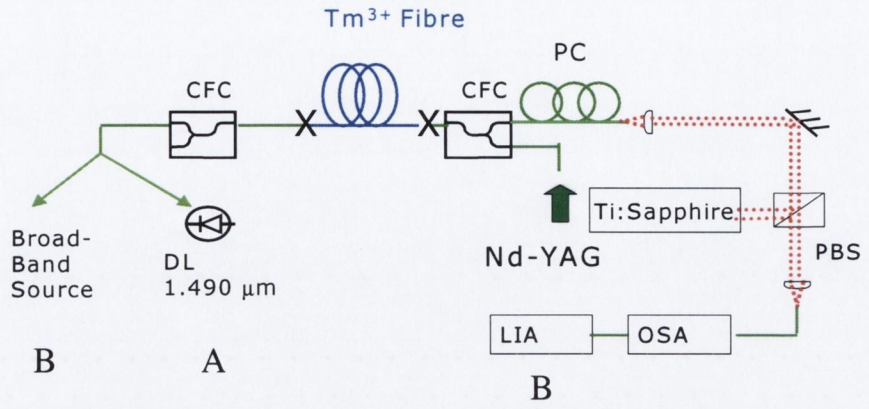

Figure 6. 2 Schematic diagram showing the outline of the Tm^{3+} amplifier:

The two pumps are coupled together by (CFC) chromatic fibre coupler.

A) The signal from a 1.49-µm single-mode laser diode (DL) is detected from the output of the amplifier after a (PBS) polarizing beam-splitter. The (PC) polarization controller maximizes the signal throughput in the (OSA) optical spectrum analyser.

B) Light from a Xenon lamp is detected by reading the output of the OSA in a (LIA) lock-in amplifier.

The estimated 1.064 µm power was 250 mW at the input port of the coupler where the loss at this wavelength was around 5 dB (see figure 5.5). Therefore the estimated power in the active fibre was about 60 mW and it was sufficient enough to show high blue up-converted emission from the entire 4 m. active fibre as shown in figure 6.3 (A).

A Ti:Sapphire laser tuned to790 nm was coupled to the other port of the chromatic fibre coupler and co-propagated with the Nd-Yag pump. The maximum power in the fibre was limited to 60 mW, a value that is well below the threshold damage level of the fibre. It is possible to observe with the naked eye the presence of the additional 790 nm pump as shown in figure 6.3 (B).

At 790 nm thulium ions strongly absorb the pump radiation and due to the long lifetime of the $^3F_4$ level large population can be built up, this drastically changes the absorption length for the 1.064 µm pump laser, leading to a large blue up-converted fluorescence emission.

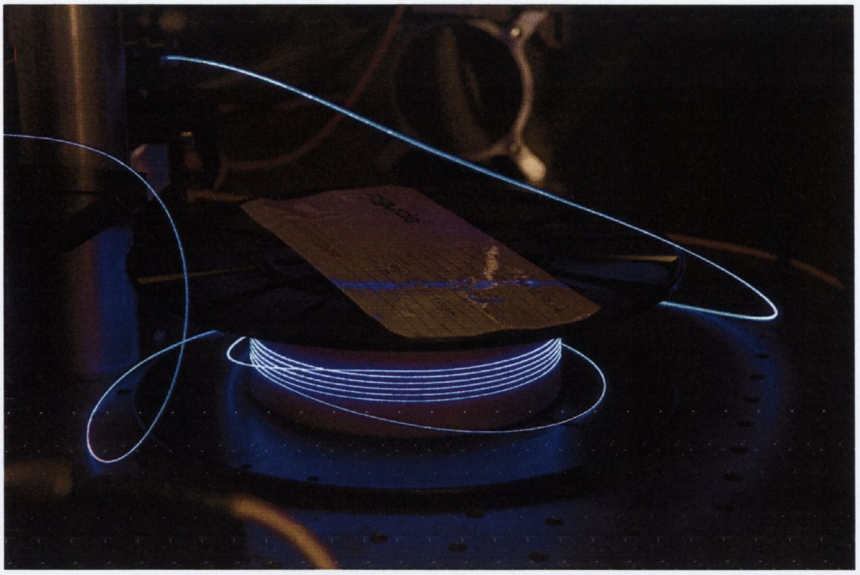

Figure 6.3 (a): Thulium doped fibre pumped with 60 mW of 1.064 μm with a Nd:Yag laser; low ground state absorption allows a homogeneous blue up-conversion along the overall length of fibre

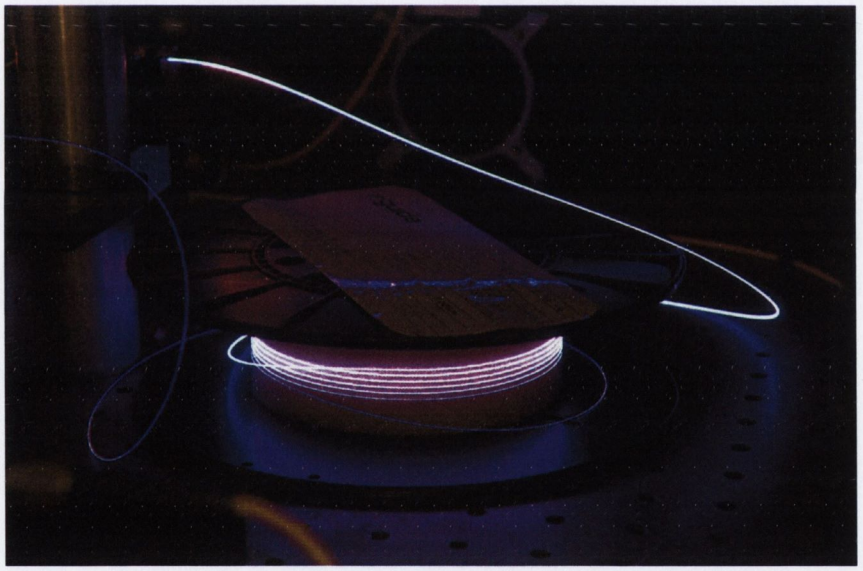

Figure 6.3 (b): Thulium doped fibre simultaneously pumped by a Ti:Sapphire and the Nd:Yag laser with similar power (60 mW). The lasers are coupled to the bright blue end of the fibre leading to a large blue emission from more than ¾ of the length of the fibre.

At the other end of the fibre it is noticeable that the blue up-conversion is largely reduced, the 1.064 μm pump is therefore largely absorbed. Since both of the pump wavelengths used for optical pumping are almost fully absorbed, the system is *a priori* deemed efficient.

A reference signal has been obtained from a single mode diode laser working at 1.49 μm (fig, 6.2 A) and it was recorded with an OSA after it had travelled the entire length

of the active fibre counter-propagating with respect to the two pumps. This configuration seems the best in order to achieve the maximum saturation, since the forward ASE that builds up in the fibre meets the signal amplifier at the end where the signal is not yet being amplified [8].

The available power of the laser was limited to –5 dBm, while the small –signal gain region corresponds to input power levels where the signal amplification does not appreciably reduce the gain of the amplifier. Therefore a small but practical level, for instance –40 dBm, has been used.

The small signal gain tuning curve along the amplifying wavelength region was measured by modifying the set-up presented in fig. 6.2 (caption B) using a broadband light source, a 75W Xenon lamp coupled into a single mode fibre. This amplified signal from the fibre output was measured by using the OSA as a monochromator and passing its (electrical) signal output to a lock-in amplifier. Spectral resolution was set to 0.2 nm. The gain between 1.45 μm and 1.55 μm was recorded for different values of the 790 nm pump optical power.

6.3 Optical Characterization

With the optical power of both pumps at 60 mW and the Ti:Sapphire tuned to 790 nm the recorded gain from the OSA was 12.5 dB in the small-signal regime. In this case the signal power was around –40 dBm and does not have an impact on the ion population of the levels involved in the amplification process (Small-signal gain).

The amplified Tm^{3+} fluorescence and the small signal gain are shown in fig. 6.4. The gain due to the 1.064-μm Nd:YAG pump alone was 2 dB while adding 790 nm pump increased the gain to 12.5 dB. The behaviour of the amplifier was also measured at higher signal powers and at –5 dBm input signal power, the gain decreases to 0.7 dB (11.8 dB) below the small-signal case.

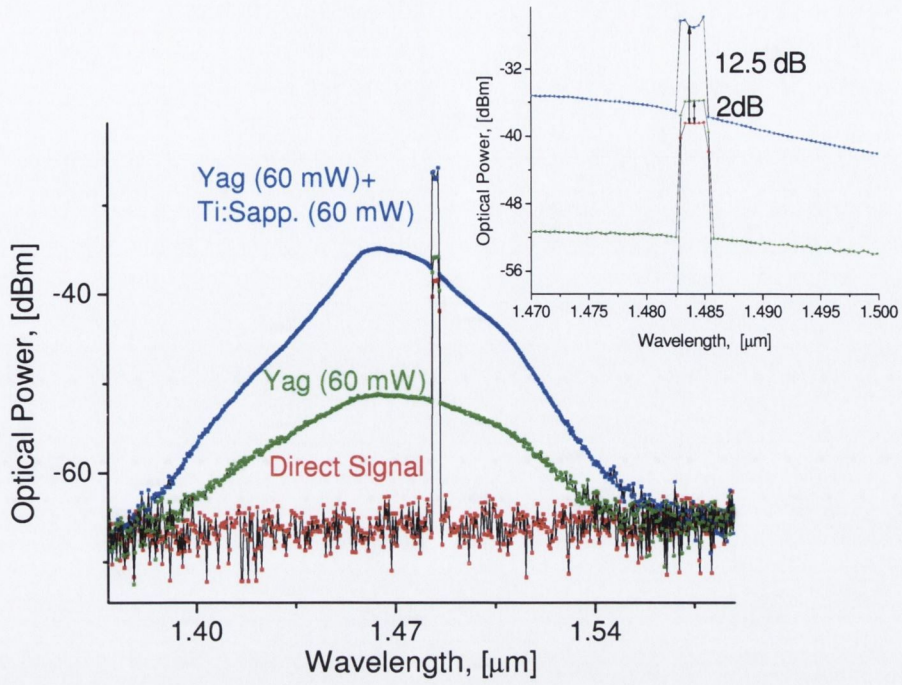

Figure 6.4: The detected Tm^{3+} fluorescence peaked at 1.47 μm is reported when optical power for the two pumps is set to 60 mW and when only the 60 mW of 1.064 μm is present. The inset shows the effect on the signal probe at 1.49 μm.

The spectral response of the gain, measured with a broadband source, is shown in fig. 6.5. The gain profile shows a significant red shift from the emission band, which is centred at 1.47 μm, and this is attributed to re-absorption. The peak structure is essentially due to the total output of the fibre coupler as observed in fig 5.3.

6.4 High Power Operation

Operation at large signal power usually requires several diode laser pumps in the amplifier package, so cost and complexity tend to increase. Therefore it is necessary to optimise the amplifier in order to achieve the maximum efficiency possible between the pump power injected and the signal gain.

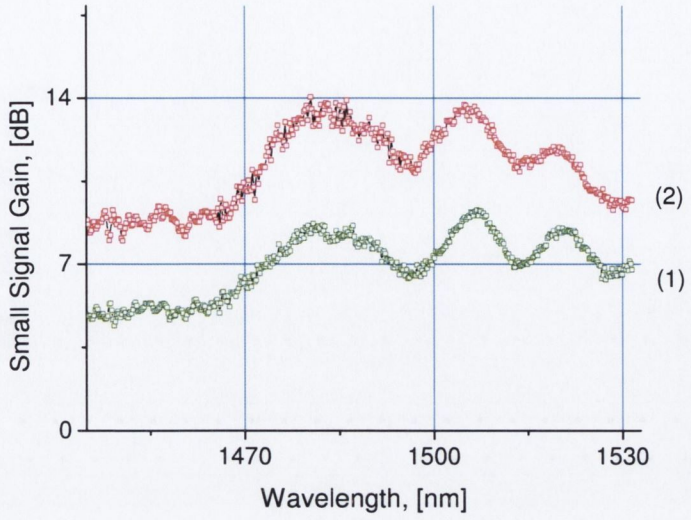

Figure 6.5 Gain versus wavelength within the amplification band. (1) Ti:sapphire power of 30 mW, Yag power 60 mW; (2) Ti:sapphire power of 60 mW, Nd:Yag power 60 mW

A figure of merit for amplifiers which describes the capacity of the system to convert pump photons to signal photons is the photon conversion efficiency (PCE), which is defined as the ratio of the photons converted into signal and the number of injected pump photons:

$$PCE = \frac{\frac{P_{Out}^{s} - P_{In}^{s}}{h\upsilon^{s}}}{\frac{P^{TiS}}{h\upsilon^{TiS}} + \frac{P^{Nd}}{h\upsilon^{Nd}}}, \tag{6.1}$$

with a little algebra and the dispersion relationship $\lambda\upsilon = c$ we have:

$$PCE = \frac{\left(P_{Out}^{s} - P_{In}^{s}\right)\lambda^{s}}{P^{TiS}\lambda^{TiS} + P^{Nd}\lambda^{Nd}}, \tag{6.2}$$

where $P_{In}{}^{s}$ is the signal input and $P_{Out}{}^{s}$ is the signal output powers; λ^{s} is the signal wavelength and P^{TiS}, λ^{TiS}, P^{Nd} and λ^{Nd} are the powers and wavelengths for the Ti:Sapphire and the Nd:YAG pump lasers. Even if power conversion efficiency is the usual parameter when dealing with power optimisation, the two definitions are different when a large energy relaxation is present in the system. In the case of low phonon energy hosts, phonon assisted relaxation is negligible for infrared fluorescence up to 2 μm so photon conversion efficiency can be used. Moreover the PCE as it has been defined does not depend on the pump and signal wavelength.

Since changing the Ti:Sapphire wavelength will affect the absorption cross-section, the pump at 790-nm can be tailored to access the value of the absorption cross-section where the maximum photon conversion efficiency is obtained. As depicted in fig. 6.6 for a 4 m length of fibre, the maximum PCE and gain achievable for a 60 mW pump power from both the Ti:Sapphire and the Nd-YAG is when the Ti:Sapphire is tuned to 800 nm. At lower wavelengths a small reduction of the gain is probably due to the concurrent excited state absorption cause by the Ti:Sapphire.

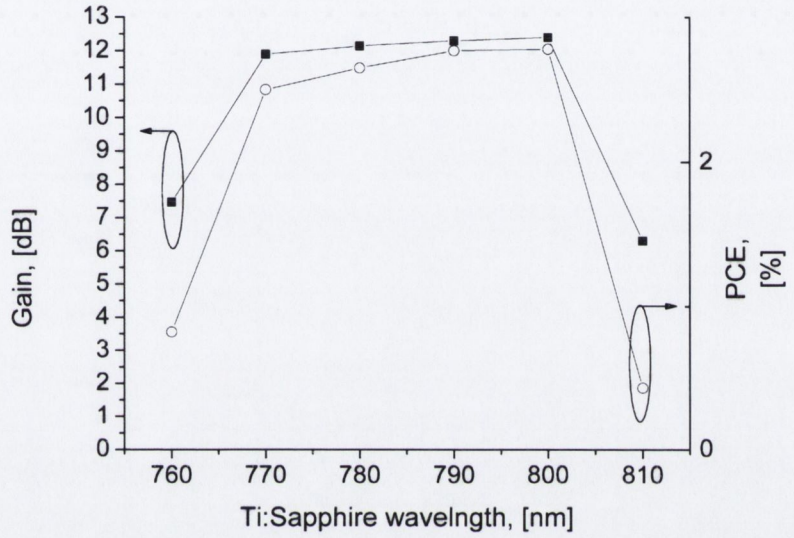

Figure 6.6: Measured gain and PCE observed for different Ti:Sapphire pump wavelengths

In the dual-wavelength pumped Tm^{3+} system, the secondary pump depletes the terminating level, therefore, a good saturation characteristic can be predicted, and once the photon conversion efficiency is high. An estimate of the saturation intensity in the limit of total bleaching of the terminating level is given by [9]:

$$I_{Sat}^{s} = \frac{h\upsilon^{s}}{\sigma_{se}^{s}\tau_{4}}, \tag{6.3}$$

so a σ_{se}^{s} stimulated emission cross-section at 1.49 μm of the order of 2.5 10^{-25} m^2 and a lifetime of the $^3H_4$ level of 1 ms give a saturation intensity of 5 10^{11} mW/m^2 or in the case of our fibre give a saturating signal power of +9 dBm.

This makes Tm^{3+} two colour pumped fibre particularly suitable for a gain-shifted booster amplifier since it can operated at a high level of signal input and low pump powers at wavelengths between 1.49 μm and 1.53 μm (S band).

Usually the output capability of the amplifier is defined as the 3 dB compression point i.e. the output power where the amplifier gain is reduced to 50 % of its small signal value. The 3 dB compression point is proportional to the saturation power according to the following equation:

$$P_{out}(-3dB) = \ln(2)P_{sat} \tag{6.4}$$

which leads to a value of +6 dBm for the 3 dB point compression. Further improvement of the 3 dB compression point can be achieved by designing the active fibre with a larger mode field diameter, so making fibres that usually have higher NA.

6.5 Transient Gain Dynamics

The dynamics of gain –recovery is important in order to address the possible cross talk during multichannel amplification. A slow gain recovery dynamic usually makes the amplifier more immune to saturation induced cross-talk effects [10].

The set-up used is similar to that previously shown in fig 6.2. In this case, the 1.49 μm-laser diode was externally driven by a square pulse generator, which provides the current necessary to run the diode. The transient gain dynamic in the amplifier was characterized by measuring the time dependent gain generated by the modulated signal. A digital oscilloscope recorded the detected signal of the OSA. The trace of the oscilloscope is presented in fig.6 7 and clearly shows that at low modulation frequency (45 Hz) the leading edge overshoots, which corresponds to a transient of the unsaturated gain regime, followed by a decrease to the steady state conditions. The exponential decay has a characteristic value of 0.64 ms [11]. Once the signal laser is turned on a fast depletion of the $^3H_4$ level occur and this reduces the efficiency of the $^3H_4 \rightarrow {}^1G_4$ excited state absorption; the system thus relaxes with a time scale proportional to the $^1G_4$ transition lifetime (0.77 ms) in order to find a new equilibrium point. With the presence of the signal the population density in the terminating level is larger than without the signal. The rate of the transition $^3F_4 \rightarrow {}^3F_2$-$^3F_3$ is larger and this tends to reduce the population inversion, the system relaxes in order to find a new equilibrium and the gain recovered after around 10 ms demonstrating that after the initial overshooting the population inversion (maximum gain, lowest noise) between the two amplifying levels is maximized.

The decay time has been reported to be pump power dependent and for almost the same type of conditions, Tm^{3+} in fluoride fibre have slower dynamics than the erbium in silica counterpart.[10], this makes for saturated multichannel operation shielded from non-linear cross talk between the channels.

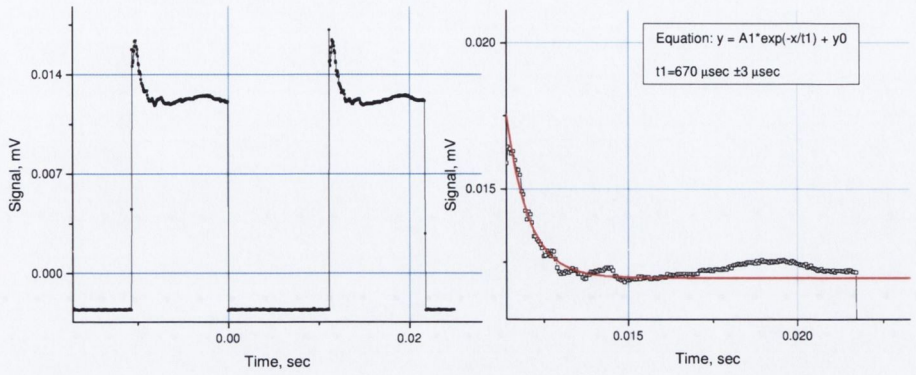

Figure 6.7: (Right) Trace detected by the digital oscilloscope clearly shows the overshooting at the leading edge, while the system reaches the steady state conditions at larger times. (Left) The dynamic is related to the lifetime of the transition $^1G_4$ due to the excited state absorption of the pump and to the lifetime of the terminating level. The exponential decay fit is shown in red.

Cross talk in optical amplifiers between several high power signals is due to the competition of the different signals for the pumped ions. The result is that in a cascade of amplifiers, some channels will grow at the expense of others [12].

Moreover, since optical non-linear effects limit the maximum power, large differences in channel powers make it difficult to keep the weaker channels above the detection threshold.

The difference in the non-linear response between fluoride and silica doped amplifiers is related to the different broadening mechanism of the fluorescence. In silica, the ions have a dominant homogenous mechanism while in fluoride both mechanisms are present; spectral hole burning for instance was demonstrated to be quite different for the two cases. In silica, a spectral hole clearly appears when the power is enough to selectively depopulate the excited state. In fluoride, no clear hole burning is observable and the spectral gain is distorted and not centred at the wavelength of the saturating probe [13].

6.6 Amplifier Noise

The determination of the noise level of an optical amplifier can be a problem due to the amplified optical signal overlapping the noise level. In the previous chapter it was demonstrated that using a polarization controller it is possible to estimate the amplified spontaneous emission close to the optical carrier. It is common in an amplifier to define the noise factor F which is directly correlated to the degree of inversion in the ionic population as [14]:

$$F = \frac{1}{G}\left(\frac{2\rho_{ASE}}{h\upsilon^{s}} + 1\right). \tag{6.5}$$

where ρ_{ASE} is the spectral density of the amplified spontaneous emission and G is the gain of the amplifier.

Another simple and practical way to estimate the noise level of the amplifier is via the so-called *interpolation method.* In fig. 6.8, the spectrum of the amplified signal is shown, the baseline has been interpolated and the value of the spectral density ρ_{ASE} (mW/nm) at the principal mode has then been estimated and gives a value of 3.7 dB for the noise figure F.

At high OSA resolution, it is possible to observe a large number of extra side modes on both sides of the main mode. These side modes are suppressed by a factor of 20-30 dB lower than the main mode. Side modes as presented in figure 6.9 preserve their own individuality even if it is almost covered by the amplified spontaneous emission due to the part of the emitted fluorescence which is amplified in a particular emission mode. They are also subject to the same gain that the main mode experiences. The impact of the ASE in the gain calculation is in this case not negligible (see eq. 2.17, section 2.10) and therefore needs to be taken into account. Moreover, observing the difference between the output power and input power (in dB) for the side modes and subtracting to that value the gain of the main mode (in dB) gives a rough method for estimating the noise level. This shows the importance of reducing the impact that the signal side modes can have in the determination of the gain where ASE and signal have comparable power.

The output signal is close to the 3 dB compression point calculated with eq 6. 3 so we are close to the region of minimum noise. The tendency of the noise level is to decrease from the small-gain limit while the signal power increases. This occurs since the ASE is suppressed and the population inversion will rise until the noise level reaches its minimum.

At a higher signal power, the noise figure will begin to increase with increased input signal power because the signal itself will cause the population inversion to deteriorate.

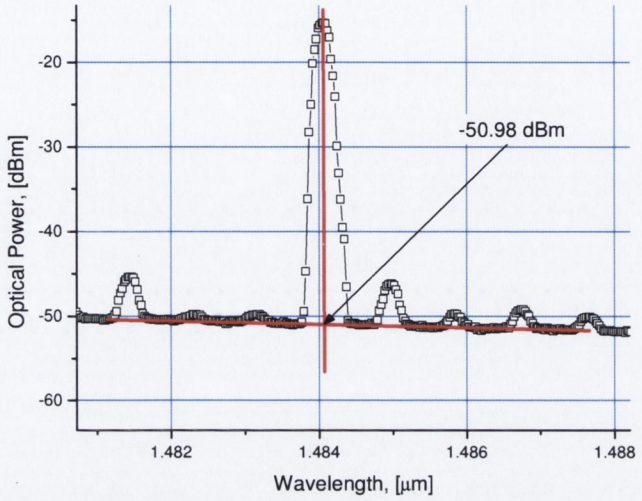

Figure 6.8: Measured noise with the interpolation method, the resolution of the OSA is set to 0.1 nm.

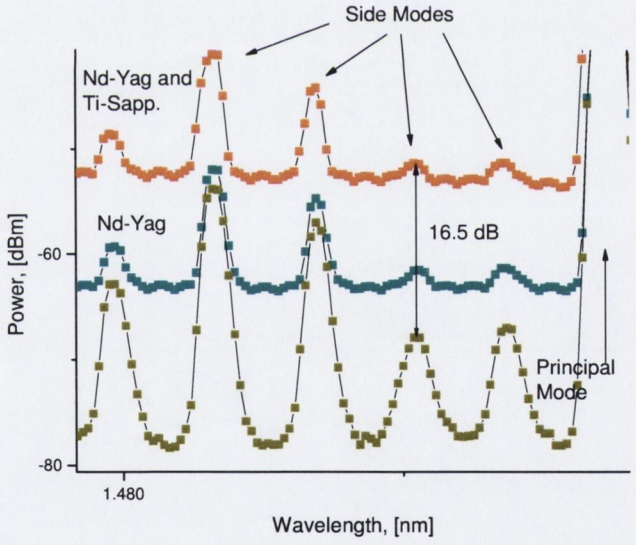

Figure 6 9: Side modes have a comparable power with respect to the amplified spontaneous emission; the 16.5 dB gain that is observed is subject to the contributions from the ASE that need to be subtracted.

6.7 Optimisation

The optimisation criteria for fibre amplifiers will strongly depend on the intended application, for example preamplifiers require high gain with good gain linearity while for high signals (booster amplifier), output power and pumping efficiency are important

considerations. Here, we concentrate on the intermediate case with –10 dBm input signal level as representative of the onset of gain saturation. The optimisation criterion chosen is to maximise the pump to signal photon conversion efficiency. This is important for a booster amplifier as the performance of a practical amplifier is often limited by the pump powers available from laser diodes. At these signal levels, the effect of the amplified spontaneous emission (ASE) is not significant and is not considered here.

As experimentally observed, the starting point for our analysis was selected at an input signal power of –10 dBm, the Ti:Sapphire tuned at 800 nm and the fibre with the same doping and parameters (NA, core diameter, length) of the fibre used in order to carry on the previous reported experimental data.

Since operation at around 1.47 μm is reduced by lower relative inversion and/or re-absorption, the analysis was limited to the 1.49-μm operation where these effects can be neglected. The model that has been developed is similar to that published by Kasamatsu *et al.* [15] where the steady state population of the relevant levels has been numerically integrated simultaneously with the propagation equations using a fourth- order Runge-Kutta method.

Thulium in ZBLA at 1.49-μm is a four level system and so high conversion efficiency is expected. A threshold power is related to the self-terminating nature of the 1.49-μm transition, however in the presence of an efficient upconversion for the $^3H_4$ population the gain coefficient $\gamma^s = \sigma^s_{se} N_4 - \sigma^s_{esa} N_2$ is always positive and the optimum fibre length is set in order to absorb as much pump power as possible [16]. The $\sigma_{se}{}^s$ is the signal stimulated emission cross-section while $\sigma_{esa}{}^s$ is the signal excited state absorption cross-section and N_4 and N_2 the population densities of the two levels involved in the process of signal amplification as depicted in fig. 6.10.

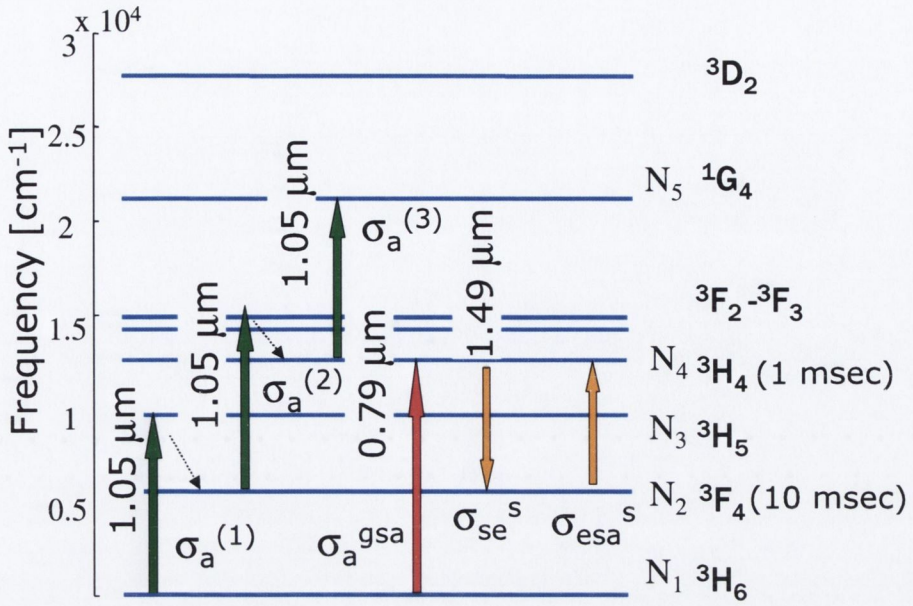

Figure 6.10: Diagram of the energy levels: the upward arrows represent absorbed photons from the 1.064 µm pump, the ground state absorption at 790 nm and signal excited state absorption while the downward arrow represents the stimulated emission at signal 1.49 µm. Each transition has an associated cross-section. The population densities for the levels involved in the model are named N_i with i=1 to 5. Lifetimes of the amplifying transition are also given.

The signal propagation is governed by a differential equation where P^s is the signal power at the z point in the fibre:

$$\frac{dP^s}{dz} = -\gamma^s P^s, \tag{6.6}$$

the minus sign is due to the counter propagation of pumps and signals and the γ^s is the gain coefficient. Equation 6.6 has to be integrated simultaneously with the pump propagation equations and this can be written as:

$$\begin{aligned} \frac{dP^{TiS}}{dz} &= -\Gamma(\lambda^{TiS})\gamma^{TiS}P^{TiS} - \alpha_{800} \\ \frac{dP^{Nd}}{dz} &= -\Gamma(\lambda^{Nd})\gamma^{Nd}P^{Nd} - \alpha_{1064}, \end{aligned} \tag{6.7}$$

where $\Gamma(\lambda^{TiS})$ and $\Gamma(\lambda^{Yag})$ are coefficients which take into account the multimode nature of the two pumps and α_{800} and α_{1064} are scattering losses of the ZBLA fibre at the

two pumps wavelength. We used the approximation $\alpha_{800} \approx \alpha_{1064} \approx 0.1 dB/m$ as reported in the specification of the ZBLA fibre.

The γ^{TiS} and γ^{Nd} terms in equation 6.7 are the absorption coefficients for the two pumps given by:

$$\begin{aligned} \gamma^{TiS} &= -\sigma_a^{gsa}(\lambda^{TiS})N_1, \\ \gamma^{Nd} &= -\sigma_a^{(1)}(\lambda^{Nd})N_1 - \sigma_a^{(2)}(\lambda^{Nd})N_2 - \sigma_a^{(3)}(\lambda^{Nd})N_4, \end{aligned} \tag{6.8}$$

where the various absorption cross sections involved and the population densities of the electronic levels (N_i) are shown in fig 6.10 and listed in table 6.1.

All the population densities are described by rate equations and the steady state value is obtained by algebraically solving the rate equations together with the conservation equation:

$$\frac{dN_1}{dt} = -\sigma_a^{gsa} N_1 \Phi^{TiS} - \sigma_a^{(1)} N_1 \Phi^{Nd} + A_{21}N_2 + A_{41}N_4 + A_{51}N_5,$$

$$\frac{dN_2}{dt} = +\sigma_a^{gsa} N_1 \Phi^{TiS} - \sigma_a^{(2)} N_2 \Phi^{Nd} - \sigma_{esa}^{s} N_2 \Phi^{s} + \sigma_{se}^{s} N_4 \Phi^{s} - A_{21}N_2 + A_{42}N_4 + A_{52}N_5,$$

$$\frac{dN_3}{dt} = 0,$$

$$\frac{dN_4}{dt} = \sigma_a^{gsa} N_1 \Phi^{TiS} + \sigma_{esa}^{s} N_2 \Phi^{s} - \sigma_{se}^{s} N_4 \Phi^{s} + \sigma_{esa}^{s} N_2 \Phi^{s} - \sigma_a^{(2)} N_4 \Phi^{Nd} + A_{54}N_5 - A_{41}N_4 - A_{42}N_4$$

$$\frac{dN_5}{dt} = \sigma_a^{(2)} N_4 \Phi^{Nd} - A_{51}N_5 - A_{52}N_5 - A_{54}N_5$$

$$N_{Tot} = \sum_{i=1}^{5} N_i$$

The Φ^{TiS} and Φ^{Nd} are the number of photons per unit time and mode field area as defined in eq. 4.9. for the two pumps and Φ^{s} for the signal. The level $^3H_5$ has strong non-radiative relaxation and the steady state value for the population density was taken as zero, the same as for the $^3F_2$-$^3F_3$ thermally coupled energy levels.

The structure of the amplifier was taken into account by the two boundary conditions to which equations 6. 6 and 6.7 are subjected, and represent the fact that the two pumps are injected in the fibre at *z=0* while the signal is counter-propagating from the other end of the active fibre.

The confinement factor $\Gamma(\lambda)$ in equation 6.4 describes the overlap of the pump mode with the fibre core dopant. This has been obtained by measuring the transmission of the fibre at the Ti:Sapphire wavelength. This gives $\Gamma(\lambda^{TiS})$=0.52. The $\Gamma(\lambda^{Nd})$ was estimated to be equal to 0.94 from the ratio of the radius of the fibre and the gaussian

spot-size calculated from the polynomial expression 5.4. All the parameters used in the simulation are reported in table 6.1.

Table 6.1: Parameters that have been used in the numerical simulation.

Parameter	Unit	Symbol	Value	Remarks
Thulium Conc.	m^{-3}		$3.2\ 10^{25}$	Specification.
Core diam.	μm		4.4	Specification.
NA			0.17	Specification.
Background loss @ 800 nm	dB/m		0.1	Specification.
Signal stimulated emission cross section	m^2	σ_{se}^{s}	$2\ 10^{-25}$	Measured (ch. 2)
Signal ESA cross-section	m^2	σ_{esa}^{s}	$0.9\ 10^{-25}$	Measured (ch. 2)
Abs. cross section 800 nm	m^2	σ_{a}^{gsa}	$1.9\ 10^{-25}$	[15]
Abs cross section 1.064 μm	m^2	$\sigma_{a}^{(1)}$	$3\ 10^{-26}$	Measured (ch. 2)
	m^2	$\sigma_{a}^{(2)}$	$9\ 10^{-25}$	Measured (ch. 2)
	m^2	$\sigma_{a}^{(3)}$	$2.5\ 10^{-27}$	[17]
Confinement factor 800nm		$\Gamma(\lambda^{TiS})$	0.52	Measured.
Confinement factor 1.064μm		$\Gamma(\lambda^{Nd})$	0.94	Estimated [18].
Spontaneous emission rate	s^{-1}	A_{51} A_{52} A_{54} A_{41} A_{42} A_{21}	564.7 214.0 138.3 615.6 75.1 123.8	Used for the rate equations [13]

Figure 6.11 shows the calculated gain as a function of the two pump powers. The gain measured for 30 mW of Ti:Sapphire and 60 mW of Nd:Yag is 7.2 dB and the calculated value is 7.04 dB while with 60 mW of Ti:Sapphire the measured gain is 12.5 dB as shown in fig. 6.4 while the calculated gain is 13.2 dB, showing good agreement. For a given Ti:Sapphire power, a fast increase in gain with Nd:YAG power is seen, due to the depletion of the terminating level, after which the gain is almost independent of the Nd:YAG power due to the small GSA absorption at 1.064 μm.

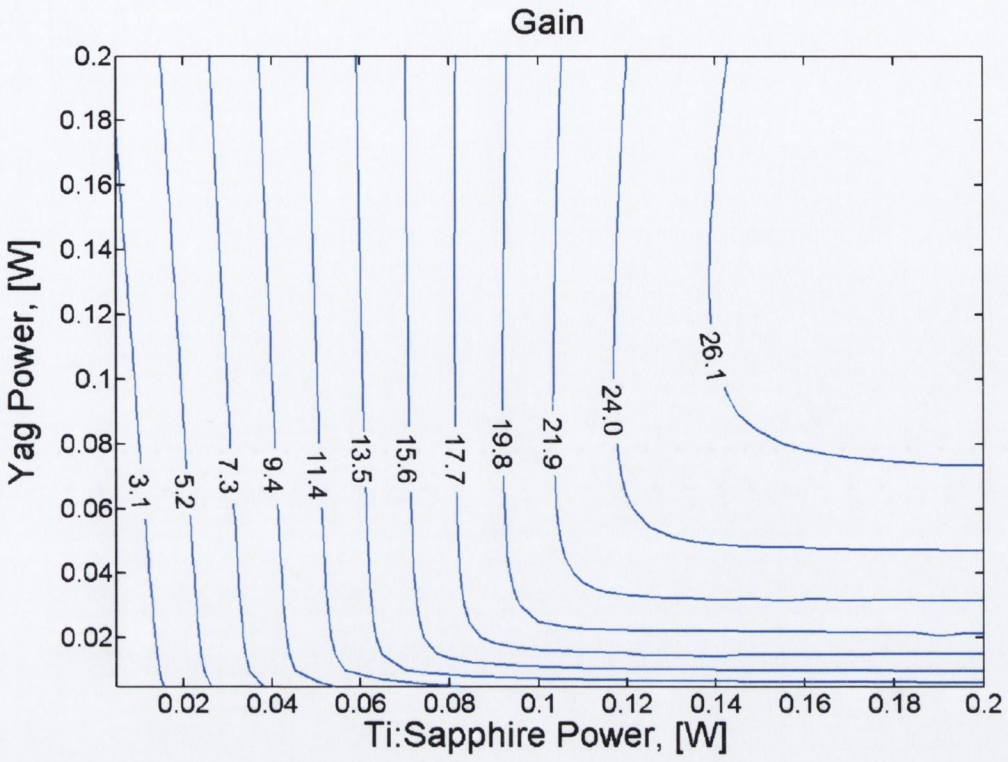

Figure 6.11: Calculated gain for different values of the two pump powers.

The transition between these two regimes can be seen as a maximum in the PCE. At a given Ti:Sapphire power, the PCE will sharply rise with the increase of the Nd:YAG power and then as the terminating level is bleached the PCE will decrease. The contour of maximum PCE (fig. 6.12) gives the optimum pump power combination and can be approximated by an empirical quadratic equation given the best ratio between Ti:Sapphire power and YAG power as:

(6.9) $$P_{Nd:Yag} = 3.2P^2_{Ti:Sapphire}.$$

We have defined the PCE as the number of stimulated emitted photons normalised by the total number of pump photons (eq. 6.2); considering only the two strong absorption mechanism the theoretical limit will be 50%, however a more reasonable figure observed in a real amplifier [19] is around 30% which is close to the limit reached by PCE for Ti:Sapphire power above 150 mW and YAG power above 75 mW. A longer fibre length is not needed since the theoretical PCE performance can be achieved in the short fibre and longer fibre will reduce the obtainable theoretical limit due to the scattering loss associated with the two pumps and the signal.

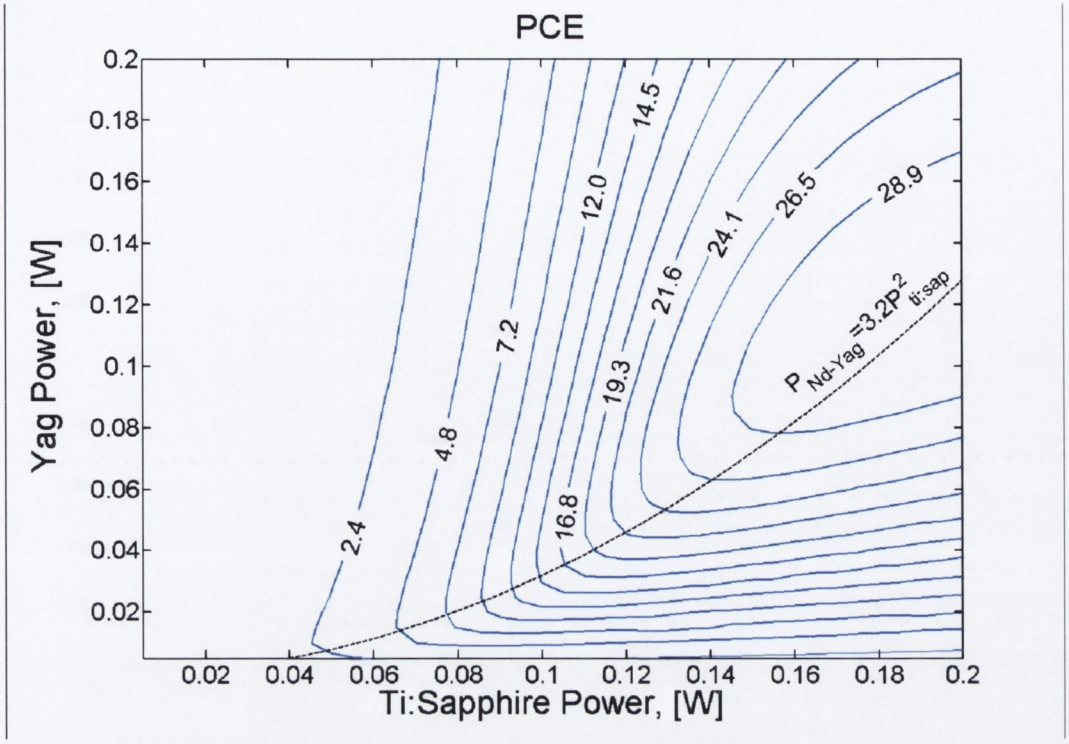

Figure 6.12: Calculated PCE for different values of the two pump powers. The maximum value for the PCE with respect to the pumps is shown as a dashed line.

In figure 6.13 we report the expected gain within the fibre length for the two pump powers. Starting from the left hand side of fig. 6.13 it is possible to calculate the 800 nm power required in order to obtain the maximum PCE and the gain obtained as a function of the length of the active fibre. The method can be used for different pumping schemes and can be tailored in order to fulfil different types of conditions and fibre geometry.

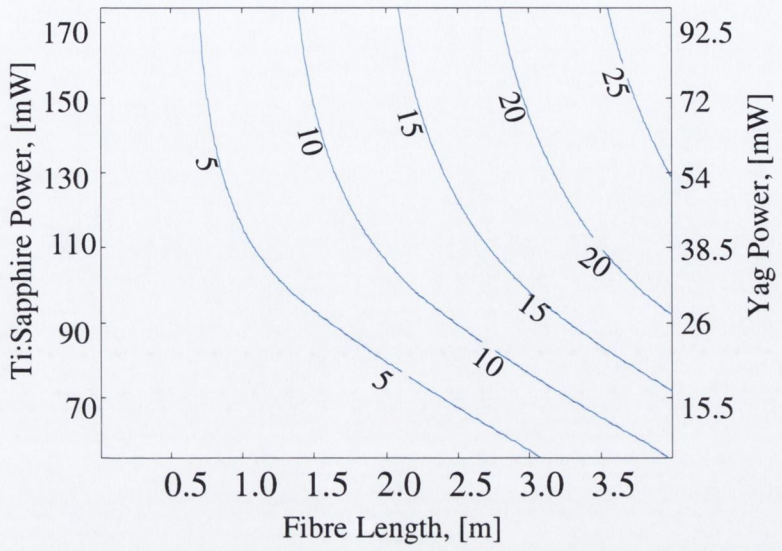

Figure 6.13: Gain predicted within the fibre for the two pumps when the power for the Nd:YAG is correlated to the Ti:Sapphire by the empirical relationship 6.9.

6.8 Conclusions

We have constructed a 4 m length thulium doped fibre amplifier pumped by a Nd:YAG (1.064 μm) laser and a Ti:Sapphire (800 nm) laser with the intention of optimising the operation of the amplifier for high signal gain at a wavelength above 1.49 μm. Experimental observations suggest the best pump wavelength is located at 800 nm for the Ti:Sapphire and practical signal operation of –10 dBm does not considerably affect the gain at 1.49 μm.

It has been demonstrated that the transient gain is connected to the lifetime of the $^1G_4 \rightarrow {}^3H_6$ transition, while low cross talk at saturated operation is expected.

High signal operations require the maximum photon conversion efficiency, so we have developed a model, not limited to the small-signal gain, in order to find the operation points where the maximum PCE is obtained for the lowest optical power of the two pumps involved.

For a given value of the Ti:Sapphire power we established that the corresponding value for the Nd:YAG power obeys to an empirical quadratic relationship.

The gain within the fibre length of the amplifier has been calculated so the required length in order to achieve the desired gain can be found.

6.9 References

[1] F. Roy, "Recent advances in thulium-doped fiber amplifiers," presented at Optical Fiber Communication Conference and Exhibit, 2002. OFC 2002, 2002.

[2] R. Caspary, U. B. Unrau, and W. Kowalsky, "Recent progress on S-band fiber amplifiers," presented at Transparent Optical Networks, 2003. Proceedings of 2003 5th International Conference on, 2003.

[3] V. P. Gapontsev, D. V. Gapontsev, N. S. Platonov, O. Shkurihin, V. Fomin, and S. Ferin, "2 kW CW ytterbium fiber laser with record diffraction-limited brightness," presented at CLEO Europe 2005, Munich (DE), 2005.

[4] C. Alegria, Y. Jeong, C. Codemard, J. K. Sahu, J. A. Alvarez-Chavez, L. Fu, M. Ibsen, and J. Nilsson, "83-W single-frequency narrow-linewidth MOPA using large-core erbium-ytterbium Co-doped fiber," *Photonics Technology Letters, IEEE*, vol. 16, pp. 1825-1827, 2004.

[5] B. Bourliaguet, F. Emond, S. Mohrdiek, A.-C. Jacob-Poulin, P.-Y. Cortes, and J. Lauzon, "Thulium-doped fibre amplifier using 1055 nm laser diode pumping configuration," *Electronics Letters*, vol. 38, pp. 447-448, 2002.

[6] S. Aozasa, H. Masuda, H. Ono, T. Sakamoto, T. Kanamori, Y. Ohishi, and M. Shimizu, "1480-1510 nm band Tm-doped fibre amplifier with high power conversion efficiency of 42%," *Electronics Letters*, vol. 37, pp. 1157-1158, 2001.

[7] B. Pedersen, W. J. Miniscalco, and S. A. Zemon, "Evaluation of the 800 nm pump band for erbium-doped fiber amplifiers," *Lightwave Technology, Journal of*, vol. 10, pp. 1041-1049, 1992.

[8] R. I. Laming, J. E. Townsend, D. N. Payne, F. Meli, G. Grasso, and E. J. Tarbox, "High-power erbium-doped-fiber amplifiers operating in the saturated regime," *Photonics Technology Letters, IEEE*, vol. 3, pp. 253-255, 1991.

[9] T. Rasmussen, A. Bjarklev, O. Lumholt, M. Obro, B. Pedersen, J. H. Povlsen, and K. Rottwitt, "Optimum design of Nd-doped fiber optical amplifiers," *Photonics Technology Letters, IEEE*, vol. 4, pp. 49-51, 1992.

[10] E. Desurvire, "Analysis of transient gain saturation and recovery in erbium-doped fiber amplifiers," *Photonics Technology Letters, IEEE*, vol. 1, pp. 196-199, 1989.

[11] B. M. Walsh and N. P. Barnes "Comparison of Tm:ZBLAN and Tm:silica fiber lasers; Spectroscopy and tunable pulsed laser operation around 1.9 μm," *Applied Physics B: Lasers and Optics*, vol. 78, pp. 325-333, 2004.

[12] S. C. Fleming, "Crosstalk in 1.3 μm praseodymium fluoride fiber amplifiers," *Lightwave Technology, Journal of*, vol. 14, pp. 66-71, 1996.

[13] I. Joindot and F. Dupre, "Spectral hole burning in silica-based and in fluoride-based optical fibre amplifiers," *Electronics Letters*, vol. 33, pp. 1239-1240, 1997.

[14] C. R. Giles and E. Desurvire, "Modeling erbium-doped fiber amplifiers," *Lightwave Technology, Journal of*, vol. 9, pp. 271-283, 1991.

[15] T. Kasamatsu, Y. Yano, and T. Ono, "1.49-μm-band gain-shifted thulium-doped fiber amplifier for WDM transmission systems," *Lightwave Technology, Journal of*, vol. 20, pp. 1826-1838, 2002.

[16] F. F. Ruhl, "Figures of merit for doped fibre amplifiers in 1300 nm and 1550 nm windows," *Electronics Letters*, vol. 27, pp. 1605-1607, 1991.

[17] T. Komukai, T. Yamamoto, T. Sugawa, and Y. Miyajima, "Upconversion pumped thulium-doped fluoride fiber amplifier and laser operating at 1.47 μm," *Quantum Electronics, IEEE Journal of*, vol. 31, pp. 1880-1889, 1995.

[18] T. J. Whitley and R. Wyatt, "Alternative Gaussian spot size polynomial for use with doped fiber amplifiers," *Photonics Technology Letters, IEEE*, vol. 5, pp. 1325-1327, 1993.

[19] T. Kasamatsu, Y. Yano, and T. Ono, "Gain-shifted dual-wavelength-pumped thulium-doped fiber amplifier for WDM signals in the 1.48-1.51-μm wavelength region," *Photonics Technology Letters, IEEE*, vol. 13, pp. 31-33, 2001.

Chapter 7

Conclusion

Having been studied for more than two decades, fibre lasers and amplifiers remain a solid and prolific part of modern optical science and technology. Fibre amplifiers are the front-runners in the implementation of the ultra large information carrying capabilities of the new optical telecommunications, and they maintain a considerable role in the development of new near and mid infrared applications. At the time of writing this thesis, an article published from Kozak and co-workers [1] shows the possibility of achieving high quality and durable glue splicing between silica fibre and fluoride fibre, making possible the integration of low-phonon energy fibre with the existing transmission technology.

A renewed interest in fibre lasers is warranted due to the impressive power scaling capability of fibre lasers [2] and fibre MOPAs [3], with the latest achievement of continuous operation kilowatts range of single mode and high beam quality; it shows how this remarkable technology can be competitive. Bulky and high power consuming lasers such as Ar-ion gas-lasers and solid state Nd-Yag will face strong competition from fibre lasers, which can guarantee similar performances but with a considerable reduction in size and power consumption. It is clear that fibre technology progress is integrated with the progress of pump or seed laser semiconductor devices and the astonishing pace in the latest development in these devices is seen as a major contribution in the fibre optics field.

An open mind and a brilliant existing international scientific community will guarantee impressive achievements in the near future.

This thesis has demonstrated the existence of resonant energy transfer in fluoride glass between the upper excited levels of thulium and praseodymium, this resonant transfer to our knowledge has never previously been proved in low phonon energy hosts and the only available literature is related to crystals at low temperature. This mechanism may be instrumental in enhancing a possible visible praseodymium laser.

It has been shown that a thulium amplifier working in a co-operative mode can be a valid option in order to obtain a highly efficient amplification in the telecommunication

band around 1.47 μm. A single pump wavelength is needed and represents a valid alternative to the complex existing thulium doped amplifier technology.

A model was developed for the previous amplifier and is a valuable tool in the design and optimisation of the amplifier, the same model with minor changes has then been used to design an optimised version for power amplification of a thulium upconversion pumped amplifier. This work can be extended to different pumping schemes.

The thesis reviews some details related to making spectroscopic measurements in fibres and provides a detailed connection between measurements and off-line calculations needed to extract significant physical parameters. The style has been kept consistently didactical hoping that future readers, unfamiliar in fibres technology, will benefit and will reduce the time needed to move from experiments to the publication of relevant information.

The future of doped fibre lasers and amplifiers are assured, doped fluoride fibres can be used as compact gain modules for amplifying signals at different wavelengths [4] moreover they are compatible with *soliton* transmission [5], a technology that has much potential in the future of optical telecommunications.

Visible and IR fibre lasers can be produced which features such as mode-hop free operation, single frequency operation, wavelength stability and accuracy, low noise and a narrow bandwidth [6]. They are an important and growing area of today's optical technology with several possible applications such as sensors and image processing.

Others important contributions that can be mentioned here are:

a) The progress toward higher power scaling: It is worth mentioning the IPG who already produce a 2.5 kW CW fibre laser, and the growth sustainability in power scaling is indicated up to 30 kW limited by the silica damage threshold, but this limit could be breached with the natural maturity of the technology and coating process [7].

b) Doped spherical micro-cavity. Rare-earth doped micro spheres have already been demonstrated to show an ultra-low threshold for laser oscillation thanks to the outstanding high quality factor possessed by these microstructures [8].

ZBLA or other fluoride fibres remain important host material, moreover, compared to the less developed chalcogeniade low phonon glasses, they posses technological advantages as the material of choice for high efficient lasers and amplifiers.

References:

[1] M. M. Kozak, W. Kowalsky, and R. Caspary, "Low-loss glue splicing method to join silica and fluoride fibres," *Electronics Letters*, vol. 41, pp. 21-22, 2005.

[2] J. Nilsson, J. K. Sahu, Y. Jeong, W. Andy Clarkson, R. Selvas, A. B. Grudinin, and S. Alam, "High Power Fiber Lasers: New Developments," presented at Proceeding of SPIE, 2003.

[3] C. Alegria, Y. Jeong, C. Codemard, J. K. Sahu, J. A. Alvarez-Chavez, L. Fu, M. Ibsen, and J. Nilsson, "83-W single-frequency narrow-linewidth MOPA using large-core erbium-ytterbium Co-doped fiber," *Photonics Technology Letters, IEEE*, vol. 16, pp. 1825-1827, 2004.

[4] N. Tomita, K. Kimura, H. Suda, M. Shimizu, M. Yamada, and Y. Ohishi, "Digital signal transmission experiment using a 1.3 μm-band Pr^{+3}-doped fluoride fiber amplifier," *Photonics Technology Letters, IEEE*, vol. 6, pp. 258-259, 1994.

[5] M. Nakazawa, Y. Kimura, and K. Suzuki, "Ultralong dispersion-shifted erbium-doped fiber amplifier and its application to soliton transmission," *Quantum Electronics, IEEE Journal of*, vol. 26, pp. 2103-2108, 1990.

[6] C. Spiegelberg, J. Geng, Y. Hu, T. Luo, Y. Kaneda, J. Wang, W. Li, M. Brutsch, S. Hocde, M. Chen, J. Babico, K. Barry, W. Eaton, M. Blake, D. Eigen, I. Song, and S. Jiang, "Compact 100 mW fiber laser with 2 kHz linewidth," presented at Optical Fiber Communications Conference, 2003. OFC 2003, 2003.

[7] V. P. Gapontsev, D. V. Gapontsev, N. S. Platonov, O. Shkurihin, V. Fomin, and S. Ferin, "2 kW CW ytterbium fiber laser with record diffraction-limited brightness," presented at CLEO Europe 2005, Munich (DE), 2005.

[8] H. Fujiwaea and K. Sasaki, "Upconversion lasing of a thulium-ion-doped fluorozirconate microsphere," *Journal of Applied Physics*, vol. 86, pp. 2384-2387, 1999.